

ABSTRACT.

ADEKORE, BABABUNMI TOLU. Acceptor Conductivity in Bulk (000 $\bar{1}$) ZnO Crystals. (Under the direction of Robert Foster Davis).

ZnO is a promising wide bandgap semiconductor. Its renowned and prominent properties as its bandgap of 3.37eV at 4.2K; its very high excitonic binding energy, 60meV; its high melting temperature, 2248K constitute the basis for the recently renewed and sustained scientific interests in the material. In addition to the foregoing, the availability of bulk substrates of industrially relevant sizes provides important opportunities such as homoepitaxial deposition of the material which is a technological asset in the production of efficient optoelectronic and electronic devices.

The nemesis of wide bandgap materials cannot be more exemplified than in ZnO. The notorious limitation of asymmetric doping and the haunting plague of electrically active point defects dim the bright future of the material. In this case, the search for reliable and consistent acceptor conductivity in bulk substrates has been hitherto, unsuccessful.

In the dissertation that now follows, our efforts have been concerted in the search for a reliable acceptor. We have carefully investigated the science of point defects in the material, especially those responsible for the high donor conductivity. We also investigated and herein report variety of techniques of introducing acceptors into the material. We employ the most relevant and informative characterization techniques in verifying both the intended conductivity and the response of intrinsic crystals to variation in temperature and strain. And finally we explain deviations, where they exist, from ideal acceptor characteristics.

Our work on reliable acceptor has been articulated in four papers. The first establishing capacitance based methods of monitoring electrically active donor defects. The second investigates the nature of anion acceptors on the oxygen sublattice. A study similar to the preceding study was conducted for cation acceptors on the zinc sublattice and reported in the third paper. Finally, an analysis of the response of the crystal to hydrostatic strain and its recovery when such strain enforces a collapse of its crystallinity is reported in the fourth paper. For the sake of brevity and the need to be concise, our supplementary investigations on extrinsic donor conductivity is deferred to other journal publications.

Acceptor Conductivity in Bulk ZnO (000 $\bar{1}$) Crystals.

by

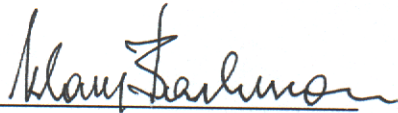
Bababunmi Tolu Adekore.

A dissertation submitted to the Graduate Faculty of North Carolina State University in
partial fulfillment of the requirements of the Degree of Doctor of Philosophy

Department of Materials Science and Engineering

Raleigh, North Carolina
2003

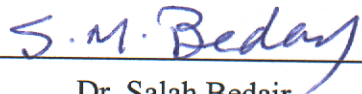
APPROVED BY



Dr. Klaus Bachmann



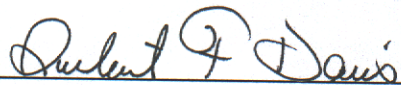
Dr. Douglas Barlage



Dr. Salah Bedair



Dr. Robert Kolbas



Dr. Robert Davis
Chairman of Advisory Committee

Dedication

All for Samson Adepitan

Words fail, and miserably they fail, in expressing what you were and still are to me Daddy!

Rest in peace indeed!

Biography.

Bababunmi Tolulase Adekore was born the last of five children to Samson (July 1, 1939-August 5, 2002) and Abiola Adekore on September 29, 1977 in Ibadan, Nigeria. Bunmi spent the beginning parts of his primary education at the Command Primary School-Bonny Camp, Victoria Island, Lagos and the concluding parts at the Command Primary School, Ibadan. He then proceeded to the International School, University of Ibadan, (I.S.I) where he completed his high school education.

Shortly after high school graduation, Bunmi immigrated to North America and commenced his university education at North Carolina State University in the spring of 1996. He graduated with high honors in Materials Science and Engineering in May of 1999. He proceeded to his doctoral studies during the fall of 1999 and successfully defended his dissertation in Materials Science and Engineering with a minor in Electrical Engineering November 13, 2003.

During his tertiary education and especially his graduate education at North Carolina State University, Bunmi has had the privilege and opportunity to interact with a truly scholarly research group at the Davis laboratories and the Department of Materials Science and Engineering at large. He is quite thankful for the support he has received from his family and friends as well as colleagues that have all made his Doctoral work at North Carolina State University a very positive and pleasant experience.

Table of Contents

Lists of Tables.....	viii
Lists of Figures.....	ix
1. Abstract	
2. Capacitance Measurements of Argon Implanted and Annealed ZnO (000 $\bar{1}$)	
Substrates.....	1
2.1. Abstract.....	2
2.2. Introduction.....	3
2.3. Experiment.....	5
2.4. Theory.....	6
2.5. Measurements and Results.....	8
2.6. Discussion.....	10
2.6.1. Low Temperature Region.....	10
2.6.1.1. Oxygen Chemisorption.....	11
2.6.1.2. Defect Association.....	12
2.6.2. Intermediate Temperature Region.....	13
2.6.3. High Temperature Region.....	16
2.6.3.1. Activated oxygen-domain boundary interaction.....	17
2.6.4. Optical Properties of Argon Implanted ZnO Crystals.....	18
2.7. Conclusions.....	19
2.8. References.....	21
2.9. Figures.....	24
3. Acceptor Conductivity in Bulk (000 $\bar{1}$)ZnO via Implantation of Nitrogen Ions.....	32
3.1. Abstract.....	33
3.2. Introduction.....	34
3.3. Experiment.....	35
3.4. Discussion.....	36
3.4.1. Impurity Selection.....	36

3.4.2.	Implantation Damage and Recovery.....	38
3.4.3.	Diode Behaviour.....	39
3.4.3.1.	Diffusion Potential and Trap induced Dipole.....	39
3.4.3.2.	CV Behaviour of Nitrogen Impalnted at 10^{15}cm^{-2}	44
3.4.3.2.1.	Structural Recovery Region.....	44
3.4.3.2.2.	Deep Levels and Trap Dominant Region.....	45
3.4.3.2.3.	Elevated Temperature Diode Stability and Dopant Ionization.....	47
3.4.3.2.4.	Ohmic Losses.....	48
3.5.	Luminescence Spectroscopy.....	49
3.5.1.	Hydrostatic Strain Effects in Oxygen Terminated Substrates.....	49
3.5.2.	Hydrostatic Strain Effects in Zinc Terminated Substrates.....	52
3.5.3.	Enhance Acceptor Transitions and New Optical lines.....	53
3.5.4.	Green Band Luminescence.....	55
3.6.	Conclusions.....	56
3.7.	References.....	57
3.8.	Figures.....	61
3.9.	Appendix.....	73
4.	Acceptor Conductivity in ZnO (000 $\bar{1}$) Bulk Substrates via Ion-Implantation of Metallic Impurities.....	75
4.1.	Abstract.....	76
4.2.	Introduction.....	77
4.2.1.	Ionicity and Ionization Potential.....	78
4.2.2.	Chemical Modulation of Valence Band and Covalency.....	80
4.2.3.	Co-ordination Polyhedra.....	81
4.3.	Experiment.....	85
4.4.	Discussion.....	86
4.4.1.	Silver-Implanted ZnO Substrates.....	86
4.4.1.1.	Chemical Properties.....	86
4.4.1.2.	Electrical Properties.....	88

4.4.1.3. Optical Properties.....	90
4.4.2. Potassium-Implanted ZnO Substrates.....	93
4.4.2.1. Electrical Properties.....	93
4.4.2.2. Optical Properties.....	94
4.4.2.2.1. Traditional Lines.....	94
4.4.2.2.2. Acceptor Transitions.....	95
4.4.2.2.3. Temperature Dependence of Acceptor Transition.....	96
4.4.3. Sodium-Implanted Samples.....	99
4.4.3.1. Electrical Properties.....	99
4.4.3.2. Optical Properties.....	100
4.4.4. Lithium and Nitrogen Codoping.....	100
4.5. Conclusions.....	101
4.6. Acknowledgements.....	102
4.7. References.....	103
4.8. Figures.....	105
5. Analysis of Implantation Damage and recovery in Ion-Implanted ZnO Substrate...	124
5.1. Abstract.....	125
5.2. Introduction.....	126
5.3. Experiment.....	128
5.4. Results and Discussions.....	129
5.4.1. Mosaic Tilt and Lateral Coherence.....	130
5.4.1.1. Virgin Substrates Implanted	130
5.4.1.2. Implanted ZnO.....	133
5.4.1.2.1. As-Implanted Substrates.....	133
5.4.1.2.2. Annealed Substrates.....	134
5.4.1.2.3. Other Implanted Impurities.....	138
5.4.2. Thermal Response.....	139
5.4.2.1. Nitrogen.....	139
5.4.2.2. Sodium and Aluminum.....	139
5.4.2.3. Lithium.....	140

5.4.2.4. Argon implanted and virgin crystals.....	141
5.4.3. Extracted Tilt of Implanted Substrates.....	141
5.5. Conclusions.....	143
5.6. Acknowledgements.....	143
5.7. References.....	144
5.8. Figures.....	146

List of Tables

<u>Chapter 2</u>		<u>1</u>
Table I	Processing conditions and identification of Argon Implanted and Virgin ZnO.	6
Table II	Optimum measuring frequency for reliable Capacitance	9
<u>Chapter 4</u>		<u>75</u>
Table I	Implantation conditions of Acceptors in Bulk ZnO	85

List of Figures

<u>Chapter 2</u>		<u>1</u>
Figure 1	Small signal equivalent circuit models for MIS capacitor	24
	(a) Series circuit model	
	(b) Parallel circuit Model	
	(c) Corrected Model	
	(d) Schematic of measurement configuration	
Figure 2	Optimal Measurement Frequency for Selected Voltages	25
Figure 3	Average carrier concentration values- N_D-N_A	26
	(i) Argon-Implanted ZnO	
	(ii) Oxygen-Terminated Grade I ZnO	
	(iii) Oxygen-Terminated Grade II ZnO	
	(iv) Zinc -Terminated Grade II ZnO	
Figure 4	Capacitance –Voltage Plots of Annealed ZnO	27
	a. Samples annealed at 25°C	
	b. Samples annealed at 350°C	
	(i) Argon-Implanted ZnO	
	(ii) Oxygen-Terminated Grade I ZnO	
	(iii) Oxygen-Terminated Grade II ZnO	
	(iv) Zinc-Terminated Grade II ZnO	
Figure 5	Capacitance-Voltage Plots of Annealed ZnO	28
	a. Samples annealed at 400°C	
	b. Samples annealed at 450°C	
	c. Samples annealed at 600°C	
	(i) Argon-Implanted ZnO	
	(ii) Oxygen-Terminated Grade I ZnO	
	(iii) Oxygen-Terminated Grade II ZnO	
	(iv) Zinc-Terminated Grade II ZnO	
Figure 6	Capacitance-Voltage Plots of Annealed ZnO	29
	a. Samples annealed at 650°C	
	b. Samples annealed at 750°C	

	<ul style="list-style-type: none"> c. Samples annealed at 850°C <ul style="list-style-type: none"> (i) Argon Implanted ZnO (ii) Oxygen-Terminated Grade I ZnO (iii) Oxygen-Terminated Grade II ZnO (iv) Zinc-Terminated Grade II ZnO 	
Figure 7	Low Resolution 8K Photoluminescence of Argon Implanted ZnO	30
	<ul style="list-style-type: none"> a. Argon As-Implanted samples b. Argon Implanted and annealed at 250°C c. Argon Implanted and annealed at 400°C d. Argon Implanted and annealed at 550°C e. Argon Implanted and annealed at 700°C f. Argon Implanted and annealed at 850°C g. Argon Implanted and annealed at 1000°C 	
Figure 8	High Resolution 8K Photoluminescence of Argon Implanted ZnO	31
	<ul style="list-style-type: none"> (a) Argon Implanted and annealed at 250°C (b) Argon Implanted and annealed at 400°C (c) Argon Implanted and annealed at 550°C (d) Argon Implanted and annealed at 700°C 	
<u>Chapter 3</u>		<u>32</u>
Figure 1	Impurity and Free Carrier profile for Nitrogen Implanted and Virgin ZnO	61
	<ul style="list-style-type: none"> (i) SIMS profile for As-Implanted Nitrogen (ii) SIMS profile for Nitrogen implanted samples annealed at 1000°C (iii) N_D-N_A profile for grade II Oxygen-Terminated virgin samples 	
Figure 2	Variation of donor traps emission peak concentration with Position and Frequency for	62
	<ul style="list-style-type: none"> (a) Nitrogen Implanted Grade I materials at 10^{16}cm^{-2} <ul style="list-style-type: none"> (i) Emission peak position (μm) (ii) Emission peak concentration ($\#/ \text{cm}^{-3}$) 	

	(b) Nitrogen Implanted Grade II materials at 10^{15}cm^{-2}	
	(i) Emission peak position (μm)	
	(ii) Emission peak concentration ($\#/\text{cm}^{-3}$)	
Figure 3	Triangular profile of donor traps distributed by X_{ti} with X_{d} (depletion Width)	63
	(i) Triangular distribution of 10^{16}cm^{-2} grade I samples	
	(ii) Triangular distribution of 10^{15}cm^{-2} grade II samples	
Figure 4	CV Measurements of Nitrogen implanted and Annealed ZnO	64
	(a) Grade I and 10^{16}cm^{-2} , (b) Grade I and 10^{15}cm^{-2} and	
	(c) Grade II and 10^{15}cm^{-2}	
	(i) Nitrogen Implanted Samples at 25°C (As-Implanted)	
	(ii) Samples annealed at 250°C	
	(iii) Samples annealed at 300°C	
	(iv) Samples annealed at 350°C	
Figure 5	$N_{\text{D}}-N_{\text{A}}$ values of Nitrogen implanted Grade I samples at 10^{16}cm^{-2}	65
	(i) $N_{\text{D}}-N_{\text{A}}$ values of samples annealed at 250°C	
	(ii) $N_{\text{D}}-N_{\text{A}}$ values of samples annealed at 300°C	
	(iii) $N_{\text{D}}-N_{\text{A}}$ values of samples annealed at 350°C	
	(iv) $N_{\text{D}}-N_{\text{A}}$ values of samples annealed at 400°C	
Figure 6	CV Measurements of Nitrogen implanted and Annealed ZnO	66
	(a) Nitrogen Implanted Grade I samples of 10^{15}cm^{-2} annealed at 450°C	
	(i) Samples annealed at 450°C and measured at 250KHz	
	(b) Nitrogen Implanted Grade II samples of 10^{15}cm^{-2} annealed at 450°C	
	(i) Samples annealed at 450°C and measured at 250KHz	
	(ii) Samples annealed at 450°C and measured at 150KHz	
	(c) Nitrogen Implanted Grade I samples of 10^{16}cm^{-2} annealed at 450°C	
	(i) Samples annealed at 450°C and measured at 1.5KHz	
	(ii) Samples annealed at 450°C and measured at 5.5KHz	
	(iii) Samples annealed at 450°C and measured at 150KHz	
	(iv) Samples annealed at 450°C and measured at 250KHz	

- (d) Nitrogen Implanted Grade I samples of 10^{15}cm^{-2} annealed at 500°C
 - (i) Samples annealed at 500°C and measured at 250KHz
- (e) Nitrogen Implanted Grade II samples of 10^{15}cm^{-2} annealed at 500°C
 - (i) Samples annealed at 500°C and measured at 1.5KHz
 - (ii) Samples annealed at 500°C and measured at 5.5KHz
 - (iii) Samples annealed at 500°C and measured at 150KHz
- (f) Nitrogen Implanted Grade I samples of 10^{16}cm^{-2} annealed at 500°C
 - (i) Samples annealed at 500°C and measured at 2.5KHz
 - (ii) Samples annealed at 500°C and measured at 5.5KHz
 - (iii) Samples annealed at 500°C and measured at 250KHz
- (g) Nitrogen Implanted Grade I samples of 10^{15}cm^{-2} annealed at 550°C
 - (i) Samples annealed at 550°C and measured at 150KHz
 - (ii) Samples annealed at 550°C and measured at 250KHz
- (h) Nitrogen Implanted Grade II samples of 10^{15}cm^{-2} annealed at 550°C
 - (i) Samples annealed at 550°C and measured at 35KHz
 - (ii) Samples annealed at 550°C and measured at 150KHz
 - (iii) Samples annealed at 550°C and measured at 950KHz
- (i) Nitrogen Implanted Grade I samples of 10^{16}cm^{-2} annealed at 550°C
 - (i) Samples annealed at 550°C and measured at 150KHz.

Figure 7

Stabilized CV Measurements of Nitrogen Implanted and Annealed ZnO 67

Measured at optimal frequency of 250KHz

- (a) Nitrogen Implanted Grade I samples of 10^{15}cm^{-2}
 - (i) Samples annealed at 600°C
 - (ii) Samples annealed at 650°C
 - (iii) Samples annealed at 700°C
- (b) Nitrogen Implanted Grade II samples of 10^{15}cm^{-2}
 - (i) Samples annealed at 600°C
 - (ii) Samples annealed at 650°C
 - (iii) Samples annealed at 700°C
- (c) Nitrogen Implanted Grade I samples of 10^{16}cm^{-2}

- (i) Samples annealed at 600°C
- (ii) Samples annealed at 650°C
- (iii) Samples annealed at 700°C

Figure 8 CV Measurement of Nitrogen Implanted and Annealed ZnO 68

Measured at optimal frequency of 250KHz

(a) Nitrogen Implanted Grade I samples of 10^{15}cm^{-2}

- (i) Samples annealed at 800°C
- (ii) Samples annealed at 850°C

(b) Nitrogen Implanted Grade II samples of 10^{15}cm^{-2}

- (i) Samples annealed at 750°C
- (ii) Samples annealed at 800°C
- (iii) Samples annealed at 850°C

(c) Nitrogen Implanted Grade I samples of 10^{16}cm^{-2}

- (i) Samples annealed at 750°C
- (ii) Samples annealed at 800°C
- (iii) Samples annealed at 850°C

Figure 9 Degree of Ionization of Nitrogen Impurities with Temperature 69

Figure 10 8K Photoluminescence spectra of Nitrogen Implanted ZnO, Argon 70

Implanted ZnO compared with Oxygen-Terminated virgin ZnO

(a) Nitrogen As-Implanted Implanted ZnO:

- (i) 10^{16}cm^{-2} Nitrogen implanted O-ZnO
- (ii) 10^{15}cm^{-2} Nitrogen Implanted on Zn-ZnO

(b) Nitrogen Implanted ZnO, Argon Implanted ZnO and Virgin ZnO annealed at 250°C:

- (i) 10^{16}cm^{-2} Nitrogen implanted O-ZnO
- (ii) 10^{15}cm^{-2} Nitrogen Implanted on Zn-ZnO
- (iii) 10^{15}cm^{-2} Argon Implanted O-ZnO
- (iv) Virgin O-ZnO

(c) Nitrogen Implanted ZnO, Argon Implanted ZnO and Virgin ZnO annealed at 400°C:

- (i) 10^{16}cm^{-2} Nitrogen implanted O-ZnO

- (ii) 10^{15}cm^{-2} Nitrogen Implanted on Zn-ZnO
- (iii) 10^{15}cm^{-2} Argon Implanted O-ZnO
- (iv) Virgin O-ZnO
- (d) Nitrogen Implanted ZnO, Argon Implanted ZnO and Virgin ZnO annealed at 550°C :
 - (i) 10^{16}cm^{-2} Nitrogen implanted O-ZnO
 - (ii) 10^{15}cm^{-2} Nitrogen Implanted on Zn-ZnO
 - (iii) 10^{15}cm^{-2} Argon Implanted O-ZnO
 - (iv) Virgin O-ZnO

Figure 11 Shift in Neutral Donor Line with temperature

72

- (a) D^0 , X variation with annealing temperature:
 - (i) Virgin O-ZnO
 - (ii) Nitrogen implanted O-ZnO at 10^{15}cm^{-2}
 - (iii) Argon implanted O-ZnO at 10^{15}cm^{-2}
- (b) D^0 , X variation with temperature:
 - (i) Virgin Zn-ZnO
 - (ii) Nitrogen implanted Zn-ZnO at 10^{15}cm^{-2}
- (c) Strain (\square) variation with temperature variation
 - (i) Argon implanted O-ZnO at 10^{15}cm^{-2} relative to O-ZnO
 - (ii) Nitrogen implanted O-ZnO at 10^{15}cm^{-2} .relative to O-ZnO
 - (iii) Nitrogen relative to Argon implantation
- (d) Strain (\square) variation with temperature for 10^{15}cm^{-2} Nitrogen Implanted Zn-ZnO relative to Zn-ZnO.

Appendix I Low Resolution 8K Photoluminescence Spectra of Nitrogen-Implanted ZnO. 73

- Ia: Nitrogen As-Implanted ZnO
- Ib: Nitrogen Implanted and annealed at 250°C
- Ic: Nitrogen Implanted and annealed at 400°C
- Id: Nitrogen Implanted and annealed at 550°C
- Ie: Nitrogen Implanted and annealed at 700°C

If: Nitrogen Implanted and annealed at 850

Ig: Nitrogen Implanted and annealed at 1000°C

Appendix II High Resolution 8K Photoluminescence Spectra of Nitrogen-Implanted ZnO.

Ia: Nitrogen As-Implanted ZnO

Ib: Nitrogen Implanted and annealed at 250°C

Ic: Nitrogen Implanted and annealed at 400°C

Id: Nitrogen Implanted and annealed at 550°C

Ie: Nitrogen Implanted and annealed at 700°C

If: Nitrogen Implanted and annealed at 850

Ig: Nitrogen Implanted and annealed at 1000°C

Chapter 4		75
Figure 1	Ionicity of Dopant-Oxide Bond	106
Figure 2	Comparison in SIMS Profile of Silver and Nitrogen Impurities	107
	(a) Ag-Implanted and Annealed at 1000°C	
	(b) N-Implanted and Annealed ZnO at 1000°C	
	(c) Ag As-Implanted ZnO	
	(d) N- As-Implanted ZnO	
Figure 3	CV Characteristics of Silver implanted and annealed ZnO	108
	(a) Silver As-Implanted	
	(b) Silver implanted and annealed at 250°C	
	(c) Silver implanted and annealed at 300°C	
	(d) Silver implanted and annealed at 350°C	
	(e) Silver implanted and annealed at 400°C	
	(f) Silver implanted and annealed at 450°C	
Figure 3	CV Characteristics of Silver implanted and annealed ZnO	109
	(g) Silver implanted and annealed at 500°C	
	(h) Silver implanted and annealed at 550°C	
	(i) Silver implanted and annealed at 600°C	
	(j) Silver implanted and annealed at 650°C	

	(k) Silver implanted and annealed at 700°C	
	(l) Silver implanted and annealed at 750°C	
Figure 3	CV Characteristics of Silver implanted and annealed ZnO	110
	(m) Silver implanted and annealed at 800°C	
	(n) Silver implanted and annealed at 850°C	
	(o) Silver implanted and annealed at 1000°C	
Figure 4	N_D-N_A profiles of Ag Implanted ZnO	111
	(a) Silver As-Implanted samples	
	(b) Silver implanted and annealed at 400°C	
	(c) Silver implanted and annealed at 650°C	
	(d) Silver implanted and annealed at 700°C	
	(e) Samples annealed 850°C	
Figure 5	Low-Resolution 8K Photoluminescence Spectra of Ag-Implanted ZnO	112
	(a) Silver As-Implanted samples	
	(b) Silver implanted and annealed at 250°C	
	(c) Silver implanted and annealed at 400°C	
	(d) Silver implanted and annealed at 550°C	
	(e) Silver implanted and annealed at 700°C	
	(f) Silver implanted and annealed at 850°C	
	(g) Silver implanted and annealed at 1000°C	
Figure 6	Reactivated Green Band Luminescence at 1000°C	113
	(a) Silver implanted and annealed at 1000°C	
	(b) Potassium implanted and annealed at 1000°C	
	(c) Sodium implanted and annealed at 1000°C	
	(d) Lithium implanted and annealed at 1000°C	
Figure 7	High Resolution 8K Photoluminescence Spectra of Silver Implanted ZnO	114
	(a) Silver As-Implanted ZnO	
	(b) Silver implanted and annealed at 250°C	

	(c)	Silver implanted and annealed at 400°C	
	(d)	Silver implanted and annealed at 550°C	
	(e)	Silver implanted and annealed at 700°C	
	(f)	Silver implanted and annealed at 850°C	
	(g)	Silver implanted and annealed at 1000°C	
Figure 8		Capacitance-Voltage Measurements of Potassium Implanted ZnO	115
	(a)	Potassium As-Implanted ZnO	
	(b)	Potassium implanted and annealed at 250°C	
	(c)	Potassium implanted and annealed at 300°C	
	(d)	Potassium implanted and annealed at 350°C	
	(e)	Potassium implanted and annealed at 400°C	
	(f)	Potassium implanted and annealed at 450°C	
Figure 8		Capacitance-Voltage Measurements of Potassium Implanted ZnO	116
	(g)	Potassium implanted and annealed at 500°C	
	(h)	Potassium implanted and annealed at 550°C	
	(i)	Potassium implanted and annealed at 600°C	
	(j)	Potassium implanted and annealed at 650°C	
	(k)	Potassium implanted and annealed at 700°C	
	(l)	Potassium implanted and annealed at 750°C	
	(m)	Potassium implanted and annealed at 800°C	
	(n)	Potassium implanted and annealed at 850°C	
Figure 9		Carrier Concentration ($N_D - N_A$) of Potassium Implanted ZnO	117
	(a)	Potassium implanted and annealed at 350°C	
	(b)	Potassium implanted and annealed at 500°C	
	(c)	Potassium implanted and annealed at 550°C	
	(d)	Potassium implanted and annealed at 600°C	
	(e)	Potassium implanted and annealed at 700°C	
	(f)	Potassium implanted and annealed at 850°C	
Figure 10		High Resolution 8K Photoluminescence of Potassium Implanted ZnO	118
	(a)	Potassium As-Implanted ZnO	
	(b)	Potassium implanted and annealed at 250°C	

- (c) Potassium implanted and annealed at 400°C
- (d) Potassium implanted and annealed at 550°C
- (e) Potassium implanted and annealed at 700°C
- (f) Potassium implanted and annealed at 850°C
- (g) Higher Resolution spectra of implanted and annealed ZnO at 850°C
- (h) Potassium implanted and annealed at 1000°C

Figure 11 Low Resolution 8K Photoluminescence Spectra of Potassium Implanted ZnO 118

- (a) Potassium As-Implanted ZnO
- (b) Potassium implanted and annealed at 250°C
- (c) Potassium implanted and annealed at 400°C
- (d) Potassium implanted and annealed at 550°C
- (e) Potassium implanted and annealed at 700°C
- (f) Potassium implanted and annealed at 850°C
- (g) Potassium implanted and annealed at 1000°C

Figure 12 Capacitance Voltage Measurements of Sodium Implanted ZnO 120

- (a) Sodium As-Implanted ZnO
- (b) Sodium implanted and annealed at 250°C
- (c) Sodium implanted and annealed at 300°C
- (d) Sodium implanted and annealed at 350°C
- (e) Sodium implanted and annealed at 400°C
- (f) Sodium implanted and annealed at 450°C

Figure 12 Capacitance Voltage Measurements of Sodium Implanted ZnO 121

- (g) Sodium implanted and annealed at 500°C
- (h) Sodium implanted and annealed at 550°C
- (i) Sodium implanted and annealed at 600°C
- (j) Sodium implanted and annealed at 650°C
- (k) Sodium implanted and annealed at 700°C
- (l) Sodium implanted and annealed at 750°C
- (m) Sodium implanted and annealed at 800°C
- (n) Sodium implanted and annealed at 850°C

Figure 13	Low Resolution 8K Photoluminescence Spectra of Sodium Implanted ZnO.	122
	(a) Sodium As-Implanted ZnO	
	(b) Sodium implanted and annealed at 250°C	
	(c) Sodium implanted and annealed at 400°C	
	(d) Sodium implanted and annealed at 550°C	
	(e) Sodium implanted and annealed at 700°C	
	(f) Sodium implanted and annealed at 850°C	
	(g) Sodium implanted and annealed at 1000°C	
Figure 14	SIMS Profile of Lithium Diffused ZnO	123
	(a) ^{64}Zn	
	(b) ^7Li	
	(c) ^{16}O	
	(d) ^6Li	
Figure 15	Capacitance-Voltage Measurements of Li-Diffused and Li-N Co-doped ZnO	124
	(a) Lithium diffused ZnO substrates annealed at 550°C	
	(b) Lithium diffused ZnO substrates annealed at 1000°C	
	(c) Lithium diffused and Nitrogen Implanted ZnO substrates annealed at 550°C	
	(d) Lithium diffused and Nitrogen Implanted ZnO substrates annealed at 1000°C	
<u>Chapter 5</u>		<u>125</u>
Figure 1	Rutherford Backscattering Measurements of Silver Implanted ZnO	146
	(a) Aligned Rutherford Backscattering Spectra of Silver As Implanted ZnO Substrates	
Figure 2	Rutherford Backscattering Spectra of ZnO	148
	(a) Virgin ZnO	

	(b) Nitrogen Implanted ZnO	
Figure 3	Schematic Illustration of the Damage Propensity in High angle tilt boundary.	149
	(a) Low angle tilt domain	
	(b) Low and high angle domain boundaries with high cross-section for implantation damage	
	(c) Amorphous clusters nucleated within single crystalline mosaic matrix	
Figure 4	Transmission Electron Micrograph of Nitrogen-Implanted ZnO	150
Figure 5	Isometric variation in $\Delta\theta$ with Reflection Order for Virgin ZnO.	151
	(a) Isometric variation in $\Delta\theta$ with Reflection Order for Virgin ZnO at 25°C	
	(b) Variation of Tilt angles (θ) with Annealing Temperature	
Figure 6	002-reflection ω -Rocking Curves of Annealed Virgin ZnO	152
	(a) Samples annealed at 25°C	
	(b) Samples annealed at 550°C	
	(c) Samples annealed at 650°C	
	(d) Samples annealed at 700°C	
	(e) Samples annealed at 850°C	
Figure 7	2 θ - ω , ω Area Maps of Silver Implanted and Virgin ZnO	153
	(a) Silver as-implanted (002) reflection	
	(b) Silver as-implanted (004) reflection	
	(c) Silver as-implanted (006) reflection	
	(d) Virgin ZnO at 25°C (002) reflection	
	(e) Virgin ZnO at 25°C (004) reflection	
	(f) Virgin ZnO at 25°C (006) reflection	
Figure 8	2 θ - ω , ω Area Maps of Silver Implanted and Virgin ZnO	154
	(a) Silver annealed at 250°C (002) reflection	
	(b) Silver annealed at 250°C (004) reflection	
	(c) Silver annealed at 250°C (006) reflection	
Figure 9	2 θ - ω , ω Area Maps of Silver Implanted ZnO annealed at 400°C	155

	(a) Silver annealed at 400°C (002) reflection	
	(b) Silver annealed at 400°C (004) reflection	
	(c) Silver annealed at 400°C (006) reflection	
Figure 10	2 \times 2, \square Area Maps of Silver Implanted ZnO annealed at 550°C	156
	(a) Silver annealed at 550°C (002) reflection	
	(b) Silver annealed at 550°C (004) reflection	
	(c) Silver annealed at 550°C (006) reflection	
	(d) Virgin ZnO annealed at 550°C (002) reflection	
	(e) Virgin ZnO annealed at 550°C (004) reflection	
	(f) Virgin ZnO annealed at 550°C (006) reflection	
Figure 11	2 \times 2, \square Area Maps of Silver Implanted ZnO annealed at 700°C	157
	(a) Silver annealed at 700°C (002) reflection	
	(b) Silver annealed at 700°C (004) reflection	
	(c) Silver annealed at 700°C (006) reflection	
	(d) Virgin ZnO annealed at 700°C (002) reflection	
	(e) Virgin ZnO annealed at 700°C (004) reflection	
	(f) Virgin ZnO annealed at 700°C (006) reflection	
Figure 12	2 \times 2, \square Area Maps of Silver Implanted ZnO annealed at 850°C	158
	(a) Silver annealed at 850°C (002) reflection	
	(b) Silver annealed at 850°C (004) reflection	
	(c) Silver annealed at 850°C (006) reflection	
	(d) Virgin ZnO annealed at 850°C (002) reflection	
	(e) Virgin ZnO annealed at 850°C (004) reflection	
	(f) Virgin ZnO annealed at 850°C (006) reflection	
Figure 13	2 \times 2, \square Area Maps of Silver Implanted ZnO annealed at 550°C	159
	(a) Silver annealed at 550°C (002) reflection	
	(b) Silver annealed at 550°C (004) reflection	
	(c) Silver annealed at 550°C (006) reflection	

For the things we must learn before we can do, we learn by doing.
-Aristotle.

2. Capacitance Measurements of Argon Implanted and Annealed ZnO (000 $\bar{1}$) Substrates.

B. T. Adekore^a, D.W. Barlage^b, R.F. Davis^a.

^a Department of Materials Science and Engineering, North Carolina State University,
Raleigh, NC 27695.

^b Department of Electrical and Computer Engineering, North Carolina State University.
Raleigh, NC 27695.

2. 1. Abstract

Capacitance-Voltage measurement is used to determine the electrical characteristics of Argon-implanted and virgin ZnO (000 $\bar{1}$) substrates. Optimal measurement frequencies in series and parallel modes are determined by a three-element circuit model. N_D - N_A carrier concentrations at various annealing temperatures are extracted and consequently the electrical contribution of point defects generated by implantation damage is determined. It was also determined that the implantation of argon and the defects thereby generated do not introduce any new lines to the 8K luminescence spectra. However, the green band luminescence seems to be significantly influenced by argon implantation.

2. 2. Introduction

Accurate capacitance-voltage measurements meticulously performed provide in theory, a quick and non-destructive technique of determining important electronic properties of doped semiconductors. Such properties of particular interest to our studies include the type of minority carriers as determined by the structure of the CV curve and the extracted carrier concentration as determined by mathematical and physical relationships.

However, there exist notable impediments such as the excessive leakage currents due to highly conductive substrates and metal semiconductor interface instabilities due to contaminant adsorption that complicate CV curves. The former typically accounts for the remarkable frequency dependence of the CV curves while the latter contributes to contact resistances in the equivalent circuit

Quasi-static capacitance measurements become very difficult at high leakage currents however, at sufficiently high frequencies the capacitance current becomes dominant and the erroneous capacitance due to the excessive leakage current can be overcome. A complication arises from the very fact that at high frequencies series resistance of the equivalent circuit becomes dominant due to the low impedance of the capacitor [1-2]. Hence, it is necessary to consider the simultaneous presence of both series and shunt parasitic resistances in the capacitance voltage measurement.

ZnO, the material of interest, is a very promising wide band gap semiconductor. It is now well documented that the wurtzite structure material has an energy gap of 3.37eV at 2K and is intrinsically n-type conductive with carrier concentrations ranging from 10^{16} - 10^{17}cm^{-3} . This intrinsic conductivity has been attributed to two possible mechanisms. The

first mechanism being the presence of point defects such as oxygen vacancies (V_o^{2+}), zinc interstitials ($Zn_i^{\bullet\bullet}, Zn_i^{\bullet}$) and zinc anti-sites Zn_o [3]. Of these three donor defects, Zinc interstitials have the lowest formation enthalpy and appear to be the most likely culprit donor defects in the crystal [3]. In general, the role of electrically active point defects in ZnO has been classified into donor-like defects or “hole-killers” such as the defects described above and acceptor-like defects or “electron killers” such as zinc vacancies V_{Zn}'' , oxygen interstitials, O_i'' . These acceptor-like defects have very high formation enthalpies (particularly O_i''), consequently exist in negligible concentrations or do not exist in the crystal at all [3]. However, there could be extraordinary conditions such as ion-implantation that could encourage and indeed sustain the generation of the acceptor-like defects i.e. V_{Zn}'' and O_i'' in significant concentrations.

The second mechanism postulates the unintentional incorporation of ubiquitous Hydrogen during crystal growth. It is posited that hydrogen exists exclusively in the positive charge state in ZnO and the previously accepted culprit defect, (V_o^{2+}), would behave as deep donors [4]. Therefore, the electrically active shallow donors could be positively charge hydrogen produced by the direct interaction of hydrogen with lattice oxygen or the interaction of hydrogen with oxygen defects. However, it is reasonable to attribute the donor conductivity to contributions from both contending hypothesis i.e. the presence of a shallow donor defect as Zinc interstitials as well as unintentional hydrogen. In this work, we use reliable CV measurements to investigate the electrical conductivity of Argon-implanted as well as virgin ZnO bulk substrates at various temperatures. We provide experimental results that allude to the dominance of point defects in the donor

conductivity of implanted and annealed bulk ZnO crystals, especially for the Argon implanted crystals.

2. 3. Experiment

Single crystal (000 $\bar{1}$) Eagle Picher ZnO substrates of oxygen termination implanted by off-axis beams at energy of 230KeV and dosage of 10^{15}cm^{-2} to a depth of 150nm were concomitantly studied with Zn- and O-terminated virgin substrates. Isochronal anneal sequences in 1 atm oxygen for thirty minutes were conducted in a quartz tube furnace. Annealing temperatures was also varied by 50°C from 250°C – 850°C. Electrical measurements were performed using a Mercury probe CV station equipped with a HP Network analyzer 1KHz-1MHz range. The Mercury probes had a probe diameter of 760 μm for the large area ohmic contact and a probe diameter of 15 μm for the small area Schottky contact and a separation distance of 15 μm between the two probes (Figure 1d). Measurement modes were the parallel modes of C_p -D and C_p -G and the series mode of C_s -Q and C_s -D. Table I summarizes the investigated samples and assigned nomenclature as discussed in this text.

The photoluminescence spectra collected at 8K was obtained using a 17mW HeCd laser at 325nm. To achieve thermal contact with the samples, a metallic adhesive was employed. A significant strain of approximately $\pm 0.8\text{meV}$ was introduced into the luminescence spectra as a result of the somewhat arbitrary and non-uniform contraction of the metallic adhesive.

Table I: Processing conditions and identification of Argon Implanted and Virgin ZnO.

Sample	Nomenclature	Termination	Treatment
Argon-Implanted	(i)	Oxygen Grade I	25-850°C, ΔT=50 °C
ZnO Virgin	(ii)	Oxygen Grade I	“
ZnO-Virgin	(iii)	Oxygen Grade II	“
ZnO-Virgin	(iv)	Zinc Grade II	“

2. 4. Theory

Argon implanted and annealed ZnO is studied as the baseline for determining the true contribution of dopants introduced by ion-implantation. Substitutional Argon atoms theoretically should have neutral contributions as a dopant to the conductivity of a virgin substrate since argon is an inert element. Hence, any additional electrical contributions observed from argon doping held in comparison to virgin ZnO can be readily attributed to point defects generated as a result of the implantation damage.

Assuming the depletion approximation and parallel-plate capacitor behavior for the above system, the average charge carrier concentration, $N_D - N_A$, can be obtained using the relationship:

$$N(x_i) = \frac{(C_i + C_{i+1})^3 (V_i - V_{i+1})}{q \epsilon \epsilon_0 (C_{i+1} - C_i) 8A^2} \quad (1)$$

Where C_i and C_{i+1} are two closely spaced capacitances, V_a , the applied voltage, q , the electronic charge, ϵ the dielectric constant and ϵ_0 , the permittivity of free space.

The differential $\frac{dV_a}{dC}$ is given by $\frac{V_i - V_{i+1}}{C_{i+1} - C_i}$ as required from the physical relationship:

$$N(x) = \frac{C^3}{A^2 q \epsilon_0 \epsilon_1 \frac{dC}{dV_a}} \quad (2)$$

The depletion-layer width is given by:

$$x_i = \frac{2 \epsilon_0 \epsilon_1 A}{(C_i + C_{i+1})} \quad (3)$$

In conducting C-V measurements, the techniques elucidated in references 1&2 is applied in this study because of the high n-type conductivity of as-received Eagle Picher ZnO substrates. We adhere to this technique in evaluating the true impedance and capacitance of the implanted and virgin substrates.

Generally, series resistance dominates low-leakage devices obtained from insulating substrates. Accurate capacitances of such devices can be effectively measured by neglecting shunt resistance in the series circuit mode as shown in Fig. 1(a).

Devices with large leakage currents such as those from highly conductive substrates are measured using the parallel mode as shown in Fig.1 (b). The complications that arise in this case, stems from the fact that firstly, the parallel circuit model is frequency dependent and secondly, the measured capacitance decreases with increasing bias due to increasing leakage [1-2]. The frequency dependence can be eliminated with a three-element model consisting of a shunt and series resistance as shown in Fig. 1(c).

The actual capacitance, C, is then determined from this model. The impedance of the equivalent circuit is given by:

$$Z = R_s + \frac{R_p(1 - j\omega CR_p)}{1 + \omega^2 C^2 R_p^2}. \quad (2)$$

The impedance of the parallel circuit model in Fig. 1(b) is given by

$$Z = \frac{D' - j}{\omega C'(1 + D'^2)} \quad (3)$$

Where the dissipation is given by $D' = \frac{1}{\omega RC'}$. D' and C' are the instrument reported values.

By equating the imaginary parts of the measured impedance in (3) and the true impedance (2), the relationship in equation (4) below is obtained.

$$\frac{1 + \omega^2 C^2 R_p^2}{C R_p^2} = \omega^2 C'(1 + D'^2). \quad (4)$$

By measuring the capacitance and dissipation at two different frequencies and substituting into (4), the actual capacitance is obtained as

$$C = \frac{f_1^2 C'_1(1 + D_1'^2) - f_2^2 C'_2(1 + D_2'^2)}{f_1^2 - f_2^2} \quad (5)$$

The above value, the actual capacitance, is the correct capacitance and is used in this study rather than the instrument generated capacitance.

2. 5. Measurement & Results

The eventual goal of obtaining optimal measurement frequencies for accurate CV curves in ZnO systems is attained by a direct three-step procedure:

- Firstly, capacitances are measured at closely spaced frequency intervals.

- Secondly frequency independent measurement regimes are obtained by the aforementioned techniques at the annealing temperatures of interest.
- Thirdly, corrected capacitances are determined using (5) above, at an optimal frequency, f_{opt} i.e. any frequency within the frequency independent regimes at annealing temperatures.

In the equivalent circuit of Fig 1(c), the shunt resistance can also be considered as differential conductance, g , which is strongly bias-dependent as shown by the definition in equation (6) above. As a result, f_{opt} is voltage dependent. However, we simplify the model by evaluating f_{opt} at selected voltages.

The variation of the actual capacitance with frequency is shown in figure 2. The plot is summarized in table II below.

Table II Optimum measuring frequency for reliable Capacitance.

Frequency	Measurement Regime	Voltage
10KHz-100KHz	Excessive Leakage	-3.5V □ 5V
100KHz-300KHz	Optimum	-3.5V □ 5V
300KHz-1MHz	High R_s	-3.5V □ 5V

From this relationship, it is clear that most meaningful capacitance curves in the studied system are obtained at frequencies in the range: $100KHz \leq f_{opt} \leq 300KHz$.

Measurements below 100KHz are unreliable due to excessive leakage current and the premature breakdown of the material. We attribute the premature breakdown to uncompensated defects generated as a result of the Argon implantation. These defects are

engaged at lower frequency and their field-assisted migration within the depletion layer is also greatly enhanced at these frequencies. High frequency unreliability ($f_{opt} > 300\text{Hz}$) is suspected to be due to a non-equilibrium relationship between the response time of the uncompensated defects and the AC capacitance measurement frequency. Instrument generated capacitance values at 250kHz and 150kHz were used in obtaining the actual capacitances shown in values in figures 4, 5, and 6 for each temperature of investigation. The calculated average carrier concentrations from the equation expressed in (1) are shown in Figure 3(i-iv).

2. 6. Discussion

The CV curves shown in Figure 3 (a-b) are categorized into three temperature subdivisions:

- Low temperature region (Fig 4a&b), temperatures from $25^{\circ}\text{C} \leq T^{\circ}\text{C} \leq 350^{\circ}\text{C}$.
- Intermediate temperature region (Fig 5 (a-c)), temperatures from $350^{\circ}\text{C} \leq T^{\circ}\text{C} \leq 600^{\circ}\text{C}$.
- High temperature region (Fig 6 a-c), temperatures greater than 600°C .

2. 6. 1. Low Temperature Region ($T^{\circ}\text{C} \leq 350^{\circ}\text{C}$).

Electrical measurements carried out on Argon implanted samples measured at the as-implanted state i.e. without thermal annealing show dramatically reduced capacitance (figure 4a(i)) because of the initial implantation damage. However, at annealing temperatures in the vicinity of 350°C lattice re-ordering from the damage commences and continues to about 400°C as seen by other investigators as well [5]. This is also consistent

with structural recovery of implantation damage in our other studies by x-ray diffraction techniques [6], where structural recovery via the elimination of implantation-induced satellite peak was observed to occur at 400°C for impurities with atomic masses comparable to that of nitrogen. The CV curves remain of n-type structure within this low temperature region indicating that no carrier type conversion occurred as is expected from an argon implant.

The commencement in repair of the argon-induced damage is seen electrically by an increase in the actual capacitance by three orders of magnitude (from 32pF to 5nF in figure 4a(i) to figure 4b(i) respectively). However, there is a decrease in the $N_D - N_A$ value averaged over the width of the entire depletion region from 10^{19}cm^{-3} to 10^{16}cm^{-3} as seen in figure 3(i). This drastic reduction can be attributed to two mechanisms. The first and more simplistic mechanism involves the gradual and progressive out-diffusion of hydrogen within and from the crystal bulk respectively. However, the detection of hydrogen out-diffusion is quite difficult due to the high detection limit of 10^{17}cm^{-3} in mass spectroscopy techniques. The second and less simplistic mechanism involves thermally activated defect associations occurring by the chemisorption of atomic oxygen and the interactions of the chemisorped oxygen with charged electrically point defects as described below.

2. 6. 1. 1. Oxygen Chemisorption

Chemisorption of oxygen has been reported to be significant at 377°C (650K) [7]. An activation energy of 0.25eV for charge transfer from O_2 to O_2^\square has also been reported [8].

Above 475K (202°C), atomic oxygen has been shown to be dominant by the conversion of O_2^\square to O^\square [8-10]. The chemisorption reaction is



2. 6. 1. 2. Defect Association

By treating damaged samples in thermally activated oxygen ambient, it is possible to facilitate the conversion of charged oxygen vacancies to neutral oxygen by the interaction of these defects with ionized atomic oxygen. The interaction is given by:



The end result is the effective reduction in oxygen vacancy concentration of the argon-implanted substrates at this temperature range (250°C to 350°C). An effective reduction in the N_D-N_A values thus ensues as shown in figure 3(i). The continuous reduction in N_D-N_A values is not sustained at elevated temperatures due to the presence and activity of other favorable defects such as zinc interstitials as we discuss in the following section. However, the speculation that a reduction of oxygen vacancies occurs by annealing in an ambient of activated oxygen is reasonable.

The average N_D-N_A values in the virgin sample remain fairly constant within the 25°C to 350°C range. Fluctuations within same order are observed from $1.5 \square 3.0 \square 10^{17} \text{ cm}^{-3}$ in virgin samples of both polarity and grade as shown in figure 3(ii)-3(iii). Because the decrease in average N_D-N_A values within this temperature range is not as drastic as in the Argon as-implanted case, it is reasonable to conclude that the decrease in average carrier concentration in ion-implanted samples seen below 350°C could involve both the out-

diffusion of hydrogen and very significantly the activity of point defects, in this case oxygen vacancies.

2. 6. 2. Intermediate Temperature Region ($350^{\circ}\text{C} \leq T^{\circ}\text{C} \leq 600^{\circ}\text{C}$).

In the intermediate temperature region, a characteristic surge in average $N_D - N_A$ values in the argon-implanted samples as well as in oxygen-terminated substrates occur. In the argon implant, an increase from the minimum value of $5 \times 10^{16} \text{ cm}^{-3}$ at 350°C to a maximum of $3 \times 10^{20} \text{ cm}^{-3}$ at $550\text{-}600^{\circ}\text{C}$ is observed and shown in Fig 3(i). From this pronounced increase in the carrier concentration values, it becomes clear that hydrogen may not be the chief and only source of the notorious donor conductivity in ion-implanted ZnO. If the preceding were indeed the case, then the conductivity would continuously decrease with progressive out-diffusion of hydrogen as facilitated by increasing annealing temperature. It is thus necessary to turn to the activity of viable point defects for the explanation of the surge in carrier concentration values in both implanted and virgin samples. Zinc Interstitials are particularly attractive as culprit defects because of their lower formation energy relative to oxygen vacancies and because of the convenience of interstitials to migrate or diffuse in and out of the depletion region. Frenkel defects would readily form upon ion-implantation particularly since it is known that the zinc sublattice displaces more readily compared to the oxygen sublattice [14] however, because the apparent increase in average charge concentration is delayed till annealing temperatures above 350°C , one can argue that a charge exchange or activation ($Zn_i^0, Zn_i^{\bullet} \rightleftharpoons Zn_i^{\bullet\bullet}$) of these frenkel defects commences above 350°C and continues to a maximum of $3.0 \times 10^{20} \text{ cm}^{-3}$ at 550°C and 600°C . It is also difficult to isolate which of the

complimentary effects of charge exchange and interstitial generation is the dominant mechanism by which the conductivity increases between 350°C and 600°C. It is most probably the case that both are effectively operative on the depletion region. It seems reasonable that the majority of interstitials are formed by the zinc displacements occurring upon ion-implantation and that these interstitials thereafter undergo a thermally activated charge exchange from neutral to charged interstitials at a particular temperature range (350°C - 600°C) as compared to the concomitant generation of zinc interstitials and charge exchange of these interstitials at this temperature range. However, the increase in average $N_D - N_A$ of oxygen terminated virgin samples within the annealing temperature range ($350^\circ\text{C} \leq T^\circ\text{C} \leq 600^\circ\text{C}$) may indicate a generation of interstitials with increasing annealing temperature. For instance, at 450°C the increase in average $N_D - N_A$ from 3×10^{17} to $7.5 \times 10^{17} \text{ cm}^{-3}$ and from 3×10^{17} to $5 \times 10^{18} \text{ cm}^{-3}$ observed for virgin grade I and grade II substrates respectively, can indeed be attributed to the intrinsic generation of zinc interstitials. Consequently, in the implanted samples it can be suggested that thermally activated charge exchange among ion-implantation induced zinc interstitials is primarily responsible for the surge in average $N_D - N_A$ values and this effect supercedes the thermally activated intrinsic generation of charged interstitials occurring at the same temperature range.

Careful examination of CV curves (400°C-650°C) indicates the decrease in capacitance in both directions of voltage sweep i.e. forward and reverse bias (Figure 5) of both virgin and argon implanted crystals- an attribute referred to as double depletion [11]. Double depletion is indicative of the presence of native defects in high densities acting as interface charges [11]. The CV measurements do indicate that it is possible for point

defects generated during ion-implantation to effectively replicate a Schottky-like barrier in argon implanted samples as seen by diode like curves of samples annealed at 450°C, 600°C and 650°C and shown in figures 5b(i), 5c(i) and 7a(i) respectively. The primary point defects generated during ion-implantation as previously mentioned are prevalent on the zinc sublattice [14]. However, the very significant presence of sub-grain boundaries in ZnO vis-à-vis ZnO-mosaicity as determined by X-ray Diffraction studies (XRD) [6], may facilitate the unequal migration of point defects to and from these sub-grain boundaries. Such contribution of sub-grain boundaries may not be significant in virgin samples wherein excess native defects were not generated. But, in ion-implanted material where the density of implantation generated native defects or excess defects would be very high, sub-grain boundaries, like grain boundaries in polycrystalline ZnO [13] could act as both high diffusivity paths and regions for defect segregation particularly since the native defects in question, zinc interstitials, are highly migrant. Therefore, at certain temperatures, $350^{\circ}\text{C} \leq T^{\circ}\text{C} \leq 600^{\circ}\text{C}$, it is possible that the migration of zinc interstitials to sub-grain boundaries is energetically favorable leaving behind in the single crystal grain, an excess of zinc vacancies which are by nature, less migrant. At the sub-grain boundaries, zinc interstitials would be captured and ultimately annihilated at elevated temperatures ($T^{\circ}\text{C} \geq 650^{\circ}\text{C}$) where their interactions with vacancies and other point defects would be permissible.

In any case, a Schottky-like behavior is achieved by an excess of zinc vacancies within the depletion region because of the migration of compensating donor point defects to the sub-grain boundaries. Thus, the metastable Schottky-like behavior shown in figures 5b(i), 5c(i) and 7a(i) are due to acceptor like defects in excess at these temperatures.

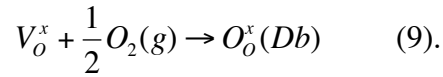
2. 6. 3. High Temperature Region ($T > 600^{\circ}\text{C}$).

The CV curves in this temperature range show a return from the defect induced Schottky like behavior seen in the Argon implanted sample at 650°C to a conductive n-type substrate at 850°C (Figure 6 a-c). The intermediate step at 750°C still indicates a decrease in capacitance with both polarities i.e. double depletion. However, the return from a Schottky to a double depletion structure does indicate a reduction in the densities of the interfacial defect as previously discussed.

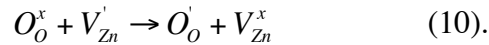
It is very apparent that there is a rapid decrease in $N_D - N_A$ values from the maximum of $3.0 \times 10^{20} \text{ cm}^{-3}$ at 600°C for the Argon-implanted samples to a minimum of $8.5 \times 10^{16} \text{ cm}^{-3}$ at 750°C . Although the $N_D - N_A$ value at 750°C is a local minimum, it is still very significant at $8.5 \times 10^{16} \text{ cm}^{-3}$. Additionally, one could expect a significant out-diffusion of hydrogen at such high temperatures, thus donor point defects may again be responsible for such a high local minimum. The defect reactions subsequently employed have been previously identified by T.K. Gupta [13] in explaining annealing-induced stability of ZnO varistors. The role of sub-grain boundaries is also critical in explaining the defect reactions leading to the carrier reduction in implanted samples because of their behavior as sources and drains for defects. Essentially, the defect reaction leads to the annihilation of zinc interstitials by the interactions described below thereby creating a decrease in the donor conductivity of the crystal. (As described by T.K. Gupta [13]).

2. 6. 3. 1. Activated oxygen-domain boundary interaction:

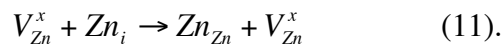
For instance, annealing the crystal in an atmosphere of oxygen at high temperatures ($T > 600^\circ\text{C}$), could encourage the diffusion of oxygen to the sub-grain boundaries. Interaction of diffused oxygen and neutral oxygen vacancies at the domain boundaries produces a sublattice of neutral oxygen at the sub-grain boundaries by the reaction:



The neutral oxygen at the domain boundary immediately captures an electron from the acceptor defect V_{Zn}^{\cdot} due to the high electron affinity of oxygen. The reaction is written as



The charged oxygen defects created by the above reaction stay at the sub-grain boundary. Consequently, neutral zinc vacancies are formed and subsequently annihilated by interacting with highly mobile zinc interstitials which already aggregated at the sub-grain boundaries during annealing at intermediate temperatures ($350^\circ\text{C} \leq T^\circ\text{C} \leq 600^\circ\text{C}$). This interaction facilitates the reduction in both the concentration of both zinc vacancies and interstitials and the formation of a positively charged zinc ion by the expression:



The positively charged zinc ions on the zinc sublattice, Zn_{Zn}^{\cdot} , combine with the negatively charged oxygen ions, O_O^{\cdot} , to form a ZnO sublattice at the sub-grain boundary.

The reaction is written as:



The eventual reduction in zinc interstitials Zn_i^\bullet concentration in the depletion layer is accomplished by the above interactions and consequently the observed rapid decrease in the N_D-N_A values seen from 600°C to 750°C. Above 750°C, there seems to be upward turn in the N_D-N_A -temperature trend in addition to the dominant n-type character of the CV curves of both virgin and implanted substrates. The increase in N_D-N_A values at these temperatures can be accounted for an increase in the generation of zinc interstitials relative to the rate at which the interstitials are compensated by the processes described above. Effectively, the zinc interstitials exist in excess again and thus increase the concentration of charge carriers and the overall conductivity of the crystal at temperatures above 750°C.

2. 6. 4. Optical Properties of Argon-Implanted ZnO crystals.

Photoluminescence conducted at 8K on both argon-implanted and virgin ZnO indicated the most prominent effect of implantation is the suppression of the green band luminescence at certain temperatures. It is quite apparent that in addition to creating a brownish taint to the otherwise transparent crystals, the implantation damage also suppresses the green band even after the brown coloration had been eliminated by thermal anneal ($T \geq 550^\circ\text{C}$). The green emission in ZnO is known to be sensitive to the position of the Fermi energy particularly in donor-doped crystals [15]. Its dominance or suppression therefore may be indicative of shifts in the position of the Fermi Energy possibly due to creation or annihilation of charged defects respectively. In the argon-implanted ZnO, the activity of the green emission was an additional verification of the electronic contributions of charged native defects. The low-resolution photoluminescence spectra of argon-implanted ZnO crystals annealed from the as-implanted state at 25°C to

a recovered state at 850°C with a ΔT of 150°C is shown in figure 8. The excitonic lines are essential quenched in the as-implanted state with the exception of the neutral donor bound exciton (D^0 , X) seen at 3.3407eV. Upon annealing to 250°C, most of the traditional excitonic lines are observable as labeled in the high-resolution photoluminescence spectra of figure 9. The re-activation of the green band commences at 400°C as shown in figure 8c, it gains dominance at 700°C-850°C also shown in figure 8e and 8f. Interestingly, by comparing the relative intensity signals of the green band at the onset and peak of re-activation to the relative intensity signal of the neutral donor bound exciton, it seems that the green emission signal remains about constant. The virtual dominance of the green band emission once re-activated at 400°C, actually seems to be the result of enhancements (at lower annealing temperatures) or quenching (at higher annealing temperatures) of high energy recombination such as that of the donor bound excitons relative to the signal of the green band.

The luminescence of virgin ZnO is also known to be polarity dependent and is discussed in detail elsewhere [16]. Essentially, shifts in the green emission of Zinc terminated crystals are quite pronounced relative to Oxygen terminated crystals. The green emission in oxygen terminated crystals seems to be unaffected by thermal anneal. As mentioned above, it seems that the quenching or enhancements of high energy transition with respect to the green band creates the virtual dominance of the green band in this case as well.

2. 7. Conclusions.

By obtaining an optimal frequency range, it has been possible to obtain meaningful and consistent capacitance-voltage measurements for conductive ZnO single crystals. The

optimal frequency range guarantees frequency independent capacitance that is needed for high current leakage systems.

Temperature dependent variations in the average impurity concentration, N_D-N_A values, in argon-implanted ZnO interpreted in context of the shape and structure of corresponding CV curves and held in comparison to virgin ZnO crystals allude to the following:

- i. Zinc interstitials Zn_i^* are the chief donor native defect in the implanted substrates. They are mostly compensated by acceptor defects such as zinc vacancies (V_{Zn}^+) located at sub-grain boundaries. These interstitials are both thermally and ion-implantation generated.
- ii. Sub-grain boundaries exist in both implanted and virgin samples and function as sources and drains for point defects in ZnO particularly for ion-implanted ZnO.
- iii. Temperature regions exist where zinc interstitials (Zn_i^*) possibly in tandem with hydrogen govern the conductivity of the crystal ($T < 450^\circ\text{C}$), temperature regions where the zinc interstitials dominate the electrical conductivity of the crystals electrically ($450^\circ\text{C} < T < 600^\circ\text{C}$) and finally temperatures where compensation and annihilation of zinc interstitials is favorable ($600^\circ\text{C} < T < 800^\circ\text{C}$).
- iv. Unintentionally introduced hydrogen only partially explains the donor conductivity of the bulk crystals both virgin and implanted because of the high value of the average N_D-N_A at temperatures ($T \geq 750^\circ\text{C}$) where the out-diffusion of hydrogen should be essentially complete.

- v. There effect of argon-implantation on the luminescence spectra of ZnO is centralized on virtual shifts of the green band emission. There were no new lines observed due to the argon implantation.

We thus learn the electrical contribution of ion-implantation to the net conductivity of ZnO single crystals. We also learn for the purposes of activating acceptor dopants, temperature regimes in which such dopants would not be compensated by highly active donor defects, the zinc interstitials (Zn_i^\bullet).

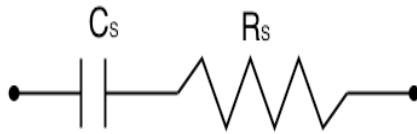
2. 8. REFERENCES:

1. K.J. Yang and Chenming Hu, "MOS Capacitance Measurements for High-Leakage Thin Dielectrics". *IEEE Transactions on Electron Devices*, Vol.46, NO 7 July 1999. Pp1500-1501
2. J.Schmitz, F.N. Cubaynes, R.J. Havens, R. de Kort, A.J. Scholten and L.F. Tiemeijer, "RF Capacitance-Voltage Characterization of MOSFETs with High Leakage Dielectrics," *IEEE Transactions on Electron Devices*, Vol.24, No 1 January 2003. Pp37-39.
3. S.B. Zhang, S.H. Wei and A. Zunger, "Intrinsic n-type versus p-type doping asymmetry and the defect physics of ZnO" *Physics Review B*, Vol. 63, January 2001. Pp75205-1:7.
4. C.G. Van de Walle, "Hydrogen as a Cause of Doping in Zinc Oxide," *Physics Review Letters*, Vol 85 No 5 July 2000. Pp1012-5.
5. B.W. Thomas and D. Walsh, "Anneal Characteristics of ion-implanted ZnO," *Journal of .Physics .D: Appl.Phys.* Vol 6, 1973. Pp 612-5.

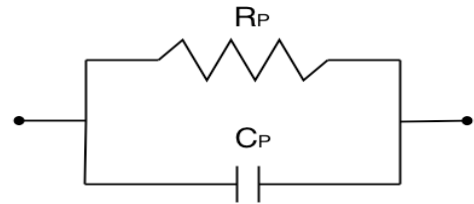
6. B.T. Adekore et al, "Analysis of Structural Damage and Recovery in Ion Implanted ZnO Bulk Crystals" To be published.
7. P. Bonasewicz, W. Hirschwald, and G. Neuman. "Influence of Surface Processes on Electrical, Photochemical and Thermodynamical Properties of Zinc Oxide Films." *Journal of The Electrochemical Society* Vol. **133** No 11 November 1986. Pp 2270-8.
8. D. Eger, Y. Goldstein, and A. Many, *RCA Rev.*, **36**, 1975. Pp. 508.
9. D.Kohl, M. Hennzler, and G. Heiland, *Surf. Sci.*, **41**, 1974. Pp403.
10. W. Gopel, "Reaction of oxygen with ZnO-10 $\bar{1}0$ -surfaces," *Journal of Vac. Sci.Technology* **15**(4) July/Aug 1978. Pp 1298-1310.
11. S.R. Forrest, "Measurement of Energy Band Offsets using Capacitance and Current Measurement Techniques" in "*Heterojunction Band Discontinuities:Physics and Device Applications.*" Edited by F. Capaso and G. Margaritondo. 1987. Elsevier Science Publishers B.V. Pp 311-375.
12. T.K. Gupta, "Microstructural engineering though donor and accpetor doping in the grain and grain boundary of a polycrystalline semiconductor ceramic." *Journal of Materials Research*, Vol. **7** No 12, December 1992. Pp 3280-3295.
13. T.K. Gupta, "Applications of Zinc Oxide Varistors." "*Journal of The American Ceramic Society.*" Vol **73** No 7, 1990. Pp 1817-1840.
14. Y.Ohta, T.Haga, and Y.Abe, *Jpn.J.Appl Phys.* Vol **36** 1997 L1040.
15. R. Kuhnert and R. Helbig, "Vibronic Structure of the Green Photoluminescence due to Copper Impurities in ZnO." *J. of Photoluminescence.* Vol. **26** 1981. Pp 203-6.

16. B.T. Adekore and R.F. Davis, "Extrinsic Donor Conductivity by Implantation of metallic Impurities" To be published.

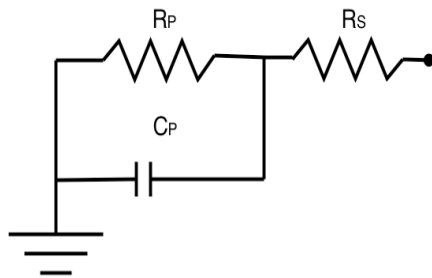
Figures 2.9



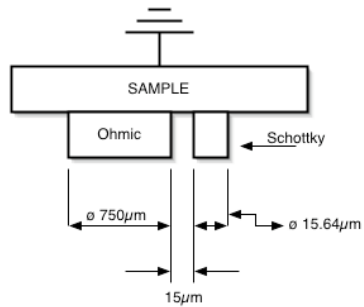
(a)



(b)



(c)



(d)

Figure 1: Small-signal equivalent circuit models for MIS capacitor: (a) series circuit model (b) parallel circuit devices. (c) Corrected model. (d) Measurement schematic of MDC Mercury probe MDC meter.

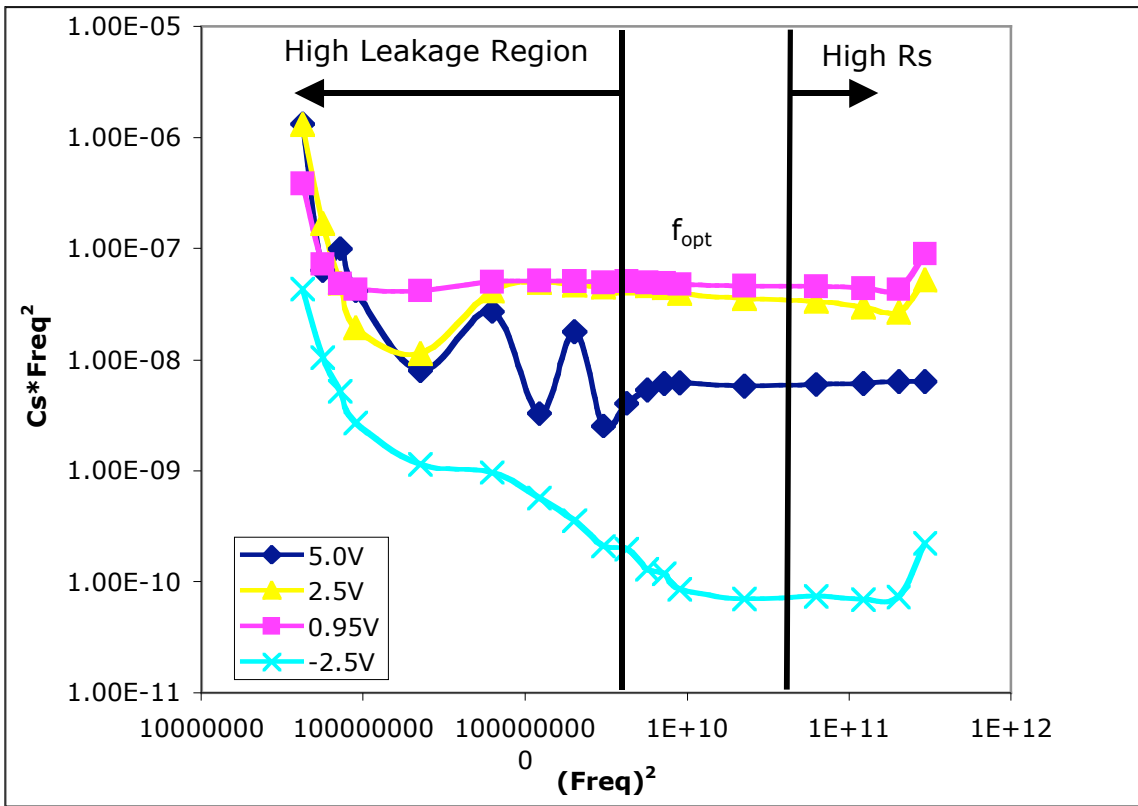


Figure 2: Optimal Measurement Frequency for Selected Voltages showing the High leakage regime, the Optimal regime and the High Series resistance regime.

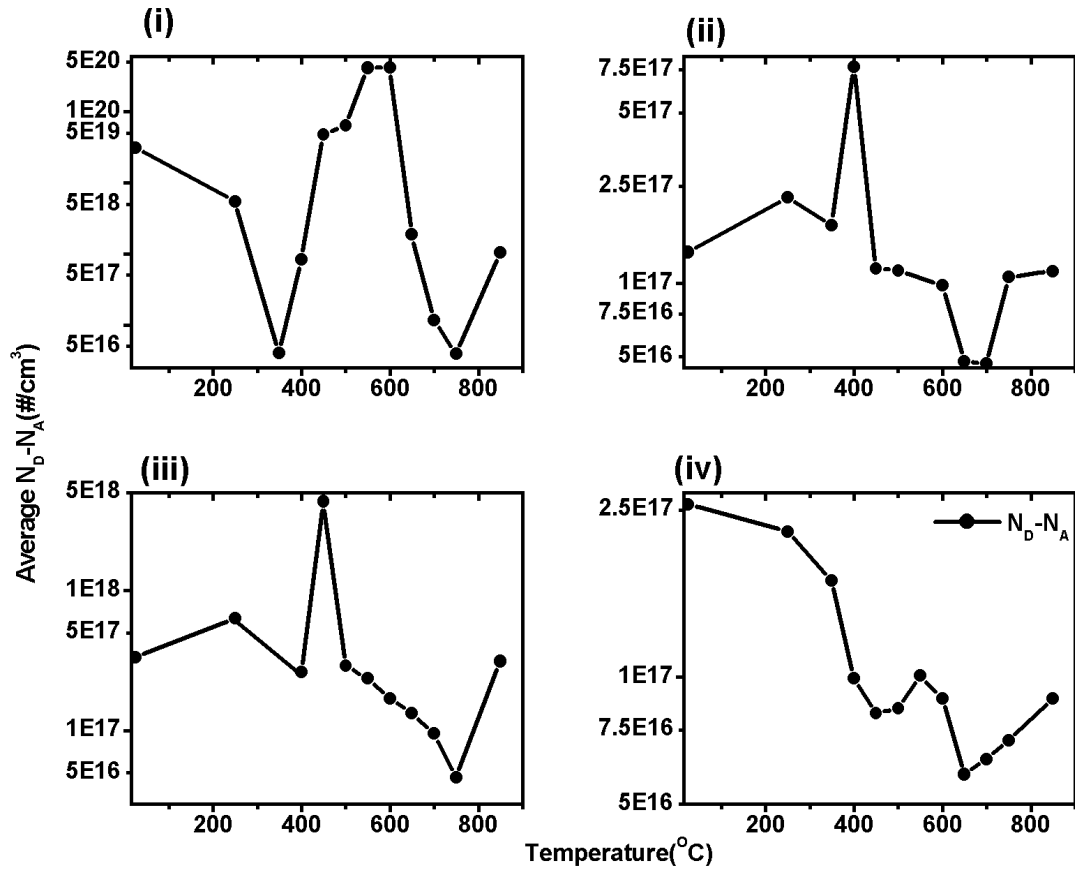


Figure 3: Average $N_D - N_A$ values of (i) Argon-Implanted ZnO (ii) Oxygen Terminated Grade I ZnO (iii) Oxygen Terminated Grade II ZnO (iv) Zinc Terminated Grade II ZnO

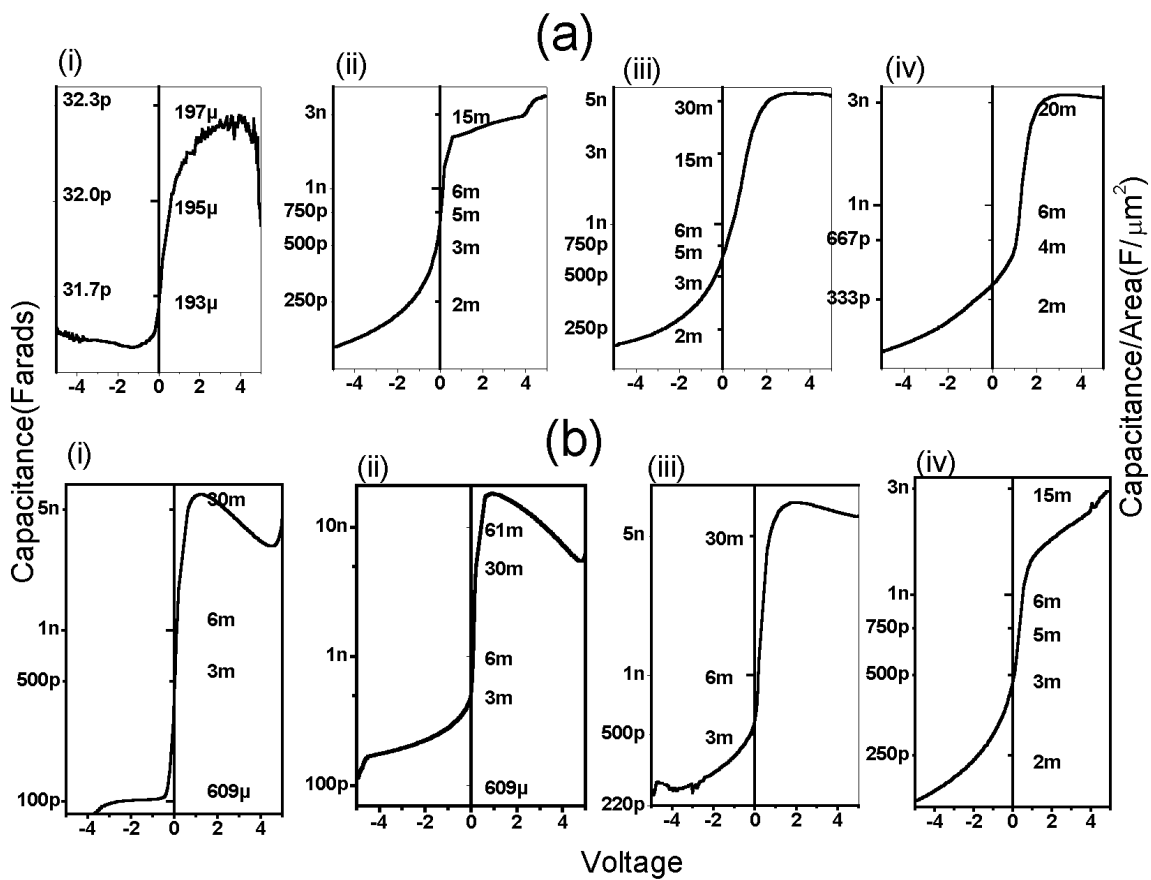


Figure 4(a) and 4(b): CV Plots at 25°C and 350°C respectively of (i) As Implanted samples, (ii) Oxygen Terminated Grade I (iii) Oxygen Terminated Grade II, (iv) Zinc Terminated Grade II substrates.

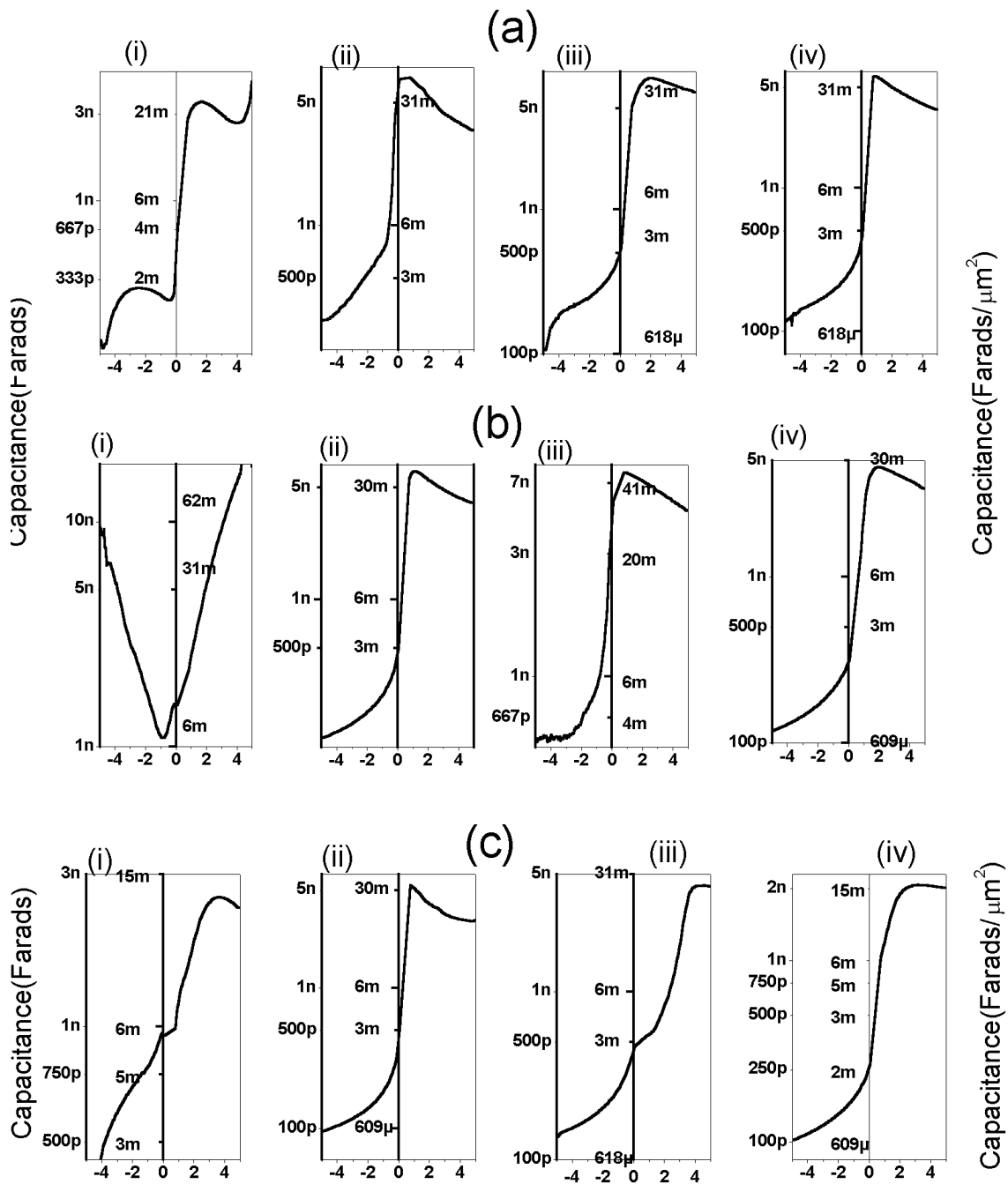


Figure 5a, 5b and 5c: CV Plots at 400°C, 450°C and 600°C respectively of (i) As Implanted samples, (ii) Oxygen Terminated Grade I (iii) Oxygen-Terminated Grade II, (iv) Zinc-Terminated Grade II substrates.

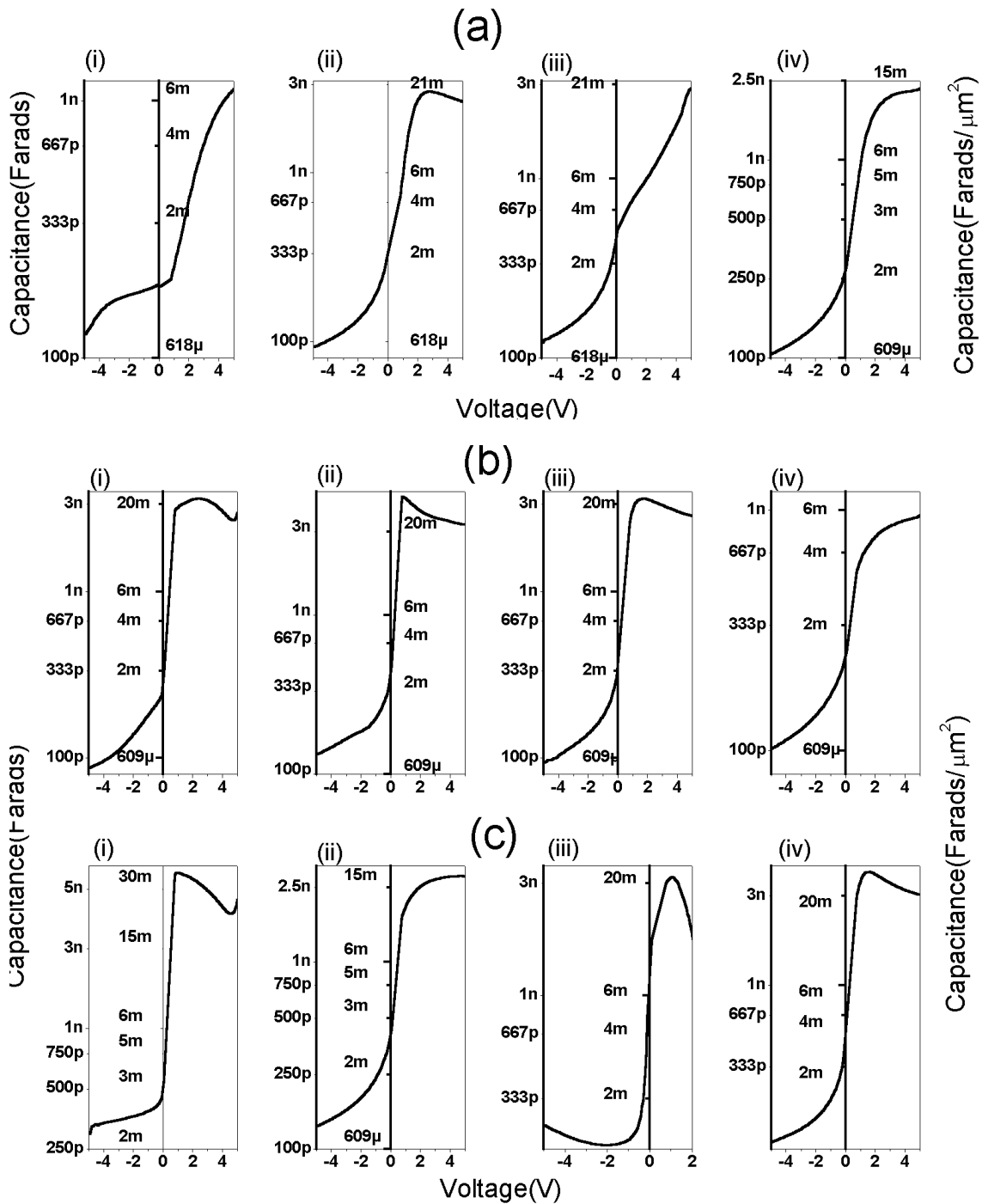


Figure 6a, 6b and 6c: CV plots at 650°C, 750°C and 850°C respectively of (i) As Implanted samples, (ii) Oxygen Terminated Grade I (iii) Oxygen-Terminated Grade II, (iv) Zinc-Terminated Grade II substrates.

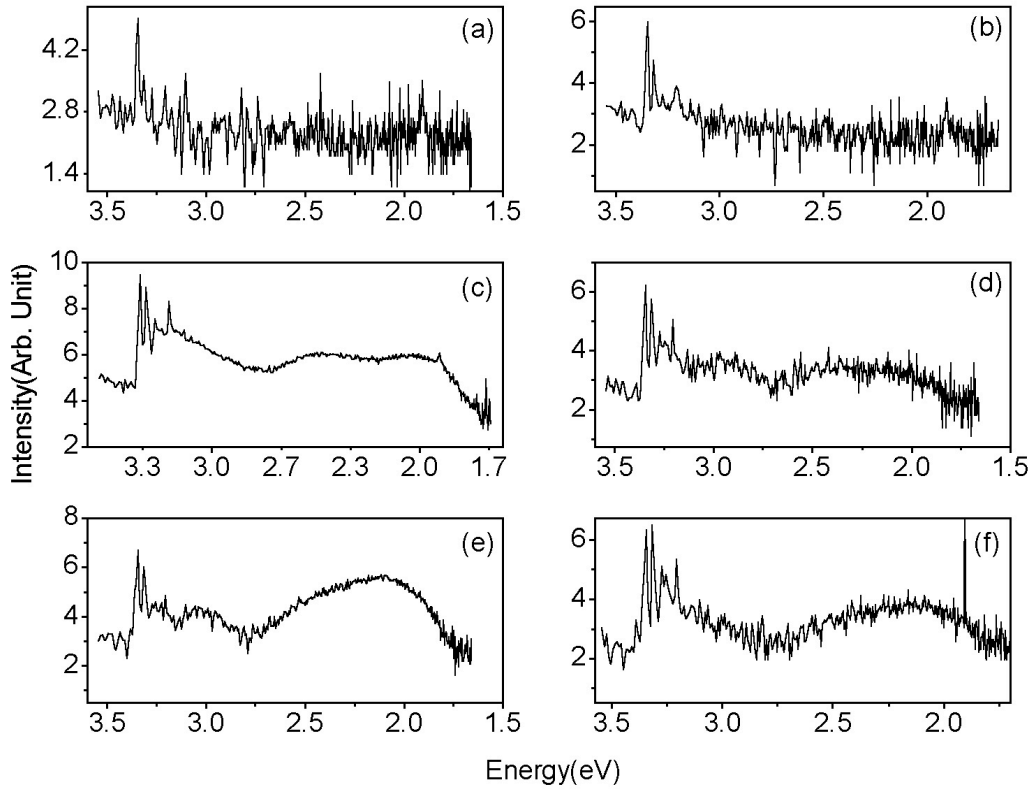


Figure 7: 8K Photoluminescence of Argon Implanted ZnO at low resolution: (7a) As-Implanted samples, (7b) Samples annealed at 250°C, (7c) Samples annealed at 400°C, (7d) Samples annealed at 550°C, (7e) Samples annealed at 700°C, and (7f) Samples annealed at 850°C.

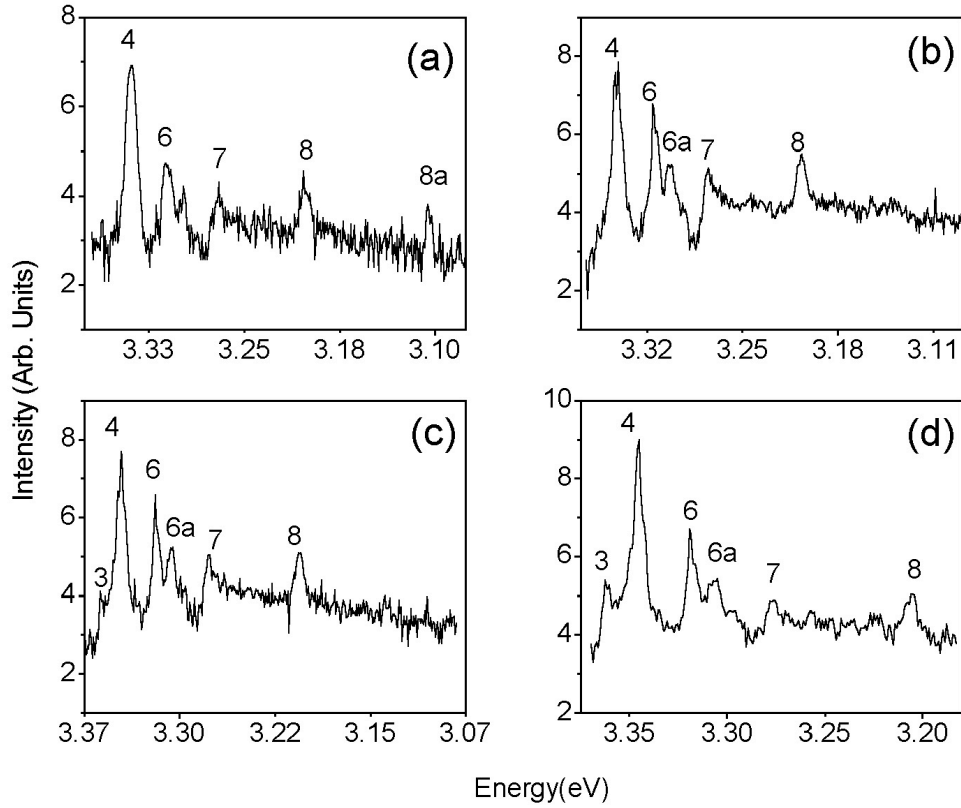


Figure 8: 8K Photoluminescence spectra of Argon-implanted ZnO at High Resolution: (8a) Samples annealed at 250°C, (8b) Samples annealed at 400°C, (8c) Samples annealed at 550°C, and (8d) Samples annealed at 700°C. Excitonic transitions designated as:

- 3 – Rotator Γ_6
- 4 – Neutral Donor Bound Exciton (D^0, X)
- 6 – Two Electron Satellite (TES)
- 6a – Longitudinal Phonon
- 7 – Free Electron to Acceptor Transition (e, A^0)
- 8 – Donor to Acceptor Transition (D^0, A^0)
- 8a – Longitudinal Phonon

3. Acceptor Conductivity in Bulk (000 $\bar{1}$) ZnO via Implantation of Nitrogen Ions.

B.T.Adekore^a, D.W. Barlage, R.F Davis^a.

^aDepartment of Materials Science and Engineering, North Carolina State University,

Raleigh, NC 27695.

3. 1. Abstract.

ZnO (000 $\bar{1}$). Bulk single crystals of intrinsic $10^{17} \text{ cm}^{-3} N_D - N_A$ values were implanted with N^+ ions at dosages of $10^{15} - 10^{16} \text{ cm}^{-2}$ at 95KeV to a depth of 150nm. Subsequent thermal processing result in a p-n structure with activated acceptor concentrations ranging from $10^{17} - 10^{18} \text{ cm}^{-3}$. Electrical characterization by capacitance-voltage techniques reveal diode characteristics of the resulting structure. Photoluminescence conducted at 8K also indicated the enhancement of the donor-bound to acceptor-bound (D^0, A^0) transitions, the suppression of the free electron (e, A^0) to acceptor transition as well as the suppression of the defect related green band at certain temperatures.

3.2 Introduction.

The imperative need for reliable acceptor conductivity in ZnO systems has been recently revived by attractive optoelectronic properties of the wide bandgap material along with copious investigative efforts. Light emitting and Laser diodes in the blue and UV range and UV detectors are some of the desirable but elusive applications of this material. The notable impediment remains the lack of reliable and reproducible p-type conductivity, a consequence of asymmetric doping in wide bandgap materials. ZnO, in this case is preferentially n-type with an energy gap of 3.4eV at 2K [1]. Leading theories as to the nature of this impediment include firstly, compensating native defects which compensates intentionally introduced dopants [2]; and secondly, unintentionally introduced hydrogen which is posited as the prevalent compensating donor defect given the prohibitively high formation energies of native defects [3].

In our work, we empirically argue that native defects are in fact the culprit defects in virgin and implanted samples [4]. These implanted samples in particular, have the added contributions of atoms displaced from lattice into interstitial positions leaving a vacancy behind, in essence a Frenkel defect. An example of such displacement would be that of Zinc atoms from lattice to interstitial positions thereby forming the electrically active donor defects, $Zn_i^{\bullet\bullet}$. The ion channeling work of Ohta et al [5] in which the ease of zinc over oxygen lattice displacements is demonstrated corroborates the foregoing.

Furthermore we have shown that there are temperatures in which the densities of such defects are effectively reduced from maximums as high as 10^{20}cm^{-3} to minimums as low as 10^{19}cm^{-3} [4].

As a result, impurities introduced for the purpose of carrier type conversion, must in principle, exist in concentrations above those of compensating defects at the referencing temperature upon thermal activation. Hitherto, most recent efforts on impurity introduction have been centered on gas-phase introduction or incorporation of impurities during growth. The disadvantage of such techniques is solubility limited incorporation of dopant impurities i.e. impurities cannot be introduced above their equilibrium solubility in the host crystal. Hence it may be difficult to introduce dopant impurities above the densities of the compensating defects. Other recent implantation work has been on focused on codoping whereby metallic (Ga^{3+}) and group V (N) impurities were implanted for substitution on zinc and oxygen sites respectively [6, 7].

In this work, we use ion implantation as a means of introducing dopants above the thermodynamically determined solubility limits thereby ensuring concentrations above those of compensating defects. We observe average acceptor doping from $7.5 \times 10^{17} \text{ cm}^{-3}$ at low temperatures to $2 \times 10^{18} \text{ cm}^{-3}$ at high temperatures indicating ionizations of 1-10% from low to high temperatures respectively. We hereby report acceptor conductivity by implantation of nitrogen in Bulk ZnO crystals.

3.3 Experiment

Nitrogen ions were implanted into Grade I ZnO bulk single crystals, of oxygen and zinc termination as well as grade II oxygen terminated substrates. The major difference is the

average background carrier concentration as we reported in [4]. The grade I substrates have average N_d-N_a values in the range 10^{16} - 10^{17}cm^{-3} , while for the grade II materials average N_d-N_a values of 10^{16} - 10^{18}cm^{-3} was observed for all annealing temperatures. The implantation specifications are 7° of axis implant at 95KeV dosage of 10^{16} and 10^{15}cm^{-2} to peak range of 150nm. Annealing was carried out in a quartz furnace and 1atm oxygen ambient from 25C-850C at 50C increments and from 850-1050C at 100C increments. The samples were subsequently air quenched. The samples were also characterized by Capacitance Voltage techniques at 300K. The procedure outlined in reference [4] was strictly followed with optimum measuring frequencies generated at each measurement temperature. The voltage sweeps were in parallel mode, C_p - G/C_p - D at $\pm 5\text{V}$ and $\pm 10\text{V}$ and the physical relationships expressed in the above reference were used to obtain N_d-N_a profiles. As expected, there was a variation in the optimum frequency with the treatment temperature of the implanted samples. We find the optimal frequencies to be in the decade of 10^4 Hz at low temperature and increasing to the 10^5 Hz decade at high temperatures. Photoluminescence was carried out at 8K using a 17mW He-Cd laser at 325nm. Implantation profiles were also determined by Secondary Ion Mass Spectroscopy (SIMS) as we discuss subsequently.

3.4 Discussion.

3.4. 1. Impurity Selection.

Nitrogen has purportedly, been the traditional choice for acceptor impurities in ZnO. Several observations of acceptor conductivity by the gas phase incorporation of nitrogen in ZnO thin films have been reported [8-10]. We follow the theoretical elucidations of

D.J Chadi [11,13], and S.B. Zhang et al [12,14,16] in selecting acceptor dopants for ZnO via ion implantation. In which case, the superiority of Nitrogen impurities over other group V impurities follows from its higher ionization potential [11] and the fact that this potential exceeds that of the host anion, oxygen. It is very well established that the valence band maximum (VBM) is derived from the anion p-states [13, 29]. In particular, the low energy O 2p orbital pushes the VBM in ZnO very deep to values as deep as 1.53eV and 1eV below that of ZnSe and ZnS respectively [13].

The condition posited by in reference [11], suggests that in order for an impurity to contribute free holes at the valence band, it is essential that the valence p-states of the dopant is more tightly bound than that of the host anion such that it lies below the VBM of the host. In essence, the impurity must have an ionization potential greater than that of the host anion. Physically, Nitrogen is the only anion impurity with an ionization potential above that of Oxygen and may very well be the only anion impurity capable of providing free holes in ZnO. Again, this is because of the deep recess of the VBM attributable to the O 2p orbital. Other anions without this property i.e. $E_{impurity}^{ionization} > E_{host}^{ionization}$, would form deep acceptor states with localized holes and consequently, poor mobility of holes in such samples ensues. [11].

The case for metallic impurities is severely complicated by the contributions of the cation d-orbitals to the valence band character. Lattice relaxations do occur that localize holes (on oxygen atoms) contributed by the substitutional placement of isovalent impurities on cation sites. These hole-induced lattice relaxations of the neighboring oxygen atoms may effectively prohibit the lattice migration of such carriers even under the influence of an applied electric field. Thus, while a comparable ionization potential as that of the host

cation is in fact required of anion acceptors and may contribute to ionization of metallic acceptors in ZnO, there are more pertinent factors governing the ionization of isovalent metallic acceptors in ZnO. Some of these factors include the degree of ionicity, the presence of covalency in the metal-oxygen bond as well as a suitable orbital interaction-p-d orbital interaction. These factors as well as the experimentally favored metallic acceptors are discussed in details in reference 15.

3.4. 2. Implantation Damage and Recovery.

The implantation profile as characterized by SIMS revealed the peak range of 175nm and peak concentration of $5E10^{19}cm^{-3}$. Significant dopant diffusion was observed at only at very high temperatures in the proximity of 1000C (peak concentration of $5.5E10^{19}cm^{-3}$ at 1000C). This was very advantageous in the sense that the dopant atoms are “frozen” in position as structural recovery of the implanted region occur at much lower temperatures effectively allowing direct placement of nitrogen impurities on substitutional sites. In the case of nitrogen, due to its smaller atomic mass in comparison to Argon or Silver for instance, structural recovery was expected and indeed observed at much lower temperatures. We observe structural recovery in the vicinity of 350C by reduction of implantation-induced strain as measured by triple axis X-ray Diffraction [17]. Another inference from the XRD study is the short ranged nature i.e. within one unit cell, of the damage. Additional thermal energy in excess of 350C contributes to the activation of the nitrogen dopant atoms. Photoluminescence at 8K also reveals enhanced luminescence as well as evolution of optical lines as we discuss much later. Figure 1 below shows the implantation profile.

3.4. 3. Diode Behavior.

3.4.3.1. Diffusion Potential and Trap induced Dipoles [18, 19]:

Although ion implantation has the advantage of introducing non-equilibrium dopant concentration, it suffers the inability of creating abrupt junctions as offered by gas-phase incorporation. As a result, the introduced profile is Gaussian and causes notable irregularities wide bandgap materials as ZnO. One of such irregularities is clearly defined regions of high and low dopant concentrations i.e. regions in proximity to the profile maximum (proximare-maxima) and those far from the profile maximum (ante-maxima) respectively. In essence upon thermal activation, the ante-maxima becomes a \mathbf{p}^- region and the proximare-maxima becomes a \mathbf{p} region. Hence, defined junctions are observed between the \mathbf{p}^- and the \mathbf{p} regions. The resulting structure as we show in Figure 1, is a $\mathbf{p}^-/\mathbf{p}/\mathbf{n}$ junction. It becomes readily apparent that the behavior of the implanted junction would be complicated by the different properties of the preceding structure especially by the resistances of transition and neutral regions. A potential is thus introduced as a result of the impurity distribution and can cause accumulation peaks and depletion notches in the N_d-N_a profiles.

Another irregularity due to ion implantation is the enhancement of deep level traps. Deep levels suspected to be present in virgin samples are further enhanced ($N_t \geq 0.1[N_d \square N_a]$) by implantation damage [4]. However, analysis of deep levels is complicated by the severe dependence of their spatial distribution on both measurement frequency and in our case, annealing temperature. In the absence of transient spectroscopy techniques, only phenomenological and qualitative inferences can empirically made. An attribute of deep

donor traps involves the thermal emission of free carriers. By thermal emission, the donor traps emit free carrier within the space charge region. Furthermore, such contributions of free carriers is actively engaged at certain annealing temperatures regardless of measuring frequency (400C-550). Although the temperature dependence in many deep level studies is associated with the measurement temperature, we expect that microstructural details such as the thermally activated chemistry of frenkel defects would make the annealing temperature as relevant even with samples annealed and air-quenched to 300K.

The effective contribution of donor traps to the overall capacitance varies with the intrinsic background concentration of the virgin samples and implantation dosage. Donor trap contributions is most prevalent in grade II samples with average N_d-N_a values of 10^{16} - 10^{18}cm^{-3} and least prevalent in grade I samples with N_d-N_a values of 10^{16} - 10^{17}cm^{-3} , However, the samples with 10^{16}cm^{-2} nitrogen impurities have an higher susceptibility to deep levels presumably because the higher dosage does effect an high densities of Frenkel defects.

For brevity, we highlight the contributions of two physical terms relevant to the behavior of deep levels in p-type ZnO as we observe. Our measurements seem to follow the mechanisms expressed below:

$$N(x_d) = N^{\square}(x_d) \square \square_i u_i(e_{ni}) \frac{x_{ti}}{x_d} \bullet N_{ti}(x_{ti}) \quad (1)$$

where N_{ti} of the i th species of the majority carrier trap having emission rate e_{ni} and trap level crossing the Fermi level at x_{ti} with trap energy E_t , e_{ni} is the emission rate and $u_i(e_{ni})$ is the electrical activity of the traps given by

$$u_i(e_n) = 1 \text{ when } e_n \gg \square$$

(1a)

$$u_i(e_n) = 0 \text{ when } e_n \ll \square$$

The first term in (1) gives the profile due to trap compensation and it involves acceptor and donor traps as well as ionized impurities. We find the term is a function of annealing temperature for the following reasons. Firstly, the degree of impurity ionization increases with annealing temperature and secondly, the trap density profile varies strongly with temperature rising to a sharp maximum at certain temperatures and declining steeply elsewhere.

Consequently, at low reverse bias (or shallow depletion depths) a compensation dip in the N_d-N_a profile is observed, This compensation dip can be attributed to donor traps compensating ionized acceptors. This mechanism is simplified as:

$$N^\square(x_d) = \{N_d(x_d) - N_a(x_d)\} - N_t^{dd}(x_d) \quad (2)$$

where N_t^{dd} is the compensating deep donor defect. $N^\square(x_d)$ thus represent the true net fixed charge distribution from acceptor defects. (substitutional nitrogen and other possible acceptor-like native defects).

The second term in expression 1, gives the fluctuations in free carriers contributed by traps N_{ti}^{dd} in the vicinity of x_{ti} , the position of the traps. The free carrier contributions to $N(x)$ is determined by their electrical activity $u(e_n)$. $u(e_n)$ is related to the angular frequency \square ($\square = 2\square f_{opt}$) by the expression in 1a such that when $e_n \gg \square$, $u(e_n) = 1$ and there is an emission peak corresponding to thermal emission of free carriers from the

deep levels. The subsequent effect in the N_d-N_a profile or more accurately the $N^{\square}(x_d)$ profile, is a rise from the compensation dip to an emission peak due to the thermal emission of free carriers at traps located at x_{ti} .

Figure 2a shows the variation of the emission peak concentration with frequency at 650C for Grade I material and dosage of 10^{16}cm^{-2} ions and figure 2b for Grade II material and dosage of 10^{15}cm^{-2} ions at 650C as well. The trend is such that the maximum emission of free carriers from donor traps is by two orders of magnitude less in the grade I material than in the grade II material. An insight into the spatial distribution of donor traps within the depletion width is also provided in figure 2. The implanted grade I material compared to the implanted grade II samples have a shallower distribution of donor traps within the depletion region as characterized by the position of emission peaks engaged at various frequency. It is seen that x_{ti} , the position of donor traps, vary from 30-100nm in grade I material. This is not the case in implanted grade II material where such donor traps are spread uniformly and deeply into the depletion region. A deep spatial distribution of donors traps of the grade II implant from 145-200nm is shown in figure 2b. Traps below 145nm are not shown here because at the very low frequencies that engage such traps, excessive current leakage interferes with the acquisition of accurate CV data. A crowding of the donor traps is observed in both implanted grades although to a smaller extent in grade II materials. Elsewhere, the traps appear to be uniformly distributed. Donor trap crowding for the implanted grade I material is pronounced between 30nm and 75nm while in grade II crowding occurs between 145nm and 158nm.

Again because of the absence of the transient spectroscopy only a relative quantitative assessment of donor traps can be made. In which case, a compensation factor, \square , is

defined as emission peak concentrations normalized to the virgin carrier concentration [4] at the annealing temperature of interest. Essentially, the compensation factor give the potency of the donor traps in compensating intentionally introduced acceptor impurities. A plot of the compensation factor versus the donor trap positions, x_{ti} shown in figure 3, reveals a triangular profile for the traps in both materials. This triangular profile further reinforces the observed compensation notches and accumulation spikes. Inspection of figure 2b indicates that traps in the crowded region of implanted grade II samples have highest emission peak concentration ($1.15 \times 10^{19} \text{ to } 9.53 \times 10^{19} \text{ cm}^{-3}$) and consequently, the highest compensation factor (120-1000). In grade I material, inspection of figure 2a does indicate the highest compensation factor (34-74) for traps in the crowded region as well. However, figure 2a also shows that there are traps away from the crowded region with an increasing compensation fraction or potency. Pronounced compensation of acceptor impurities is thus expected in regions where the traps are most crowded and in essence have the highest compensation factors.

Finally, dipoles observed in the $N_d - N_a$ profile of activated nitrogen implanted ZnO could be as a result of variations in the distribution of the dopant impurity donor traps with compensation and emission characteristics. Regardless of the source of the dipole, one can deduce the net activated acceptor concentration in both lightly doped or compensated regions (p^+) and uncompensated regions (p). In addition we can tell from the width of the dipole, the width over which the concentration changes from p^+ to p . We now turn our analysis to the CV curves.

3. 4. 3. 2. CV Behavior of N-implanted ZnO at 10^{15}cm^{-2} :

The electrical behavior of the implanted samples (grade I and II) as a function of temperature indicate that the properties of the resulting p/n junction is affected by structural recovery from implantation damage; by deep levels as we discussed above; and by ohmic losses as a result of voltage drop outside the transition region of the diode. In our treatment of the electrical properties of the diode, we examine CV curves at temperature regimes wherein structural recovery occurs, traps are dominant and have the highest densities and finally regimes of stable diode behavior and higher dopant ionization.

3. 4. 3. 2. 1. Structural Recovery Region:

We define the structural recovery region at temperatures form 25C-350C. Initially at 25C, the implanted samples are insulating as we show in figure 4.

The capacitance increases with temperature and the structure of the CV curve indicates the presence of a diode with the forward bias on the **p** /**p** side as shown in figure 4 as well. It is apparent that increasing the dosage to 10^{16}cm^{-2} from 10^{15}cm^{-2} in the grade I samples does improve the diode properties causing a steady diode onset at 250C (figure 4a and 4b). The 10^{15}cm^{-2} samples show steady diode onset at 300C and 350C for grade I and II substrates respectively. It is also noteworthy that at this temperature regime, the degree of acceptor ionization is minimal and ranges from 0.1-1% (figure 8). This is reflected both in the capacitances (maximum of 833pF for grade I and 2nF for grade II at 350C) CV and the N_d-N_a profiles.as shown in figures 4 and 5 respectively. Ohmic losses

are also occur in all the samples particularly at 350C for both grades and dosage of implanted material. N_d-N_a profiles also reveal that depletion occurs all the way to the surface in many cases because of the proximity of the observed dipole to the wafer surface.

Because the features of CV curves in this temperature regime are common not only to the nitrogen implant but to other metallic implants as well may indicate that implantation related effects may be prevalent rather than ionization of dopant impurities.

3. 4. 3. 2. 2. Deep Levels and Trap Dominant Regions:

At intermediate temperatures (400-550C), we observe a very strong frequency dependence of CV measurements in all dosages and grades of the implanted material. This fact coupled with the decrease in reverse capacitance with reverse bias further augments the behavior of deep level donors as emission centers within the space charge region.

The frequency dependence of the grade II material at 10^{15}cm^{-2} and the grade I material at 10^{16}cm^{-2} is such that a local maximum around $V=0$ occurs in the CV curves at low frequencies [19]. The local maximum occurring at 450 for the grade I/ 10^{16}cm^{-2} material (figure 6c (i)-(ii)) and at 500 -550C for grade II/ 10^{15}cm^{-2} material (figure 6e and 6h (i)-(iv)) disappears as the measuring frequency is increased. Also, the donor character of the traps is seen at 450C (figure 6c (iii) and (iv)) where the CV curves closely resemble CV curves for n-type material. Samples annealed at 500- 550C and measured at higher frequency (250KHz) return to a diode structure however suffer significant ohmic losses as the forward bias is increased (figure 6g, (ii), (iii) and 6(i), (iv)). Trap densities are so

high and their contributions so severe in Grade II material that at the very best, only a reduction of the local maximum can be achieved as the measuring frequency is increased from 35KHz to 950KHz. (figure 6e and 6h)

Grade I samples at 10^{15}cm^{-2} do not show a strong influence of high density traps on the reverse capacitance as a local maximum does not exist at low frequencies. This is as expected because the grade I materials have a lower background carrier concentration (n-type) and the added contribution of a higher dosage in generating more donor type defects is absent. Beginning at 450C through 550C, diode behavior with significant ohmic losses is observed. However, the almost linear decrease in reverse capacitance with reverse bias at 500C (figure 6d, (i)) is attributable to some generation of free carriers from donor traps within the depletion region [20].

In concluding the discussion on CV curves in trap dominant annealing regions, we note that the grade I material of both dosages of nitrogen implantation (10^{15} and 10^{16}cm^{-2}) return to steady a diode capacitance structure at temperatures above 500C. In grade II material annealing temperatures between 400 and 550C seem to be dominated by free carrier emissions from deep donor traps. As we have previously alluded to, the annealing temperatures at which donor traps are most active (450-500C in grade I and 450-550C in grade II) coincide with annealing temperature ranges at which donor defects approach maximum values in Argon-implanted samples (400-600C) [4]. Differences in the atomic masses of Argon and Nitrogen may account for the higher temperature shift in argon-implanted substrates.

The ability to return the p/n junction to a steady diode again indicates a reduction in the density of donor traps and or an increased compensation of donor traps by intentional acceptors occurs as the annealing temperatures increases above 500C and 550C for grades I and II material respectively.

3. 4. 3. 2. 3. Elevated Temperature Diode Stability and Dopant Ionization:

Deep donor defects are effectively compensated or reduced by defect annihilation ($N_t \approx 0.1(N_d - N_a)$) beyond 550C for grade I materials (figure 6g and 6i). The true behavior of the diode is again re-established as shown in figures 7 and 8. It is clear from these figures that the diode is most stable at temperatures from 600C –750C in both grades and dosages of the implanted substrates. The grade II substrates however continue to suffer decreases in reverse capacitance from generation centers within the space charge region the space charge region as well as significant ohmic losses from increased conductivity of neutral regions (see below) seen in figure 7b (i) – (iii). The stabilization of diode properties uniformly across all substrates at the above temperatures, maybe due to the combined effect of increased donor defect annihilation and increased degree of ionization of dopant impurities. While grade I substrates of both dosages extend their diode stability to 800C (Figure 8a (ii) and 8c (i) & (ii)), degradation of diode behavior commences at this temperature for grade II substrates. Above 800C the diode behavior of both substrates degrade severely. This degradation could be as a result of a combination of very extensive ohmic losses as well as the onset of new defect mechanisms of donor character. The return of CV curves to curves with n-type semblance tends to favor the latter mechanism. Figure 9 shows the temperature variation of average $N_D - N_A$ at

temperatures were a steady diode has been observed and thus providing the degree of ionization of nitrogen acceptors.

3. 4. 3. 2. 4. Ohmic Losses:

A dominant effect we observe at all annealing temperatures but particularly at higher temperatures is the slowly increasing or in some case, decreasing forward capacitance of the diode with increasing external voltage. We attribute this effect to ohmic losses (OHL, hereafter). Typically, it is assumed that the resistivity of neutral region of the diode is low due to high doping and consequently, the voltage drop across the neutral regions is negligible. However, we attribute the losses in forward capacitance to a voltage drop outside the transition region of the diode. The voltage drop in these neutral regions is depends on the current through the device and ultimately, on the voltage across the junction. In our case, we can represent the junction voltage by

$$V = V_a - I \left(\underbrace{R_{p^-}(I) + R_{p^+}(I)}_{R_p(I)} + R_n(I) \right) \quad 3$$

where $R_p(I)$ is the total resistance due to regions p^- and p^+ and $R_n(I)$ the resistance of the n region. V_a is the applied external voltage.

As the current increases, the voltage drop across R_p and R_n increases and consequently the voltage across the junction consequently decreases. As a result of this decrease in junction voltage, carrier injection is lowered and thus, the forward capacitance increases more slowly (or in some cases, decreases) with increased external bias.

3.5 Luminescence Spectroscopy.

Low temperature (8K) photoluminescence conducted on the nitrogen-implanted samples of both termination was held in comparison to argon implanted and virgin samples of oxygen termination. Generally, we observe traditional excitonic transitions in virgin ZnO such as the free exciton transitions (FE), the donor-bound exciton transitions (D^0, X), the corresponding two electron transitions (TES) as well as the corresponding LO phonons with LO phonon energy of 72.2meV. There is an uncertainty as to the nature of the line at (3.3476eV) which has been classified as a donor-bound transition by Reynolds et al [21] and an acceptor bound transition by Gutowski et al and others as well [22]. We also observe the free electron to acceptor transition (e, A^0) and the donor-bound to acceptor bound transition (D^0, A^0) We label the above lines in figures in which they are most resolved throughout our subsequent illustrations.

3.5.1. Hydrostatic Strain Effects in Oxygen terminated Substrates:

In determining the true contributions of nitrogen to the luminescence spectra, it is important to compare the nitrogen and argon spectra relative to that of virgin ZnO of oxygen termination (denoted as O-ZnO hereafter) at all annealing temperatures. In which case we expect and indeed observe the strain contributions of nitrogen to be similar to that of argon because of their comparable atomic masses (figure 11) and acceptor transitions enhanced by substitutional nitrogen to be minimal or absent in the argon spectra (figure 10 a-f).

The behavior of the implanted and annealed luminescence spectra is affected firstly; by the presence of internal built-in strain in virgin ZnO bulk crystals [23] secondly; by the strain introduced through ion-implantation itself and thirdly; by hydrostatic compression of ionized nitrogen substituting on oxygen vacancies. Wherein for hydrostatic compression, the radius of ionized nitrogen, N^{3-} , is given as 1.71\AA and that of oxygen as 1.32\AA . Since impurity ionization varies from 0.1-6%, there is a significant distribution of unionized nitrogen in interstitial and lattice sites wherein hydrostatic tension contributions is quite possible i.e. atomic nitrogen (0.77\AA) on ionized oxygen sites (1.32\AA) results in a tensile state.

The effect of the built-in strain in O-ZnO is shown in figure 11a (i). Herein, the D^0 , X line initially redshifts to lower energy lines at temperatures between 25 and 250C. The line then blueshifts to higher energy lines at temperatures between 250C and 700C. A quite significant redshift is observed between 700C and 850C. An increasingly significant dominance of the green band with temperature is also observed but discussed elsewhere [24]. Hence, in O-ZnO, the built-in compressive state seems relieved by treatment below 400C, but especially by treatment between 700C and 850C. The foregoing character of the built-in strain is expected to be superimposed on any strain contributions from a substitutional dopant such as nitrogen. Relative to O-ZnO, D^0 , X lines are significantly redshifted to lower energy lines in nitrogen and argon implanted substrates at all annealing temperatures. A maximum shift of 16.7meV (figure 11c (ii)) is however observed at 400C for the nitrogen implanted samples. The trend is similar for the argon implant in which an expectedly larger redshift of 19.3meV (figure 11c (i)) is also observed at 400C.

It is apparent that an absolute compressive state i.e blueshifts of D^0 , X in implanted samples to energies higher than that of D^0 , X in O-ZnO is only observed at temperatures the vicinity of 1000C. What is observed prior to 1000C, is a gradual shift from a locally tensile state or low energy lineshift ($T^0C < 400C$) to a locally compressive state or high energy lineshift ($400 < T^0C < 500C$) and then a tensile state again ($T < 850C$) as shown in figure 11a (ii) and (iii) for nitrogen and argon implanted samples respectively. These shifts could be as a result of strain alleviation either by the incorporation of nitrogen atoms or alleviation of implantation induced strain. Interestingly, the local maximum occurring at 550C coincides with the temperature range in which we have observed maximum contributions from electrically active point defects. This again makes another case for the activity of point defects in which case their compressive contributions at 550C is less dramatically relieved by strain contributions from dopant incorporation or implantation itself. The strain state returns to a tensile state between 550C and 850C as shown in 10a, probably because of a reduction in the concentration of point defects and thus their contributions to the built-in strain. In O-ZnO, it seems the compressive state is maintain almost constantly at temperatures from 400C through 700C. Beyond 700C, there is a sharp shift in the D^0 , X line to lower energy lines [23] with the lowest shift occurring at 1000C as shown in figure 10a (i). It is difficult to distinguish the strain contributions due to dopant incorporation from that due to ion implantation at lower temperatures. However, the upward turn of D^0 , X lines to higher energies beyond 700C in the implanted material makes a case for strain contributions as a result of dopant incorporation. This is augmented primarily because lineshifts in O-ZnO indicate that the built-in strain has been significantly alleviated above 700C, thus any further strain

contributions at this temperature range has to be an extrinsic effect. Secondly, the fact that this upward turn is significantly more pronounced for nitrogen than for argon corroborates the contributions from dopant incorporation rather than that from implantation strain. In addition, because of the higher degree of dopant ionization at higher temperatures, one expects and observes a pronounced strain contribution from of substitutional nitrogen on oxygen sites at this temperature range.

3. 5. 2. Hydrostatic Strain Effects in Zinc Terminated Substrates:

We mention very briefly the strain behavior in Zinc terminated substrates (denoted as Zn-ZnO hereafter). Figure 10c shows the pattern of lineshifts in Nitrogen implanted Zn-ZnO and virgin Zn-ZnO. In which case, we observe continuous redshift of the D^0 , X line with increasing annealing temperature in virgin Zn-ZnO (Figure 10c (i)). It is apparent that there is a gradual redshift or alleviation of built-in strain from 25C-400C, a steeper redshift between 400C and 550C and thereafter a gradual decline is again observed to 850C. Therefore, it is reasonable to conclude that a continuous alleviation of the built-in strain occurs on the zinc face possibly because of the significantly less defect concentration in this termination [4] and thus a reduced strain contribution. The nitrogen implant somewhat replicates this behavior (figure 10c (ii)). In which case, the notable features include a similarly steep decline between 250C and 400C, and an upward turn beyond 700C (absent in virgin Zn-ZnO). This upward turn is again attributable to compressive strain contributions as a result of increased dopant incorporation or ionization.

3. 5. 3. Enhanced Acceptor Transitions and New optical lines:

Identification of uniquely new optical lines due solely to acceptor transitions is complicated by several factors including strain initiated lineshifts, However, prominent acceptor transitions have been noted for firstly, the free electron to acceptor (e, A^0) at 3.2898eV [23], 3.236eV [25] and in this work $3.2789 \pm 0.001\text{eV}$ and secondly, for the donor-bound to acceptor bound (D^0, A^0 or DAP) transition at 3.2176eV [23], 3.22eV[25] and in this work, $3.2089 \pm 0.024 \text{ eV}$. The free electron transition occurs as electrons contributed by thermally ionized donors recombine with acceptors associated with the second valence band or the B-valence band while the (D^0, A^0) transition occurs as a donor-bound-acceptor bound exciton collapses. In the case of the D^0, A^0 , the acceptor is associated with the first valence band or the A-valence band.

In this study, an increase in the intensity and dominance of the DAP line in nitrogen implanted samples over other acceptor transitions was observed with increasing annealing temperatures. Also observed was a concomitant decrease in the intensity of the free exciton to acceptor transition (e, A^0) with increasing annealing temperature as highlighted in Figure 10a-f. The foregoing increase in prominence of the DAP or D^0, A^0 transitions over e, A^0 transitions for nitrogen implanted samples is not observed in virgin O-ZnO or Zn-ZnO with the case for O-ZnO shown in figure 10. Acceptor transitions in virgin samples do not appear to be enhanced with increasing annealing temperatures and the line intensity of such acceptor transitions remains approximately the same from 25C through 850C. Above 850C, the lines are completely extinguished in virgin samples of both termination, what is prominent at such high temperatures is luminescence from the defect or green band. Acceptor transitions evolve very differently in nitrogen and argon

implanted samples although to a less pronounced extent for the argon samples. The DAP lines are particularly enhanced from 550C to 1000C for the nitrogen implanted samples relative to virgin samples. Free electrons to acceptor transitions were observed to diminish in intensity with increasing temperature. Such decreases in e, A^0 intensity are most probably due to a decrease in the concentration of effectively ionized donor defects. Donor defect concentration could be effectively reduced either by the thermally activated donor defect annihilation as discussed in reference [4] or by an increase in concentration of ionized and compensating acceptors i.e substitutional nitrogen on oxygen sites or vacancies. The net effect is an overall reduction in number of free electrons available to transition to acceptor levels and consequently an effective reduction in the relative intensity of the e, A^0 line. The acceptor binding energy to the first and second valence band A- and B bands respectively can be deduced using the theoretical value of bandgap energy, 3.436 and 3.4465 for the A and B-bands respectively. In which case for the B-band, the e, A^0 line of 3.2789 yields an acceptor binding energy of 168meV close to other observed values of 157meV [23,25]. And for the A-band an acceptor binding energy of 167meV after considering the donor binding energy of 60meV and the DAP line at 3.2089eV.

We also observe a broad band at 3.0795 ± 0.001 eV from 25-850C. The broad band shifts to a pronounced and strong line above 850C. This new line with linewidth of 35meV occurs at 3.0587 above 850C and relatively strong at 1000C. The line may be due to another acceptor transition as it is unique only to nitrogen-implanted samples. The fact that this line is strong at very high temperatures, allude to a correlation with the degree of ionization of dopant nitrogen. In the case of an acceptor transition for this line, an

ionization energy of 377meV (assuming transitions to the A-Valence band with bandgap energy of 3.436eV) indicates the line may correspond to significantly less shallow acceptor levels.

3. 5. 4. Green Band Luminescence.

Broadband luminescence centered at 2.45-2.50eV, also known as the green band luminescence was also observed in both implanted and virgin ZnO. The behavior of this ubiquitous band for Argon implanted and virgin samples where the argon implant is representative of the green band (GB) behavior of other implanted impurities, is discussed elsewhere [24, 26]. However, we note in this work the significant increase in green band dominance above 700C for implanted and virgin samples. We also note that in virgin samples annealed above 900C, GB luminescence is essentially the only observable luminescence with other transition being significantly quenched.

Figure 10g shows the spectra at 1000C for the nitrogen implanted and virgin O-ZnO samples. Wherein we observe the quenching of excitonic transitions above 850C for virgin samples. Excitonic transitions in nitrogen-implanted samples seem relatively unaffected at this temperature range as shown in figures 10g and 10h. We have observed the suppression of the GB at temperatures below 850C for the nitrogen implanted sample although at 550C the GB begins to increase in intensity but still relatively suppressed.

With an onset at 550C, the GB reaches maximum intensity at 1000C.

The fundamental origin of the GB is as a result of vibronic transitions involving a transition from the conduction band or a shallow-donor level D, to a deep level, A.

Susbtitutional copper impurities Cu^{2+} have been suggested through EPR and

luminescence studies as a possible culprit for deep levels because of the zero phonon line [27]. However other arguments support the activity of native defects such as zinc and oxygen vacancies [26, 28]. The ability to suppress the green band by ion-implantation and thermally activate it again at elevated temperatures tends to favor contributions of native point defects. In which case, the effective compensation or annihilation of such deep level native defects would tend to suppress GB luminescence. At elevated temperatures where the concentration of the native defects is maximal we expected and observed the onset of GB luminescence. After the onset, the GB gains intensity to a maximum at such elevated temperatures as 1000C where the rate of compensation and annihilation of native defects is much smaller than the rate of generation of such defects. An appendix for low and high resolution 8 Kevin photoluminescence has been attached showing the development of the N-Line as well as identifying the traditional optical transitions.

3.6. Conclusions

In conclusion, we note that nitrogen ions implanted into O-ZnO and Zn-ZnO are thermally activated with a degree of ionization varying from 1-10%. We observe by capacitance-voltage techniques diode characteristics due to p-layer from activated nitrogen acceptors and n-layer from intrinsic n-type conductivity of bulk substrates. We observe the presence of electrically active donor traps which act as deep levels. Finally, we observe optically, the enhancement of acceptor transitions at 3.2089eV and the presence of a uniquely new line at 3.0587eV as well as the suppression of green band luminescence at temperatures below 850C.

3.7. References:

- [1] D.C. Look, "Recent Advances in ZnO materials and Devices".
- [2] S. B Zhang, S.H Wei, A. Zunger, "Intrinsic n-type versus p-type doping asymmetry and defect physics of ZnO" *Physical Review B*, Vol. 63, Jan 2001.
- [3] Van de Walle, C.G, "Hydrogen as a cause of Doping in Zinc Oxide", *Physical Review Letters*, Vol.85, No 5 July 2000.
- [4] B.T. Adekore, D.W. Barlage, R.F Davis, "Capacitance Measurements of Argon Implanted and Annealed ZnO (000 $\bar{1}$) substrates". In press.
- [5] Y. Ohta, T. Haga, Y. Abe, "Crystallographic Features of ZnO single crystals", *Jpn J. Appl Phys* 36, L1040-L1042, Part 2, No8H, 1997.
- [6] M. Joseph, H. Tabata, T. Kawai, "p-Type Electrical Conduction in ZnO Thin Films by Ga and N codoping". *Jpn J. Appl Phys*. Vol. 36, L1205-1207, Part 2, No 11A. Nov. 1999.
- [7] M. Kamatsu, N, Ohashi, I. Sakaguchi, S. Hishita, H. Haneda "Ga, N Solubility limit in co-implanted ZnO measured by secondary ion mass spectroscopy. *Appl. Surface Science* 7760 (2002) Pp 1-4.
- [8] K. Minegish, Y. Koiwa, "Growth of p-type ZnO Films by Chemical Vapor Deposition." *Jpn. J. Appl. Phys*. Vol. 36. Pp L1453.
- [9] Look, D.C "Characterization of homoepitaxial p-type ZnO grown by Molecular Beam Epitaxy". *Appl. Phys. Letters*, Vol 82, Issue 10, Pp 1831, Feb 2002.

- [10] A.B.M. Almamum Ashrafi, I. Suemune, H. Kumano and S. Tanaka, "Nitrogen-Doped p-Type ZnO Layers Prepared with H₂O Vapor-Assisted Metalorganic Molecular-Beam Epitaxy." Jpn. J. Appl. Phys. Vol. 41 (2002) Pp L1281-1284.
- [11] D.J. Chadi, "Column V Acceptors in ZnSe: Theory and Experiment", Appl. Phys. Lett. Vol 59, No 27, Pp 3589-91, Dec. 1991.
- [12] S.B Zhang, S.H Wei, A. Zunger, "A phenomenological model for systematization and prediction of doping limits in II-VI and I-III-VI₂ compounds". Journal of Appl. Phys., Vol 83, No 6, Pp 3192-6, March 1998.
- [13] D.J. Chadi, M.L Cohen, "Tight Binding Calculations of the Valence Bands of Diamond and Zinc Blende Crystals". Physica Status Solidi (B), Vol 68, No 1, Pp 405-416, March 1975.
- [14] S.B Zhang, S.H Wei, A. Zunger, "d-band excitations in II-VI semiconductors: A broken symmetry approach to the core hole". Physical Review B, Vol 52, No 19, Pp 13975-13982 Nov. 1995.
- [15] B.T. Adekore, D.C. Look, R.F Davis, "Acceptor conductivity in bulk ZnO (0001) single crystals via ion-implantation of metallic impurities". In Press.
- [16] H. Kawazoe, H. Yanagi, K. Ueda, H. Hosono, "Transparent p-Type Conducting Oxides: Design and Fabrication of p-n Heterojunctions", MRS Bulletin, August 2000. Pp 28-36.
- [17] B.T. Adekore et al, "Damage Mechanisms of Implanted ZnO investigated by X-ray Diffraction and Synchrotron Studies". To be published.

- [18] P. Blood and J.W. Orton, "The Electrical Characterization of Semiconductors: Majority Carriers and Electron States". Academic Press Inc. San Diego 1992. Pp 220-335.
- [19] S.R. Forrest, "Measurement of Energy Band Offsets using Capacitance and Current Measurement Techniques" in "*Heterojunction Band Discontinuities: Physics and Device Applications.*" Edited by F. Capaso and G. Margaritondo. 1987. Elsevier Science Publishers B.V. Pp 311-375.
- [20] B.G. Streetman, "Fabrication of p-n Junctions" in "*Solid State Electronic Devices*". Prentice Hall, New Jersey 1972.
- [21] D.C. Reynolds, D.C Look and B. Jogai, " Neutral-donor-bound-exciton complexes in ZnO crystals" Physical Review B, Vol 57, No 19. May 1998. Pp 12151-12156.
- [22] J. Gutowski, N. Presser and I. Broser, "Acceptor-exciton complexes in ZnO: A comprehensive analysis of their electron states by high-resolution magneto-optics and excitation spectroscopy", Physical Review B, Vol 38, No 14, Nov. 1988. Pp 9746-58.
- [23] D.C, Reynolds, D.C Look, B. Jogai, R.L Jones, C.W. Litton, W. Harsh and G. Cantwell, "Optical properties of ZnO crystals containing internal strains", Journal of Luminescence, Vol 82 1999, Pp 173-6.
- [24] B.T. Adekore , R.F Davis: "Enhanced Green Band transitions in Implanted and Annealed ZnO substrates". To be published.
- [25] K. Thonke, Th. Gruber, N. Teofilov, R. Schonfelder, A. Waag, R.Sauer. "Donor-acceptor pair transitions in ZnO substrate material" Physica B. Vol 308-310. 20001 Pp 945-8.

- [26] D.C Reynolds, D.C Look and B. Jogai, "Fine structure on the green band in ZnO".
Journal of Appl. Phys. Vol. 89 No 11. June 2001. Pp 6189-91.
- [27] R. Kuhnert and R. Helbig, "Vibronic structure of the green photoluminescence due
to copper impurities in ZnO". Journal of Luminescence, Vol. 26, 1981, Pp 203-6.
- [28] F. H Leiter, H. R Alves, A. Hofstaetter, D.M Hoffmann and B.K, Meyer. "The
oxygen vancancies as the origin of a Green Emission in Undoped ZnO".Phys. Stat. Sol.
B. Vol 226, No1, 2001, Pp R4-R5.
- [29] S. Wei, A. Zunger, "Role of d Orbitals in Vavlence-Band Offsets of Common-Anion
Semiconductors". Physical Review Letters. Vol. 59, No 1. July 1987. Pp 144-7.

3. 8. Figures

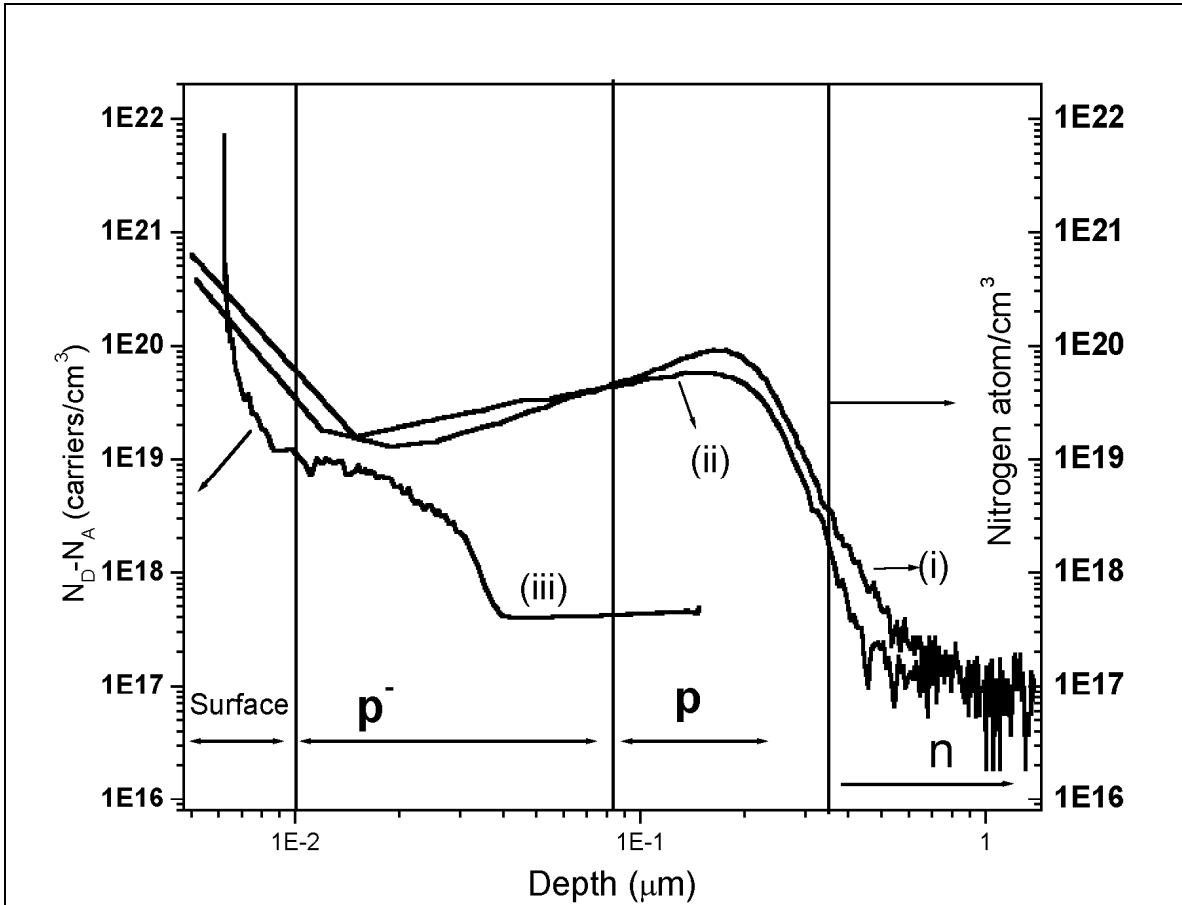


Figure 1: Impurity and Free-Carrier profile for Nitrogen Implanted and Virgin ZnO. (i) SIMS profile for as-implanted Nitrogen. (ii) SIMS profile for implanted and annealed at 1000°C and (iii) $N_D - N_A$ profile for grade II virgin samples of oxygen termination.

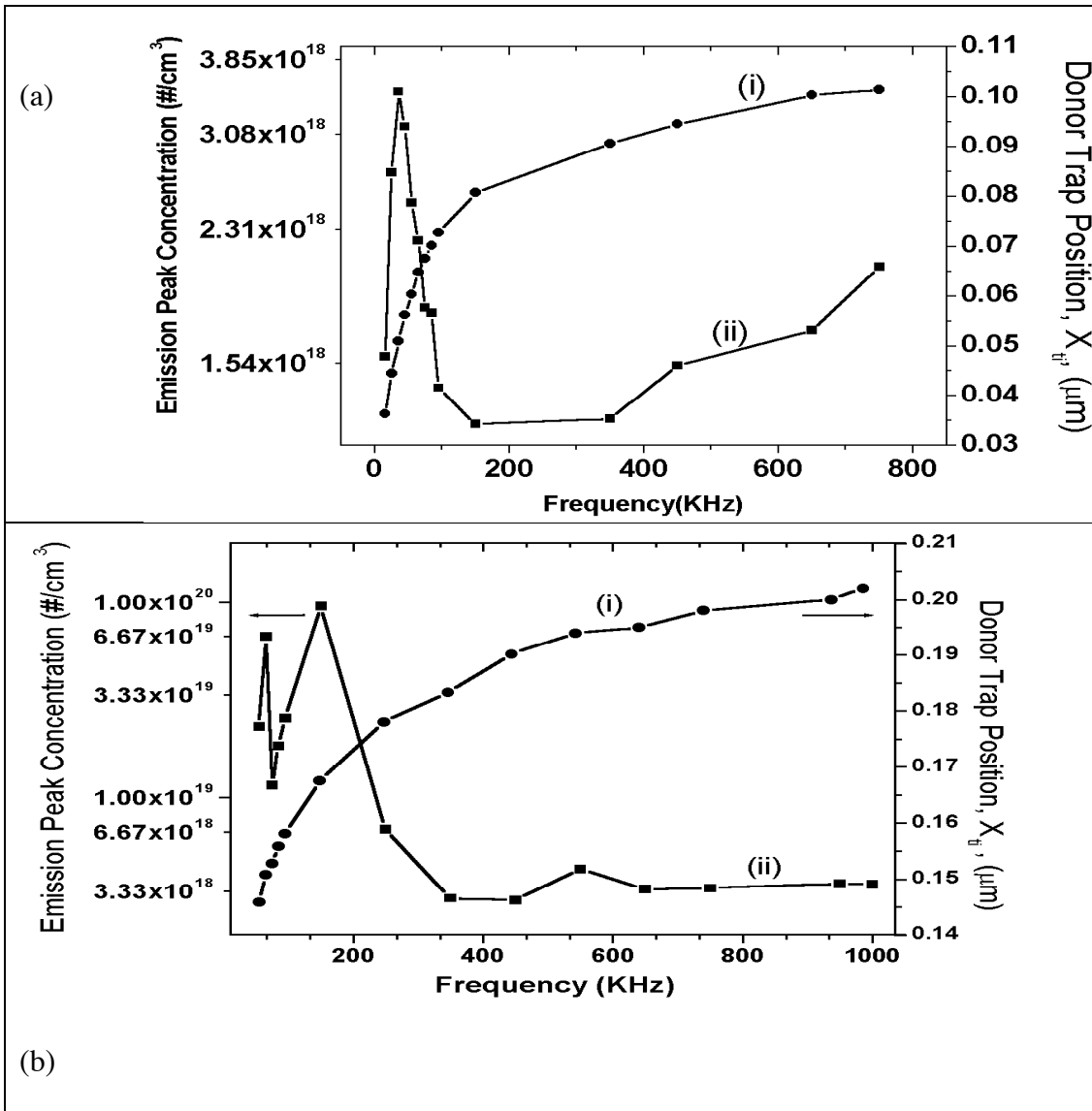


Figure 2a: Variation of Donor Traps Emission Peak Concentration and Position with Frequency for implanted Grade I material at 10^{16}cm^{-2} of Nitrogen. (i) Emission peak positions (μm). (ii) Emission peak concentration ($\#/\text{cm}^{-3}$).

Figure 2b: Variation of Donor Traps Emission Peak Concentration and Position with Frequency for implanted Grade II material at 10^{15}cm^{-2} of Nitrogen. (i) Emission peak positions (μm). (ii) Emission peak concentration ($\#/\text{cm}^{-3}$).

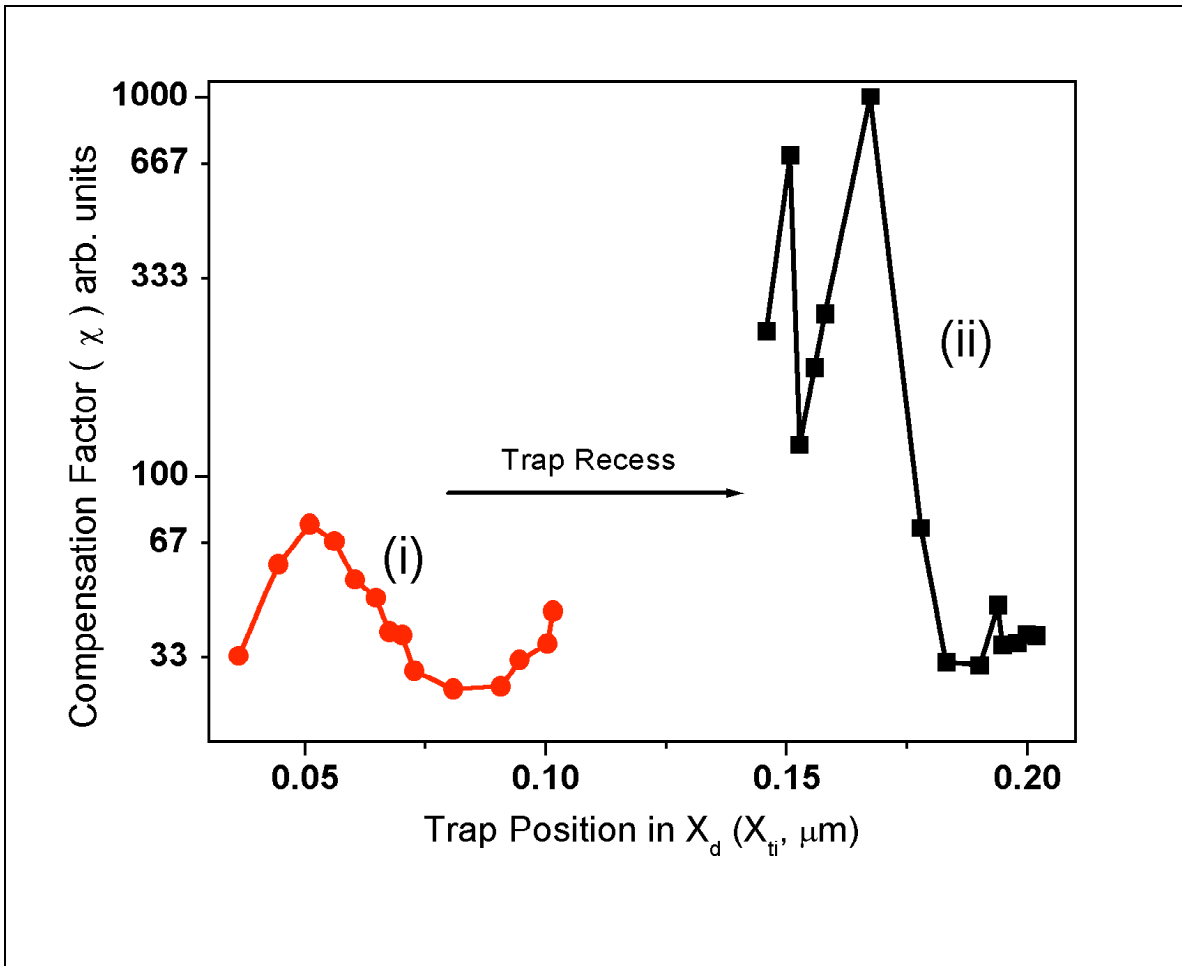


Figure 3: Triangular profile of Donor traps distributed by X_{ii} , with X_d (the depletion width). Figure 3 (i): Triangular distribution of 10^{16} cm^{-2} grade I samples and Figure 3 (ii): Triangular distribution for 10^{15} cm^{-2} grade II samples.

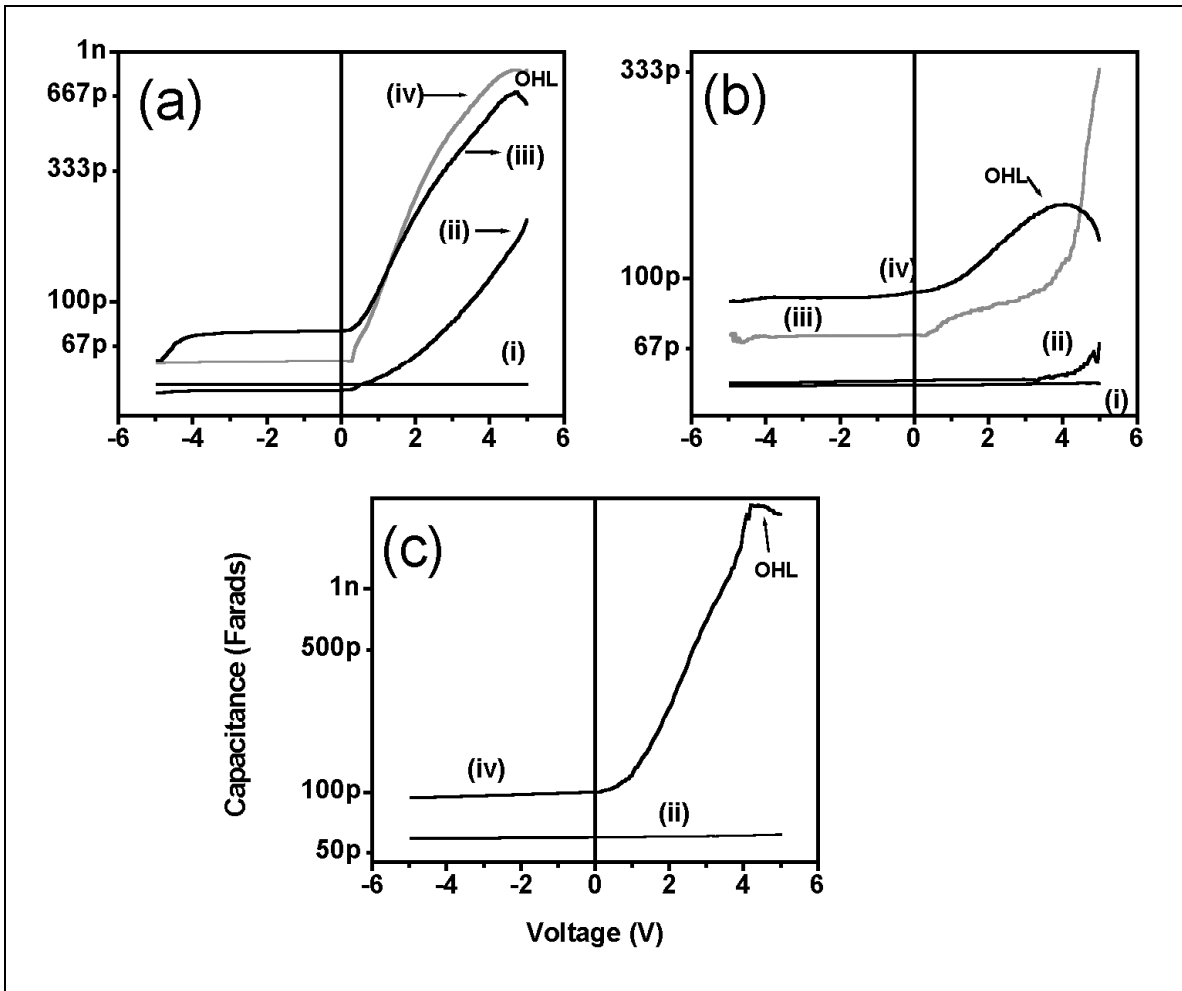


Figure 4a, 4b and 4c: CV Measurement of grade I and 10^{16} cm^{-2} , grade I and 10^{15} cm^{-2} , grade II and 10^{15} cm^{-2} Nitrogen implantation respectively. (i) As-Implanted or at 25C. (ii) Annealed at 250C. (ii) Annealed at 300C and (iv) Annealed at 350C. OHL denotes ohmic losses.

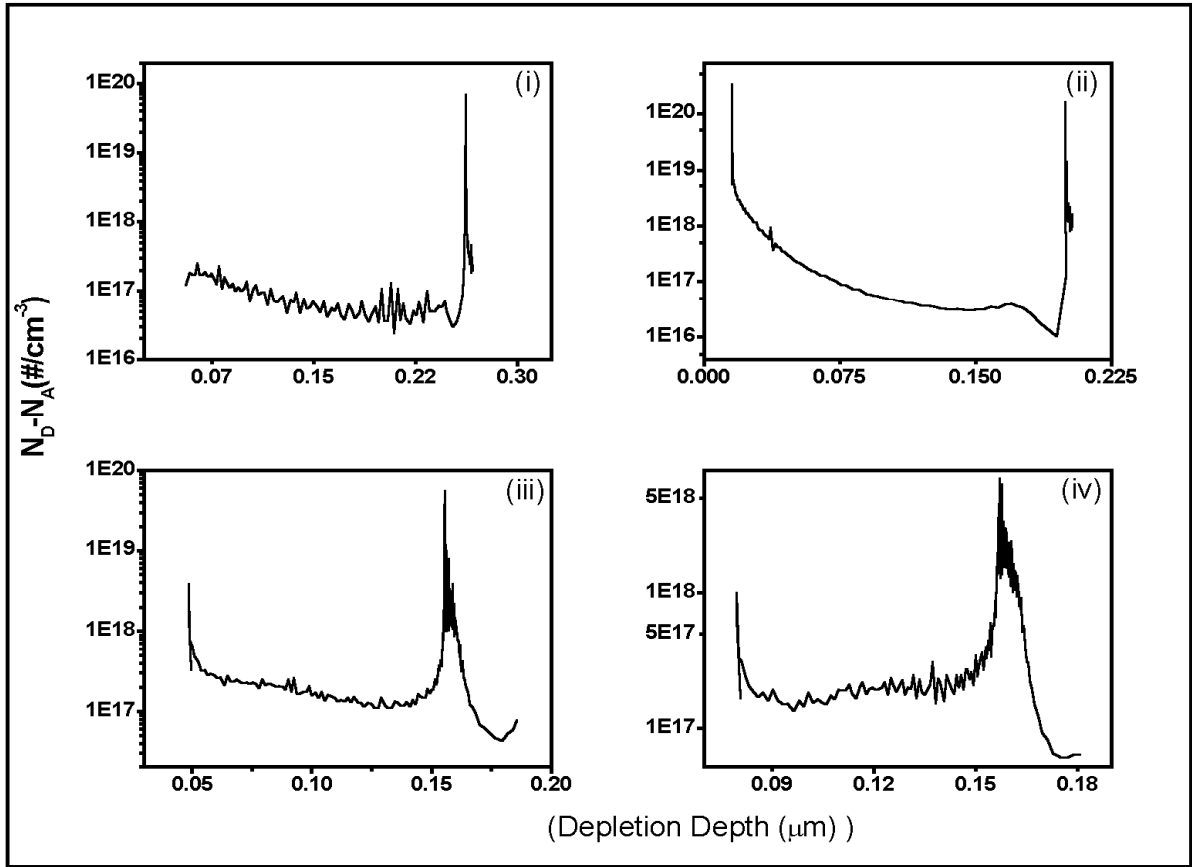


Figure 5: $N_D - N_A$ values of Nitrogen implanted Grade I samples at $10^{16}cm^{-2}$. (i) Samples annealed at 250C. (ii) Samples annealed at 300C. (iii) Samples annealed at 350C. (iv) Samples annealed at 400C.

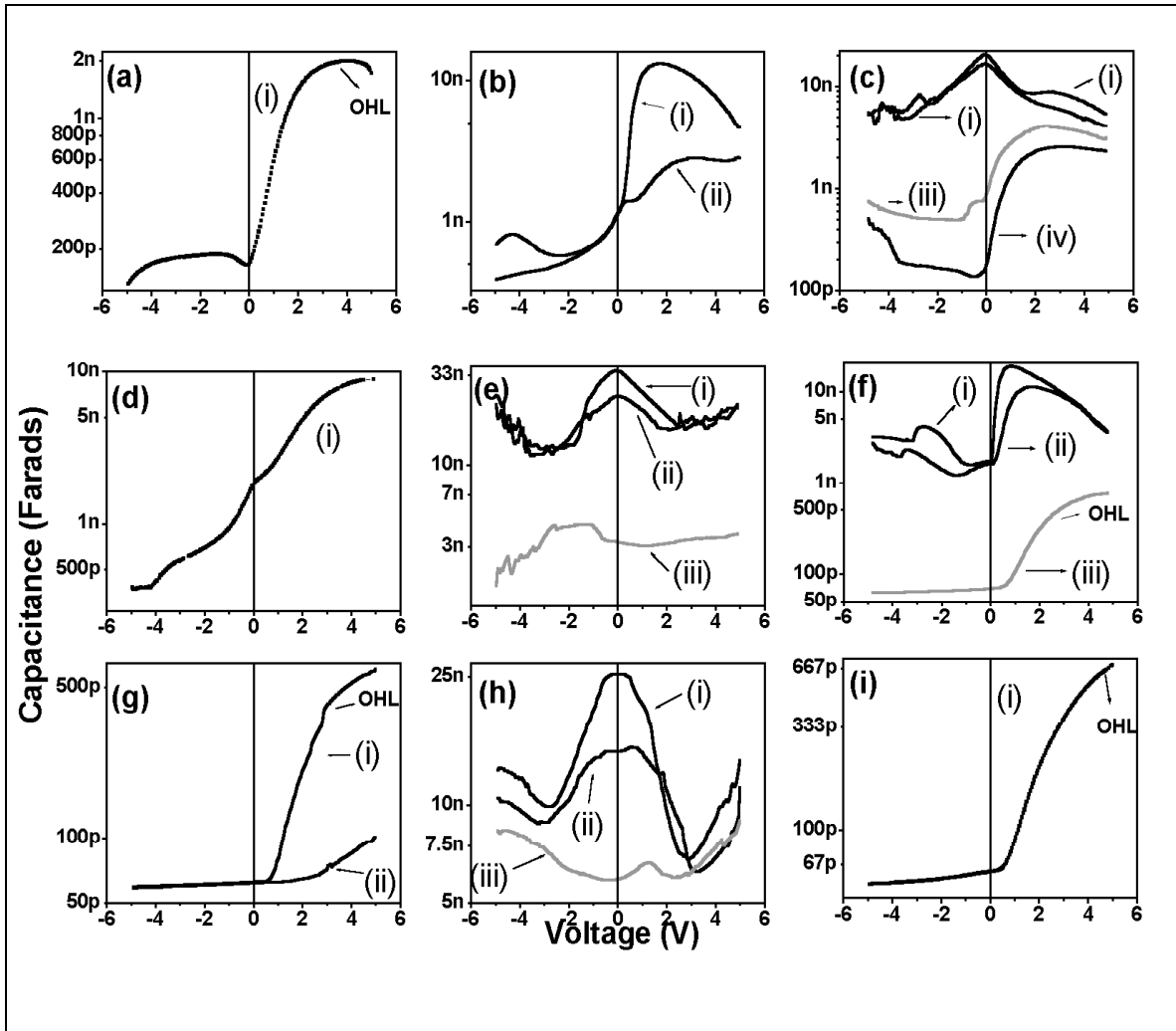


Figure 6a, 6b and 6c: CV curves for grade I samples of 10^{15}cm^{-2} , Grade II 10^{15}cm^{-2} and Grade I 10^{16}cm^{-2} nitrogen atoms annealed at 450C respectively.

Figure 6d, 6e and 6f CV curves for grade I samples of 10^{15}cm^{-2} , Grade II 10^{15}cm^{-2} and Grade I 10^{16}cm^{-2} nitrogen atoms annealed at 500C respectively.

Figure 6g, 6h and 6i CV curves for grade I samples of 10^{15}cm^{-2} , Grade II 10^{15}cm^{-2} and Grade I 10^{16}cm^{-2} nitrogen atoms annealed at 550C respectively.

Figure 6c (i) and (ii) shows local maximum due to high trap densities at 1.5 and 5.5KHz. Figure 6c (iii) and (iv) shows elimination of trap maximum and donor character of the traps at 150 and 250KHz.

Figure 6f (i) and (ii) show trap dominance at 2.5 and 4.5KHz for samples annealed at 500C Figure 6f (iii) shows return to diode character at higher frequency, 250KHz.

Figure 6h (i), (ii) and (iii) show trap dominance at 35KHz and 150KHz and 950KHz for samples annealed at 550C.

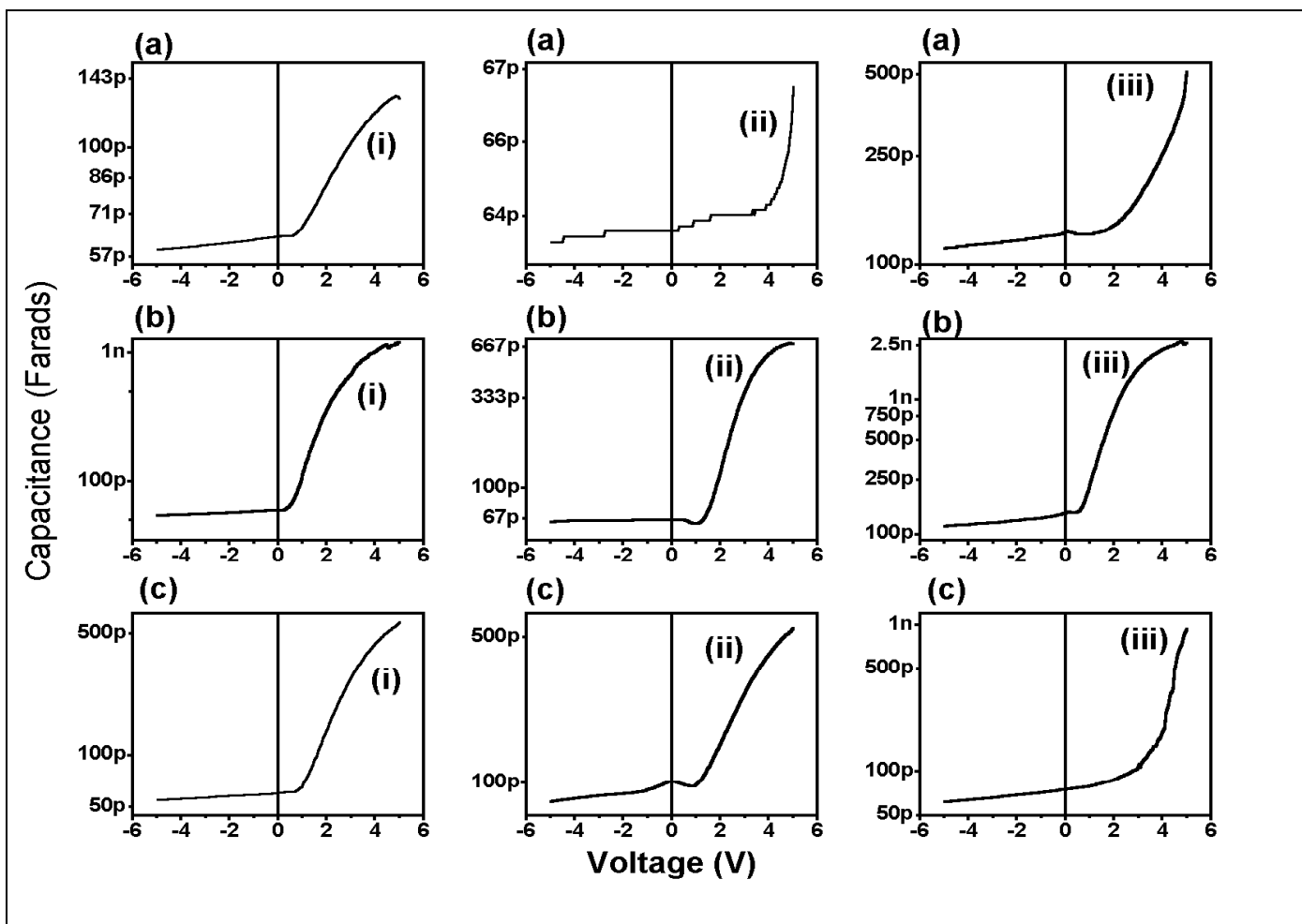


Figure 7a: Grade I substrates at 10^{15}cm^{-2} annealed at (i) 600C, (ii) 650C and (iii) 700C.
 Figure 7b: Grade II substrates at 10^{15}cm^{-2} annealed at (i) 600C, (ii) 650C and (iii) 700C.
 Figure 7c: Grade I substrates at 10^{16}cm^{-2} annealed at (i) 600C, (ii) 650C and (iii) 700C.

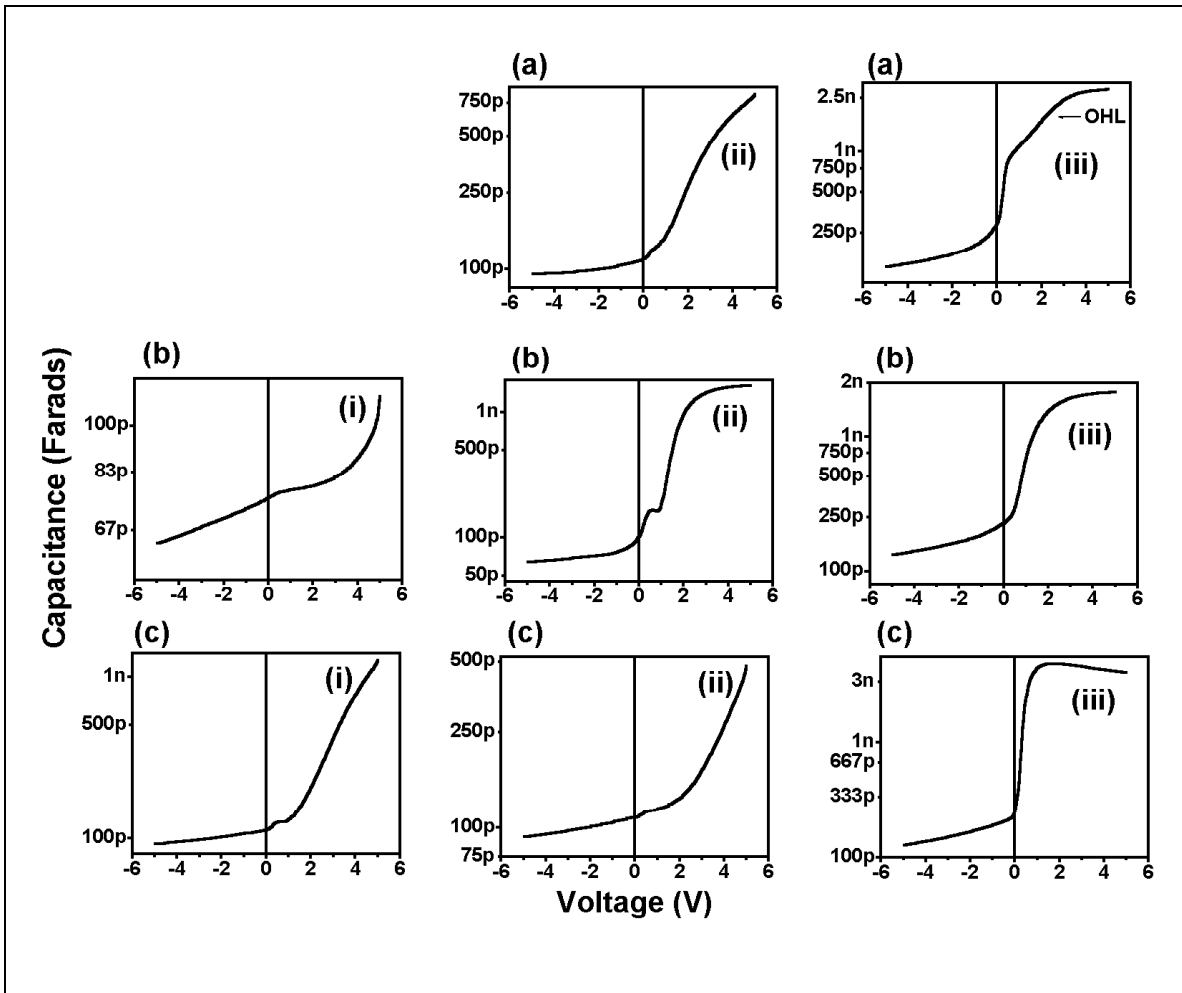


Figure 8a: Grade I substrates at 10^{15}cm^{-2} annealed at (i) 800C and (ii) 850C.

Figure 8b: Grade II substrates at 10^{15}cm^{-2} annealed at (i) 750C, (ii) 800C and (iii) 850C.

Figure 8c: Grade I substrates at 10^{16}cm^{-2} annealed at (i) 750C, (ii) 800C and (iii) 850C.

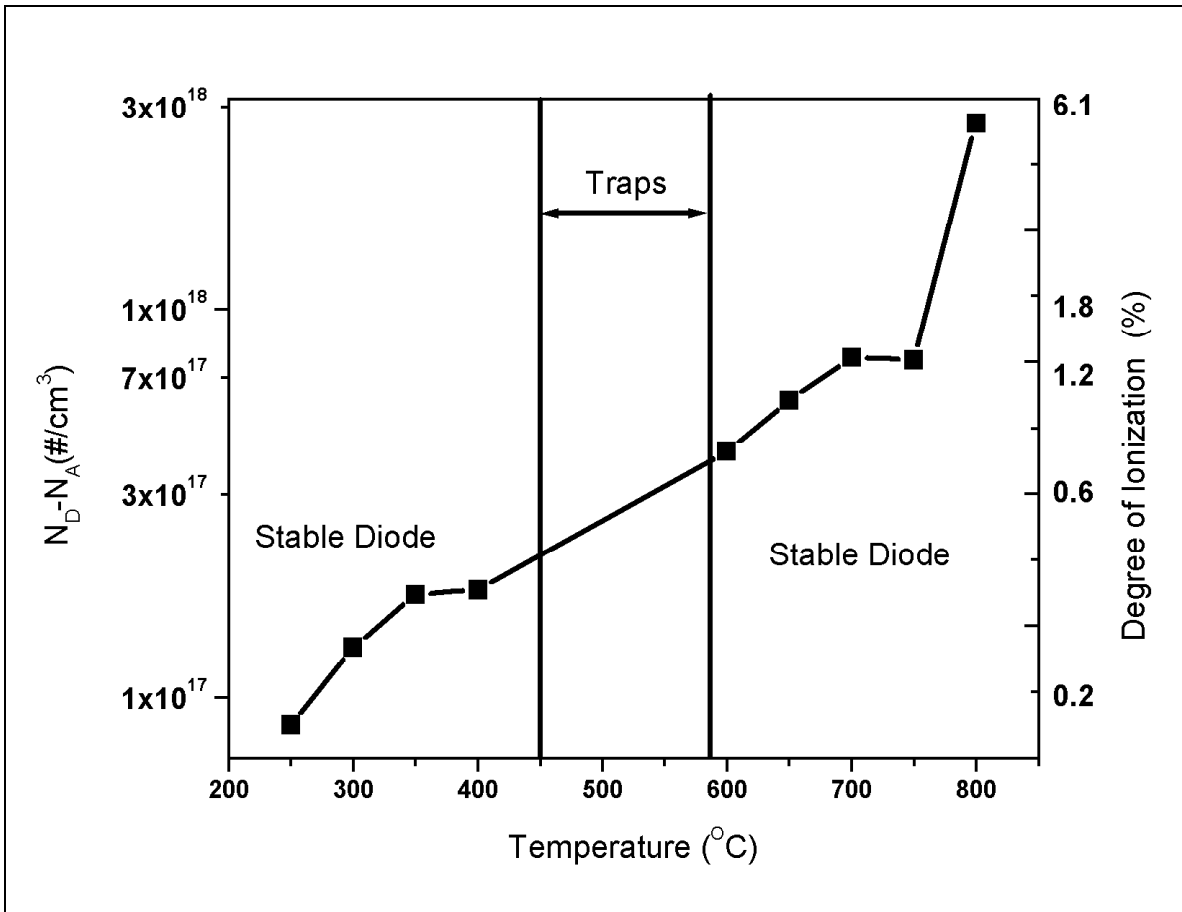


Figure 9: Degree of Ionization of Nitrogen impurities versus annealing Temperature.

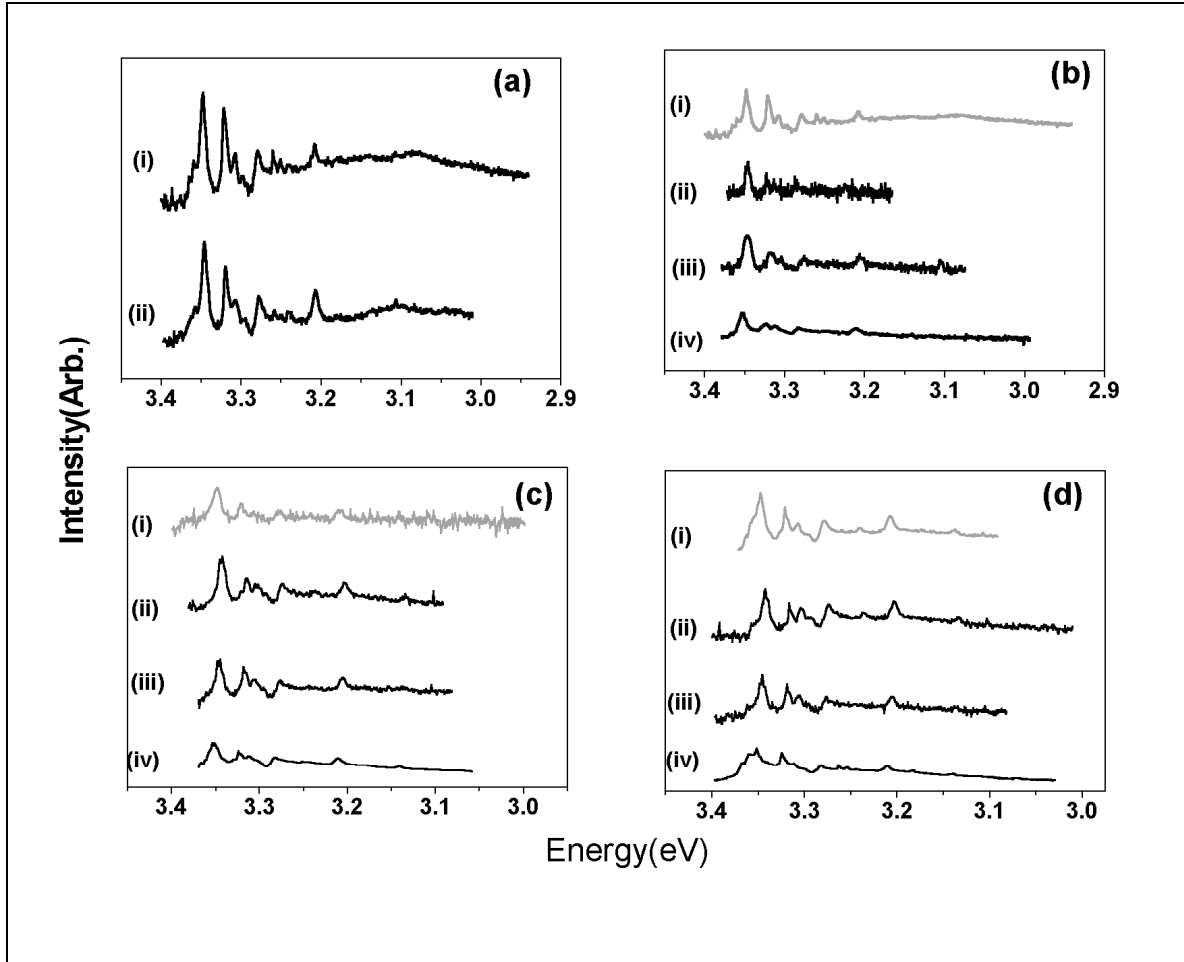


Figure 10: 8K Photoluminescence spectra of Nitrogen Implanted ZnO, Argon Implanted ZnO compared with Oxygen-Terminated virgin ZnO.

Figure 10a: Nitrogen As-Implanted Implanted ZnO:

- (i) 10^{16}cm^{-2} Nitrogen implanted O-ZnO
- (ii) 10^{15}cm^{-2} Nitrogen Implanted on Zn-ZnO

Figure 10b: Nitrogen Implanted ZnO, Argon Implanted ZnO and Virgin ZnO annealed at 250°C:

- (i) 10^{16}cm^{-2} Nitrogen implanted O-ZnO
- (ii) 10^{15}cm^{-2} Nitrogen Implanted on Zn-ZnO
- (iii) 10^{15}cm^{-2} Argon Implanted O-ZnO
- (iv) Virgin O-ZnO

Figure 10c: Nitrogen Implanted ZnO, Argon Implanted ZnO and Virgin ZnO annealed at 400°C:

- (i) 10^{16}cm^{-2} Nitrogen implanted O-ZnO
- (ii) 10^{15}cm^{-2} Nitrogen Implanted on Zn-ZnO
- (iii) 10^{15}cm^{-2} Argon Implanted O-ZnO
- (iv) Virgin O-ZnO

Figure 10d: Nitrogen Implanted ZnO, Argon Implanted ZnO and Virgin ZnO annealed at 550°C:

- (i) 10^{16}cm^{-2} Nitrogen implanted O-ZnO
- (ii) 10^{15}cm^{-2} Nitrogen Implanted on Zn-ZnO
- (iii) 10^{15}cm^{-2} Argon Implanted O-ZnO
- (iv) Virgin O-ZnO

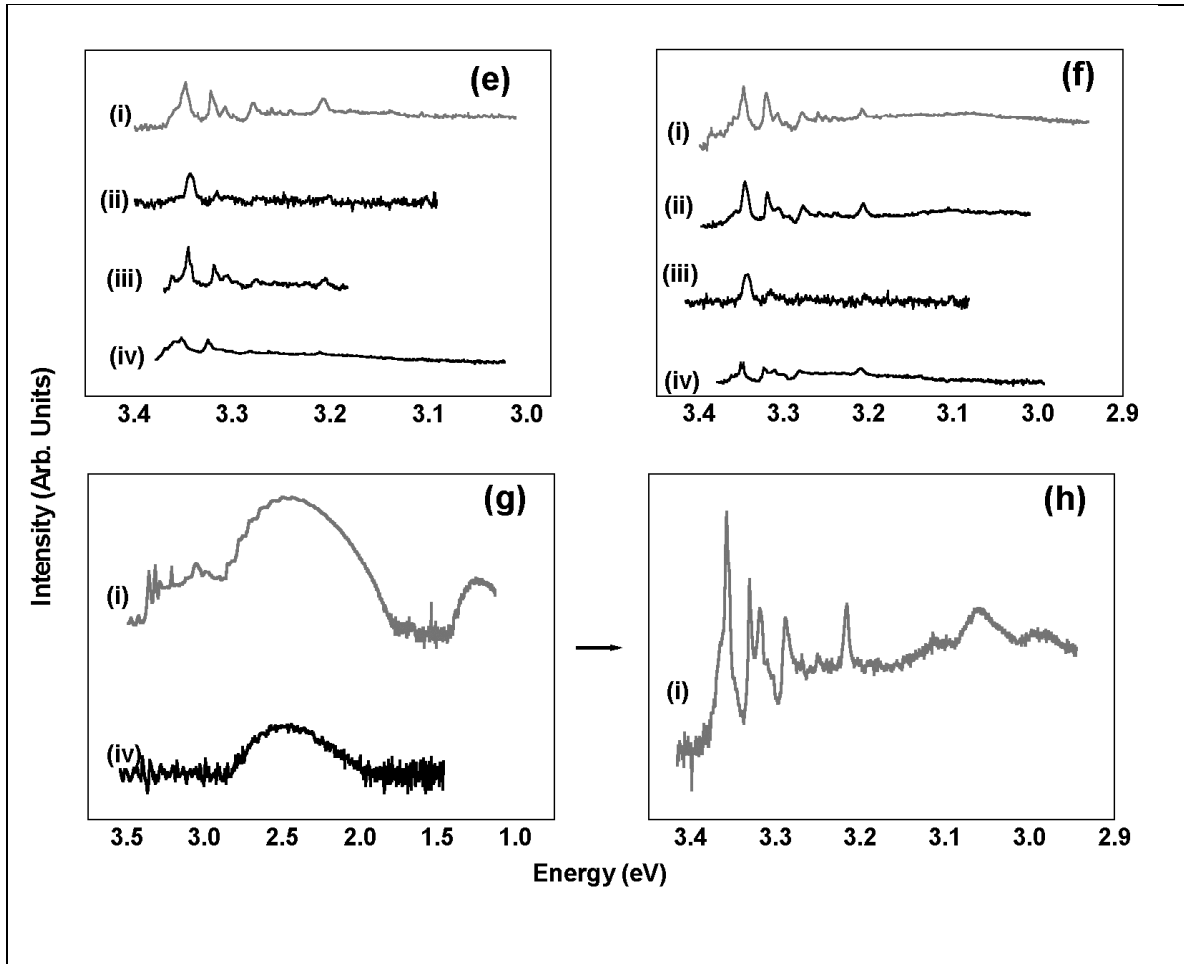


Figure 10e: Nitrogen Implanted ZnO, Argon Implanted ZnO and Virgin ZnO annealed at 700°C:

- (i) 10^{16}cm^{-2} Nitrogen implanted O-ZnO
- (ii) 10^{15}cm^{-2} Nitrogen Implanted on Zn-ZnO
- (iii) 10^{15}cm^{-2} Argon Implanted O-ZnO
- (iv) Virgin O-ZnO

Figure 10f: Nitrogen Implanted ZnO, Argon Implanted ZnO and Virgin ZnO annealed at 850°C:

- (i) 10^{16}cm^{-2} Nitrogen implanted O-ZnO
- (ii) 10^{15}cm^{-2} Nitrogen Implanted on Zn-ZnO
- (iii) 10^{15}cm^{-2} Argon Implanted O-ZnO
- (iv) Virgin O-ZnO

Figure 10g: Low Resolution PL of Nitrogen Implanted ZnO and Virgin ZnO annealed at 1000°C:

- (i) 10^{16}cm^{-2} Nitrogen implanted O-ZnO
- (iv) Virgin O-ZnO

Figure 10h: Hi Resolution PL of Nitrogen Implanted ZnO.

- (i) 10^{16}cm^{-2} Nitrogen implanted O-ZnO

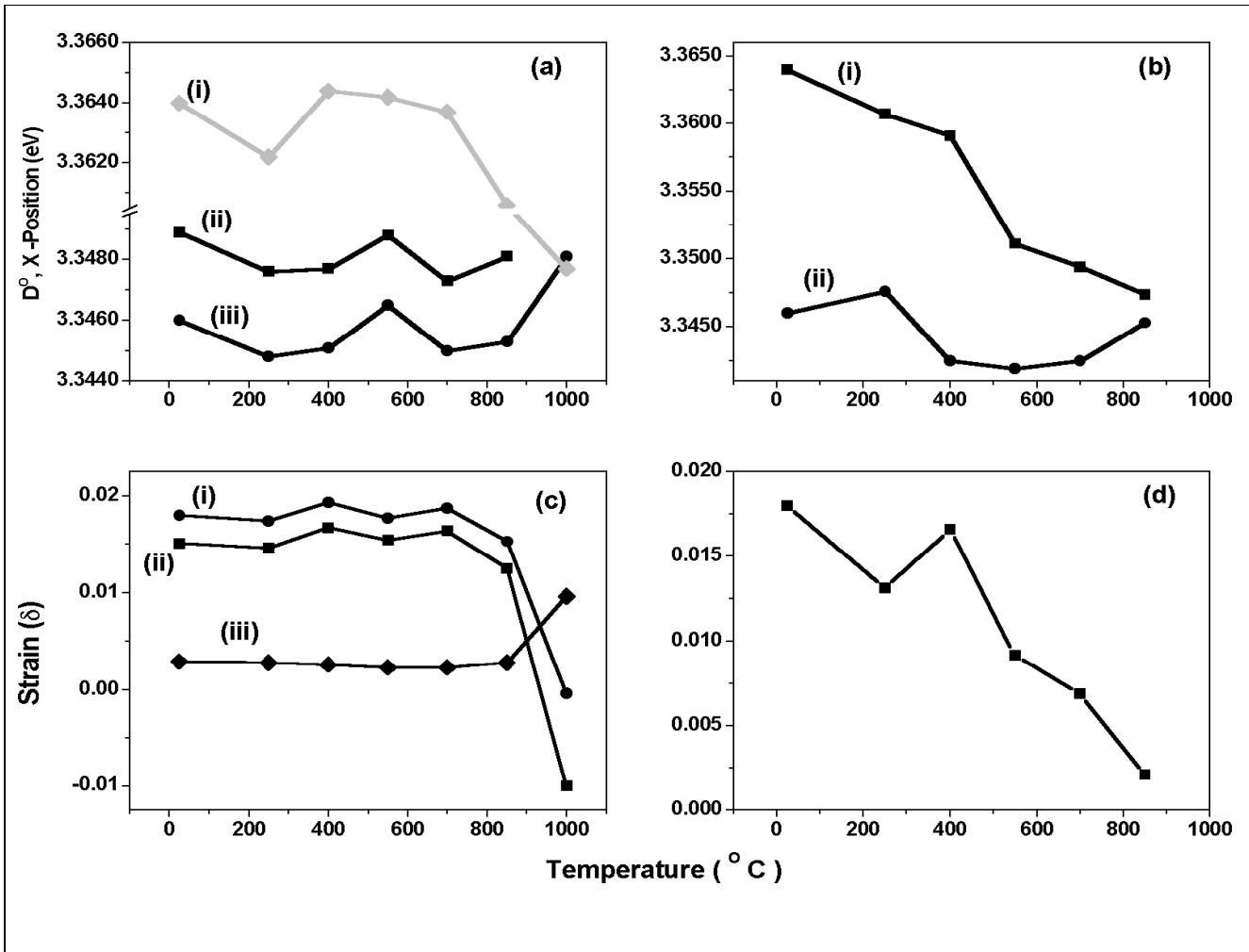


Figure 11 Shifts in Neutral Donor Line with Temperature.

Figure 11a: D⁰, X variation with annealing temperature:

- (i) Virgin O-ZnO
- (ii) Nitrogen implanted O-ZnO at 10¹⁵cm⁻²
- (iii) Argon implanted O-ZnO at 10¹⁵cm⁻².

Figure 11b: D⁰, X variation with temperature:

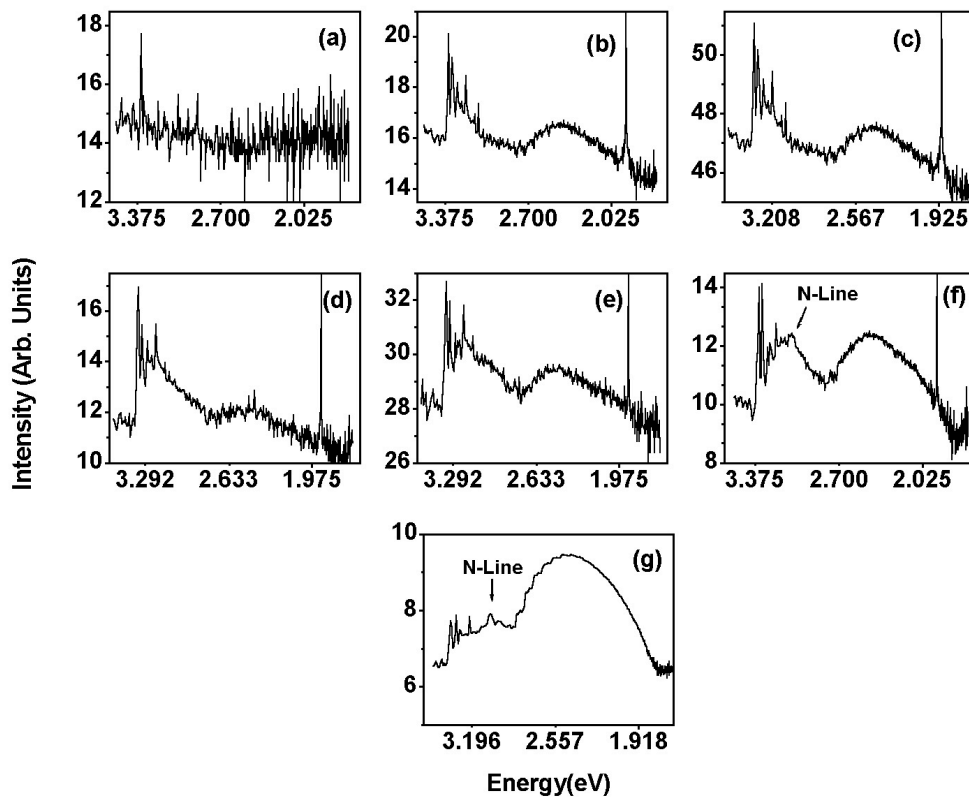
- (i) Virgin Zn-ZnO
- (ii) Nitrogen implanted Zn-ZnO at 10¹⁵cm⁻².

Figure 11c: Strain (δ) variation with temperature variation

- (i) Argon implanted O-ZnO at 10¹⁵cm⁻² relative to O-ZnO
- (ii) Nitrogen implanted O-ZnO at 10¹⁵cm⁻² relative to O-ZnO
- (iii) Nitrogen relative to Argon implantation.

Figure 11d: Strain (δ) variation with temperature for 10¹⁵cm⁻² Nitrogen Implanted Zn-ZnO relative to Zn-ZnO.

3. 9. Appendix.



Appendix I: Low Resolution 8K Photoluminescence Spectra of Nitrogen-Implanted ZnO.

Ia: Nitrogen As-Implanted ZnO.

Ib: Nitrogen Implanted and annealed at 250°C.

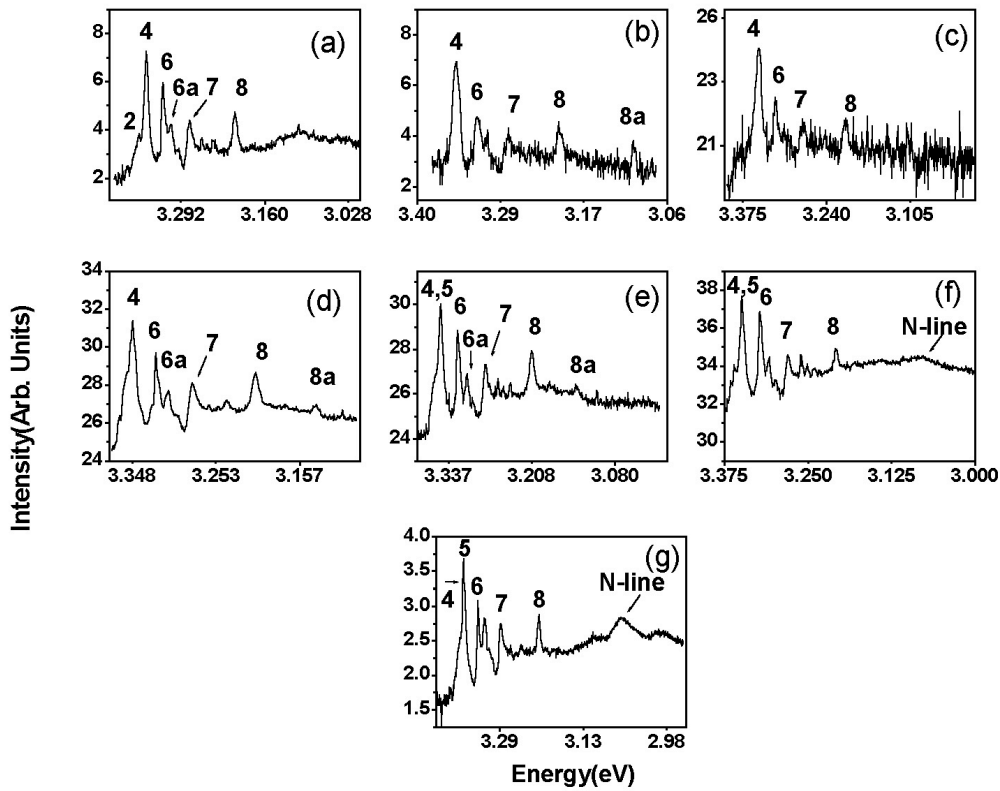
Ic: Nitrogen Implanted and annealed at 400°C.

Id: Nitrogen Implanted and annealed at 550°C.

Ie: Nitrogen Implanted and annealed at 700°C.

If: Nitrogen Implanted and annealed at 850.

Ig: Nitrogen Implanted and annealed at 1000°C.



Appendix II: High Resolution 8K Photoluminescence Spectra of Nitrogen-Implanted ZnO.

- Ia: Nitrogen As-Implanted ZnO.
- Ib: Nitrogen Implanted and annealed at 250°C.
- Ic: Nitrogen Implanted and annealed at 400°C.
- IId: Nitrogen Implanted and annealed at 550°C.
- Ie: Nitrogen Implanted and annealed at 700°C.
- IIf: Nitrogen Implanted and annealed at 850.
- IIg: Nitrogen Implanted and annealed at 1000°C.

Excitonic transitions designated as:

- 2 – Rotator \square_5
- 3 – Rotator \square_6
- 4 – Neutral Donor Bound Exciton (D^0, X)
- 5 – Neutral Acceptor Bound Exciton (A^0, X)
- 6 – Two Electron Satellite (TES)
- 6a – Longitudinal Phonon
- 7 – Free Electron to Acceptor Transition (e, A^0)
- 8 – Donor to Acceptor Transition (D^0, A^0)
- 8a – Longitudinal Phonon

4. Acceptor Conductivity in ZnO ($000\bar{1}$) Bulk Substrates via Ion-Implantation of
Metallic Impurities.

B.T Adekore, R.F Davis.

Department of Materials Science and Engineering, North Carolina State University,
Raleigh, NC 27695.

4.1 Abstract.

Notable isovalent metallic impurities as Ag^+ , Na^+ , K^+ and Li^+ were introduced into virgin $(000\bar{1})$ ZnO substrates by ion-implantation to implantations depths, R_p , ranging from 100nm-150nm. Reproducible and reliable capacitance voltage measurements indicated via diode curves, electrical activation of both silver and potassium impurities at temperatures from 350C through 850C. 8K luminescence spectra of silver implanted and annealed substrates revealed a strong suppression of green band luminescence at temperatures below 850C as well as the strong enhancement of donor bound to acceptor bound (D^0 , A^0) transitions. Particularly strong enhancement and significant broadening of the free electron (e , A^0) and the (D^0 , A^0) transitions centered at 3.2718 and 3.2025eV respectively was observed for the potassium implanted substrates at annealing temperatures above 400C. In addition, the presence of a uniquely new acceptor band centered at 2.8971eV further indicates the optical activation of potassium in ZnO. Sodium and Lithium impurities implanted into ZnO were neither electrical nor optical activated and effectively function as donors and deep acceptors respectively. Secondary ion mass spectroscopy indicated by the presence of multiple peaks, defect enhanced diffusion and segregation of metallic impurities at higher temperatures.

4. 2. Introduction.

Successful activation of nitrogen acceptors in virgin ZnO films via gas phase introduction [1-3] and substrates via ion implantation [4] has been recently observed by the referenced investigative efforts. However the successful activation of metallic impurities remains elusive to investigators of acceptor conductivity in ZnO. The traditional and reputedly purported metallic choice is Lithium. The alkali metal choice with comparable ionic radius as that of zinc cation should contribute free holes upon substitutional placement on Zinc sites. However, lithium in ZnO is amphoteric and has been postulated to function as a shallow donor upon interstitial placement (Li_i^+) and a deep acceptor on substitutional placement onto Zinc lattice sites (Li'_{Zn}). Upon proper heat treatment, the prominent character of implanted and diffused lithium in ZnO remains its ability to compensate mechanisms responsible for the highly intrinsic n-type conductivity of bulk virgin substrates as later reported in this work and observed by other groups as well [5]. In some cases, by astute thermal processing and defect engineering facilitated by the implantation of oxygen into Lithium doped hydrothermal crystals, weak hole conductivity has been observed [6]. The fact that Lithium doping usually results in insulating or compensated substrates and at best, weak hole conductivity from a deep acceptor alludes to the strong localization of free carriers via lattice coupling and relaxation.

A deep acceptor is not expected for an isovalent alkali impurity which lacks the infamous p-d repulsion. The p-d repulsion is typically responsible for abnormally deep acceptor

levels as Cu^{2+} acceptors in ZnO [7]. It is therefore inherent that there exist other factors that govern the shallow or deep ionization of metallic acceptors in ZnO besides mere isovalency. Furthermore, the weight and relevance of each governing factor orbital is determined by the presence or for that matter, absence of the d-orbital i.e. a transitional or non-transitional metallic impurity. In agreement with theoretical elucidations of other investigators [8], the governing factors for metallic acceptor ionization include the degree of ionicity of the resulting metal-oxide bond, the covalency of the metal-oxide chemical bond, the first ionization potential of the metallic impurity and the co-ordination of the resulting polyhedra. The foregoing factors individually or collectively affect lattice relaxation of the oxygen sublattice and effectively the localization of free carriers in this case, holes at the valence band edge.

4.2.1. Ionicity and Ionization Potential:

The degree of ionicity of the metal-oxide bond mathematically expressed in equation 1 is shown in figure 1 for each of the metallic impurities investigated. It is known that strong ionicity favors the localization of holes on oxygen atoms [8,9] because the 2p orbitals of the oxygen are far lower lying than the valence orbitals of the metallic atoms.

Consequently, one can expect that isovalent metallic impurities with strong ionicity (mostly the case for alkali metals) of the metal-oxide bond to be strongly coupled with the oxygen 2p orbitals. Of necessity therefore, localization of holes ensues via relaxation of the oxygen sublattice and acceptors levels are effectively deep.

$$Ionicity = \left[1 - \exp(-0.25(X_A - X_B)^2) \right] \times 100\% \quad [1]$$

X_A and X_B are the electronegativities of the metallic impurity and of oxygen respectively.

Indeed, the strong ionicity of alkali metals shown in figure I ranging from 77.97% to 82.02% for Lithium and Potassium respectively, is the very reason for the localization of holes these dopants contribute upon substitutional placement on zinc lattice sites.

However, as subsequently discussed, potassium does demonstrate sustainable diode characteristics and effectively, is an anomaly because sustainable diode characteristics would infer the presences of free holes. The anomaly can be explained if one considers the lower first ionization potential of potassium (4.341eV) compared to that of Sodium (5.139eV) and for that matter, of Lithium (5.392eV). Although potassium has the highest degree of ionicity (82.02%) of the investigated alkali metals and necessarily forms a deeper level, its lower first ionization potential allows for the ionization of such deep acceptors upon substitution on Zinc lattice sites and thus measurable acceptor or diode behavior. Sodium and Lithium in addition to their strong ionicity of 79.30% and 77.97% respectively have higher first ionization potentials. Consequently, even on substitutional placement, the deep acceptors thus formed necessarily have higher ionization barriers for the ionization of free carriers. Conclusively therefore, sodium and lithium at best form deep acceptors based on their strong ionicity and because of their higher ionization potentials such deep levels do not readily ionize. The other apparent disadvantage of

Sodium and lithium is the possibility of amphoteric ionization. Amphoteric ionization results in the occupation of interstitial as well as substitutional positions and consequently the concomitant presence of monovalent acceptor and donor levels ensues. The net effect of amphoteric ionization on the conductivity of the crystal maybe negligible because of the tendency to self-compensate as such, the innate conductivity of the crystal might be the overall observed conductivity. This is very much the case for sodium impurities as we subsequently discuss.

4. 2. 2. Chemical Modulation of Valence Band and Covalency [8]:

Low-lying anion 2p-orbitals in ZnO, are the selfsame reasons for the wide bandgap and the doping asymmetry of the crystal. More importantly, these low lying 2p orbitals have remarkable high energies and thus deep acceptor levels as far as other acceptor dopants are concerned. In fact, for anion dopants substituting on the oxygen sublattice, a necessary requirement is that the ionization potential of the impurity is at the very least, greater than that of oxygen in order to avoid free carrier (holes) localization. It has been suggested by the above reference, that if the energy levels of the uppermost closed shell in the metallic cation is equivalent to those of the 2p levels of the oxide ions, covalency is introduced into the metal-oxide bond. An immediate consequence of covalency is the formation and dominance of an extended valence band structure over the localized valence band structure intrinsic to ZnO. Silver and Copper with neutral configurations [Kr] 4d¹⁰ 5s¹ and [Ar] 3d¹⁰ 4s¹ respectively have cations Ag⁺ and Cu⁺ with closed-shell electronic configurations of 4d¹⁰5s⁰ and 3d¹⁰4s⁰ respectively. It has already been established that Copper acts as a deep acceptor in ZnO [10-12]. This deep acceptor level

could possibly be attributed to isoelectronic ionization of copper upon substitutional placement as Cu^{2+} and the slightly higher ionicity and consequently carrier localization of the copper-oxide bond (44.73%) compared to Ag-O bond (43.45%).

In any case, $d^{10}s^0$ closed-shell configuration has been suggested to have comparable energy with the 2p orbitals thus introducing covalency in the metallic-oxide bond and establishing the desired extended band structure. This extended band structure enables the lowering of acceptor levels and consequently thermally activated holes are not localized and can migrate within the lattice under the influence of an applied electric field. Silver ions are therefore established as a new favorite for metallic acceptor dopant in ZnO with the necessary minimal ionicity, the preferred isovalency and the much desired high energy orbital, $4d^{10}s^0$.

The foregoing approach of altering the valence band structure to minimize lattice relaxation and thus carrier localization has been termed chemical modulation of valence band (CMVB, [8]) and we have found to be both essential and crucial for the generation of free holes by metallic impurities.

4.2.3. Co-ordination Polyhedra [8]:

The cation-anion polyhedra formed by metallic dopants must encourage sp^3 hybridization for p-type doping to be viable. The sp^3 electronic configuration effectively reduces the antibonding nature of oxide ions and consequently reduces both the localization of the valence band edge and the localization of holes. Tetrahedrally coordinated oxide ions in which eight oxide electrons are distributed among four σ -bonds of the

coordinating cations enables sp^3 hybridization. However, tetrahedral coordination and thus sp^3 hybridization can be expected for Ag_2O and Cu_2O but not for AgO and CuO as mandated by Pauling's coordination rules. Therefore the additional constraint of sp^3 hybridization and consequently tetrahedral anion co-ordination seems necessary for delocalized holes.

Because Copper atoms unfortunately behave as deep acceptors in ZnO , the localization of holes contributed by copper ionization is quite apparent. The mechanism of copper ionization involves disproportionation reactions which may encourage the formation and dominance of divalent copper ions Cu^{2+} , and as a result isoelectronic contributions. The resulting crystal type is CuO rather than the desirable Cu_2O . Immediately, the disadvantage of the absence of sp^3 hybridization results in the undesirably localization of the valence band edge. The new favorite, silver, does not have this handicap. Ionization mechanisms of silver do not necessarily involve disproportionation due to its slightly higher second ionization potential compared to copper and more importantly, the isovalency of silver guarantees the Ag_2O structure and thus ensuring delocalization of the valence band edge by sp^3 hybridization.

The foregoing contingencies support the experimental observations we have made on the activation of metallic impurities in ZnO . In which we have observed that of the non-transitional metals investigated, potassium emerges as a new favorite. Potassium demonstrates sustainable diode behavior as characterized by CV and thus acts as an ionizable acceptor because of its lower first ionization potential. We have also observed that silver is a new transitional metal favorite acceptor because of its closed shell

configuration, $4d^{10}s^0$ which enables covalency. Again this covalency is a consequence of the energy equivalence of the 2p oxygen orbitals and the $4d^{10}s^0$ orbitals. And finally silver possesses a tetrahedral co-ordination of oxide anions which in turn, guarantees the delocalization of the valence band structure by sp^3 hybridization. CV characterization of ionized silver impurities in ZnO, also demonstrate sustainable diode characteristics.

Sustainable diode properties in the sense that low temperature and high temperature CV measurements at optimal measurement frequencies [13] with the exception of the notorious trap active temperature region [4, 13], must indicate persistent diode properties.

This restriction arises from the very fact that diode properties at low annealing temperatures do not conclusively indicate the activity of intentionally introduced acceptor impurities. The presence and properties of implantation induced defects can replicate a fictitious diode character at low annealing temperatures which can only be proven to be due to the intentional dopant if such diode character is sustained at elevated temperatures wherein firstly, the crystal has been recovered from implantation induced defects, strain or damage; and secondly, the degree of dopant ionization is quite significant.

Generally, we also observe the traditional optical transitions and their associated phonon peaks. Such peaks include the neutral donor bound excitonic transitions (D^0, X), the two electron satellite peaks (TES), the free electron to acceptor transition (e, A^0), the donor-bound to acceptor-bound transition and in some cases the higher order rotator states (\square_5, \square_6). The position of these lines is shifted for each case and rarely occur at exactly the same energy value from sample to sample and for that matter from one annealing temperature to another, however, the deviation is minimal and can be attributed to the hydrostatic strain introduces by each implant upon substitutional placement on lattice

positions. The individual optical contribution of each of the metallic impurities and the actual positions of their corresponding excitonic transitions as well as the ubiquitous green band are explored in detail in the respective sections.

Complications arise in the CV characteristics of both superior metallic dopants due to the combined contributions of defect-enhanced diffusion as well as acute ohmic losses. The defect-enhanced diffusion is particularly prominent in Ag-implanted samples where average concentrations, N_D-N_A values, as high as 10^{19} cm^{-3} and 10^{20} cm^{-3} corresponding to ionizations of 50-60% have been observed for grade II and grade I samples respectively. Ohmic losses [14,4] as observed by a somewhat less proportionate increase in measured capacitance with increasing applied bias is indicative of high injection current in the transition region. High injection currents create very significant voltage drops in regions exterior to the transition region i.e. in the neutral regions. In turn, the voltage drops effectively reduce the junction voltage, V_j , and thus lower the level of carrier injection into the junction. Effectively, the junction current and hence, the junction capacitance increases more slowly or less proportionately with increasing bias. This effect is captured by the expression below in which R_p and R_n are the respective resistances of the p and n regions and V_a and V_j are the respective applied and junction bias.

$$V_j = V_a - I[(R_p(I) + R_n(I))] \quad [2]$$

The additional convolution of increased dopant ionization at higher annealing temperatures creates a decrease in the resistances of p and n region which tend to retard continued degradation of junction voltage, V_j , thus restoring the ideal increase of junction current or capacitance with increasing bias. These effects prevalent in Ag-implanted

samples, introduces double slopes in the capacitance-voltage relationship as subsequently illustrated.

4.3. Experiment.

Metallic impurities were implanted at 7° off axis into grades I and II [4, 13] eagle picher bulk ZnO substrates at conditions specified in Table I. Subsequent isochronal annealing sequences in 1atm of Oxygen was conducted from 25C through 850C at $\Delta T=50C$ increments. Electrical properties of doped substrates were measured by capacitance-voltage techniques in parallel mode with optimized measuring frequencies between 10kHz and 100KHz. [13]. Photoluminescence was carried out at 8K and a $\Delta T = 150C$ using a 17mW He-Cd laser at 325nm from 250C to 1000C. Impurity profiles of Ag and potassium implanted samples were determined by secondary ion mass spectroscopy (SIMS) as we discuss subsequently.

Table I Implantation conditions of Acceptor Impurities in Bulk ZnO.

Dopant	Dosage($\#/cm^2$)	Energy (eV)	Range, R_p (nm)
Silver	6E14	375	90nm
Potassium	1E15	250	150
Sodium	3E14	130	150
Nitrogen [†]	1.5E15	95	150

[†] Nitrogen and Lithium co-doping discussed in Discussion section D.

4.4. Discussion.

We now examine the chemical, electrical and optical contributions of the metallic impurities enumerated above beginning with the case for silver implanted substrates.

4.4.1 Silver-Implanted ZnO substrates:

4.4.1.1. Chemical Properties:

Isotopic studies conducted by Rita and Walch [15] have indicated that silver impurities implanted into ZnO undergo substitutional placement onto the Zn sublattice. Our work on isometric and asymmetric triple-axis X-ray diffraction indicated long-range strain in order of three unit cells is present in Ag-implanted substrates [16]. Studies from the above reference also indicate that it is possible to recover the damaged crystal at elevated annealing temperatures i.e. temperatures in excess of 650C. Crystals with substitutional and thermally activated Ag-impurities with minimal implantation strain can thus be obtained at annealing temperatures above 650C. SIMS profile of the Ag- implanted substrates however confirm the prevalence of defect-enhanced diffusion of the silver impurities in the zinc sublattice via the splitting of the implantation or impurity profile upon high temperature annealing. This is very much unlike the behavior of implanted Nitrogen impurities. The implantation profiles of the nitrogen species demonstrate both elevated temperature stability of the impurity profile as well as a capacity for a relatively higher dosage [4] possibly because of the absence of highly migrant point defects in the

oxygen sublattice. The zinc sublattice however, possesses highly migrant zinc interstitials (Zn^{**}) resulting from the preferential displacement of zinc atoms over oxygen upon implantation as observed by Ohta et al [17]. It is both energetically favorable and convenient that these migrant interstitial defects and their complimentary pair, Zinc vacancies (V_{Zn}'') ionically couple with the substitutional Ag impurities and consequently enhance the migration of silver impurities at high annealing ($T > 700C$) in addition to increasing dopant ionizations.

Effectively, silver because of defect- coupling and migration becomes a fast diffuser in implanted ZnO and can migrate faster than the movement of the epitaxial re-growth interface at $T \geq 850C$. The onset of impurity segregation is clearly observed by SIMS at annealing temperatures in the vicinity of 850C as shown in the SIMS profile of Figure 2. The impurity profile is stable up to 700C where segregation was not observed although slight activity of defect-enhanced diffusion is noticeable. These thermally induced metastabilities of the silver implantation profile effect a decomposition of the implantation peak into multiple peaks of three distinct concentrations at $T \geq 850C$. The decomposition is further exacerbated at 1000C to peaks of $1.5 \times 10^{18} \text{ cm}^{-3}$ at 26nm, $5 \times 10^{19} \text{ cm}^{-3}$ at 54nm and lastly, of $1 \times 10^{19} \text{ cm}^{-3}$ at 135nm. A less likely mechanism for the formation of multiple peaks would be “push-out” effects or insolvency of Ag ions in ZnO. In which case the solubility limit of Ag in ZnO would have been exceeded at dosages of 10^{14} cm^{-2} . However, because we know that ion implantation enhances the concentration of point defects in ZnO [13] and that particularly on the Zn sublattice [17], and because silver has a natural affinity for oxygen as reflected by the thermodynamic

stability of its oxides (Ag_2O and AgO), the defect enhanced diffusion and redistribution of Ag impurities seems a more tenable argument for the foregoing observations.

4.4.1.2. Electrical Properties:

The CV characteristics of Ag-ZnO annealed from 25C to 850C is heavily accented with ohmic losses (OHL), defect enhanced diffusion (DED) and breakdown effects (BDE). The effects are indicated in figure 3 where applicable. The breakdown effects occur via double depletion of the diode indicating the significant activity of interfacial boundary donor defects which contributes to electrical breakdown as we have discussed in reference [13]. Although the onset of redistribution and segregation of Ag impurities was only observed at temperatures in the vicinity of 850C, N_D-N_A profiles indicated that impurity redistribution commenced at a much lower annealing temperature of 400C. Generally, limited redistribution of Ag impurities commences at temperatures around 400C. Allowing for the depletion approximation, the designated depths of X_1 , X_2 and X_3 in figure 4b approximately corresponds, although not exactly, to the three segregated peaks observed in the SIMS profile. The non-linearities seen around $V_a=0$ in CV curves can thus be correlated to the dopant segregation or defect enhanced diffusion occurring at the respective annealing temperatures. Each thin segregated region: X_1 , X_2 and X_3 would contribute an intermediate turn-on of the diode upon forward bias and therefore a non-linearity around $V_a=0$ upon forward bias. Unlike nitrogen impurities, the diode character

of Ag implanted substrates is sustained even at 850C although accented by the effects of higher degrees of ionization (50%-60%) and defect-enhanced diffusion as seen by the double slopes of figure 3n. Strong ohmic losses coupled with the activity of Schottky defects facilitates the reversion of diode characteristics to the intrinsic donor conductivity as observed at annealing temperatures in the vicinity of 1000C shown in figure 3o. The low annealing temperature regions of 250C to 400C do indicate diode behavior as well. Because the diode behavior is sustainable at high temperatures, one can infer the contributions of substitutional silver impurities however at lower degrees of ionization at these low annealing temperatures especially at 400C (figure 3e). Higher temperatures of 500C, 700 through 800C (Figure 3g, k, l, m) show minimal extrinsic complications of DED and BDE and thus the properties of a sustainable and stable diode.

Derived N_D-N_A values at selected annealing temperatures is shown in Figure 4 with the highest average N_D-N_A value of $2 \times 10^{19} \text{cm}^{-3}$ (figure 4d) or degree of ionization as high as 50% and 60% observed at 700C for grade II and grade I substrates respectively. An immediate inference from the preceding values is that ionization percentages and consequently ionization efficiency is higher on the zinc sublattice than on the oxygen sublattice where the highest percentage ionization of nitrogen impurities was only approximately 10% [4].

The notorious trap active temperature region [4,13] in which there is the strong dependence of measured capacitance on measuring frequency is again observed particularly at 550C through 650C. In this case, the effects of double depletion is very prominent and in fact, maximal at these annealing temperatures (Figure 3h-3j). Again, the diode behavior is regained as the annealing temperature drives the material out of the trap

active region to regions of temperature induced relative stability (defect annihilation [13]) and higher degree of dopant ionization as we see in figure 3k-3m. CV characterization of this stable region shows a decrease in the extent of double depletion and thus the activity of boundary donor defects as well as a relative stabilization of the diode.

4.4.1.3. Optical Properties:

Heavy atomic mass impurities as silver significantly damage ZnO bulk crystals. 8K luminescence of as-implanted Ag-ZnO is essentially quenched. The implanted crystals have a characteristic brownish-yellow taint corresponding to implantation-induced point defects forming very deep levels. This taint is progressively eliminated as the annealing temperature is increased from 250C to 1000C at a ΔT of 150C. Complete disappearance of this taint is first observed at 700C.

The first immediately noticeable trend attributable to the dopant impurity is the strong suppression of green band luminescence (GBL). The GBL suppression occurs until 850C in Ag-implanted samples after which it is strongly reactivated. This is consistent with GBL evolution observed in Nitrogen implanted samples [4] where GBL reactivation occurs above 550C. In attempting to understand the origin of the green band, it is important to consider some of its pertinent structure. We have observed sub-structure of the green band at annealing temperatures above 850C in both virgin and implanted ZnO samples. The sub-structure has been attributed to the vibronic transitions of shallow donors to deep Cu^{2+} acceptors (D-A_{Cu}) [12]. However, because of the ability to suppress

and reactivate the green band, it seems reasonable that the contributions of native defects of donor and acceptor nature are quite pertinent. Substrates treated at elevated annealing temperatures in excess of 850C do return to the innate donor conductivity of the crystals. More or less coincidental, the GBL is reactivated at temperatures in the vicinity of 850C or more. It is thus reasonable to associate the elevated annealing temperature reactivation of innate donor conductivity with the thermal reactivation of the GBL. Thus, the same mechanism responsible for the “reactivation” of the donor conductivity is also responsible for the “reactivation” of the GBL. In which case this mechanism is attributed to the thermally intensified generation of Schottky defects as oxygen and zinc vacancies ($V_O^{\bullet\bullet}$ and V_{Zn}'') occurring at temperatures wherein Schottky defects formation is both energetically feasible and sustainable. Limited extrinsic acceptors (Ag_{Zn}') ineffectively compensate overwhelming donor defects ($Zn_i^{\bullet\bullet} + V_O^{\bullet\bullet} + Ag_i'$) at the temperatures in question ($T > 850C$). Effectively, the conductivity of the system reverts to its innate donor conductivity and similarly, vibronic transitions mediated by these donor defects “reactivate” the GBL.

Although, it is difficult to preclude the possible contributions of substitutional Cu^{2+} deep acceptors to GBL in virgin substrates, it seems native defect contributions maybe the prevalent mechanism at elevated temperatures ($T > 850C$). The GBL transition (D- A_{GB}) would then involve notable transitions from donors ($Zn_i^{\bullet\bullet} + V_O^{\bullet\bullet} + Ag_i'$) to deep acceptor defects (V_{Zn}'') and consequently subject to defect thermodynamics occurring at different temperatures. Thus, at temperatures wherein the ionization of extrinsic acceptors and the annihilation of donor defects are thermodynamically favored, GBL would be suppressed as the case is for temperatures between 250C and 850C. Likewise, at temperatures

wherein Schottky defect generation is thermodynamically favored and sustained, GBL would be enhanced and such is the case at temperature above 850C. Figure 5 shows the low-resolution 8K spectra of Ag-implanted and annealed ZnO and essentially captures the suppression and reactivation of the GBL. The GBL at 1000C fits remarkably well with the vibronic model postulated by Reynolds et al [12] for almost all the implanted samples. Figure 6 shows the high-resolution spectra of the GBL for some implanted samples. Similarities in the GBL of various metallic impurities as well as those of non-metallic impurities (not shown) also reinforce the assertion on the intrinsic nature of the GBL (Schottky defects) rather than an extrinsic one. The observed doublet splitting in figure 6 is explained by the presence of two donors E_{D1} and E_{D2} with activation energies of 30meV and 60meV respectively and discussed in detail in reference [12].

High resolution 8K photoluminescence conducted on annealed samples from 250C through 1000C does reveal luminescence properties similar to those of nitrogen acceptors in ZnO. The enhancement of the Donor-bound to Acceptor-bound transition at (D^0, A^0) particularly at 850C and the suppression of the free electron to acceptor transition (e, A^0) are among such consistent properties and are shown in figure 7. More importantly, the appearance of a uniquely new band at 3.0318eV selectively at 850C establishes the similarities between nitrogen and silver acceptors. This broad band located at 3.0584eV for nitrogen acceptors was particularly pronounced above 850C for nitrogen-doped substrates. Besides free exciton transitions and their corresponding rotator states, all other traditional excitonic transition such as neutral donor and neutral acceptor bound transitions, the two electron satellite transition and their corresponding LO phonons were observed for the silver doped.

4.4.2. Potassium-Implanted ZnO Substrates.

Potassium is an isovalent alkali metal which demonstrates sustainable diode properties upon thermal activation as characterized by capacitance voltage techniques. The high ionicity of potassium theoretically localizes holes contributed by its ionization or substitutional placement on zinc sites and thus makes potassium a deep acceptor. However, its lower first ionization potential as previously discussed facilitates significant ionization of these deep acceptor levels resulting in measurable diode behavior by the contributions of free holes. Deep acceptor levels have been observed in the optical luminescence of potassium as subsequently discussed.

4.4.2.1. Electrical Properties:

With the exclusion of the electrically active trap region endemic to implanted ZnO as has been previously postulated [4,13], CV characteristics of K-implanted ZnO shown in figure 8, do demonstrate sustainable diode character accented with significant ohmic losses. The trap active region from 600C to 700C is strongly accented with double depletion breakdown mechanisms (figures 8i-8k) as previously mentioned for the Ag-implanted samples. The chemical analysis of K-implanted ZnO as shown in figure 16 demonstrate the stability of the potassium profile with temperature. A possible reason for this stability in comparison to the metastability of the silver profile, is the stronger ionic character of the potassium-oxide bond relative to the silver-oxide bond. This strong ionicity ensures that the interactions of potassium with the oxygen sublattice are more

stable compared with the interactions of potassium with defects within the zinc sublattice. Thus the migration of potassium is inhibited or at the very least, limited.

The double slopes in the CV profiles however, may allude to some limited defect enhanced diffusion of potassium in ZnO. The structure of CV curves in trap active regions of figure 8i to 8l indicates the dominance of donor defects as well as interfacial boundary defects effecting the observed double depletion [13]. Interestingly, new acceptor lines observed in 8K luminescence spectra completely diminish in this temperature range as well. Further thermal activation stabilizes the zinc sublattice with respect to notorious donor defects and the diode behavior is restored at temperatures from 800C (Figures 8m and 8n). As expected, the acceptor optical lines are also “reactivated” in this temperature range as we discuss in the optical section below. N_D-N_A profiles are shown in figure 9 as derived from traditional physical relationships [13]. Maximum ionization as high as 60% was observed at 500-550C for potassium impurities on the zinc sublattice. However, it seems that the degree of dopant ionization degrades with annealing temperature to lower values at 700C through 1000C. This degradation may again be attributable to the compensation by donor defects at trap active temperatures and fast diffusion of potassium at elevated annealing temperatures.

4.4.2.2. Optical Properties:

4.4.2.2.1 Traditional Lines:

Initially, the implantation damage relatively quenches the luminescence of as-implanted samples, however some luminescence is still observed. The neutral donor exciton (D^0, X) at 3.3547 ± 0.0027 eV remains within the deviation from 25C through 850C. Similar

conformity is observed for the neutral acceptor exciton (A^0, X) at 3.3522eV through the annealing temperatures. The two electron satellite transitions (TES) are again observed at the traditional position, 3.3250 ± 0.0012 eV through the annealing range as well. The corresponding phonons are observed at 72.2meV shifts from the lines in questions as well. Also observed are the free exciton (FE) transition at 3.3659eV(\square_5) and at 3.3677eV(\square_5) for samples annealed at 700C and 850C respectively. The rotator transition of the FE of \square_6 is also observed at 3.3622eV and 3.3613eV for 700C and 850C cases respectively. Figure 10 shows the high-resolution spectra of the traditional optical lines as well as their corresponding phonon replicas over the annealing temperature range.

4.4.2.2.2 Acceptor Transitions:

In determining the contributions of intentional dopants, two prerequisites seem to validate the optical activation of the introduced impurities. The first involving the presence of uniquely new transitions and the second, the enhancement of innate acceptor transitions. Indeed, activated potassium implanted substrates fulfill both prerequisites. For instance, in the luminescence spectra of samples annealed at 550C shown in figure 10&11, there is the formation of a distinct band at 2.8972eV; also there is the very strong enhancement and in some cases dominance of both the donor-bound to acceptor-bound transitions (D^0, A^0) at 3.2546eV and the neutral acceptor line (A^0, X) at 3.3522eV over other high energy transitions; finally, there is the red-shifting of the green band from its traditional center at 2.45-2.50eV to a unique center at 2.0395eV. Essentially, the neutral donor line (D^0, X) moves into the neutral acceptor line (A^0, X). Interestingly, the converse effect in which the neutral acceptor line moves into the neutral donor line was observed for metallic

donor dopants and is discussed elsewhere [18]. The fact that the highest degree of ionization of 60% was also electrically observed at the 500-550C range makes the case for acceptor related transitions, although deep acceptor transitions, with respect to the above transitions, less coincidental. The appearance of a strong free exciton transition at 3.4733eV and 3.4094eV at 700C and 850C respectively also corroborates the occurrence of strong ionization. The line at 3.4733eV at 700C maybe attributed to some degree of degeneracy in the valence band however further investigations into degeneracy is still being conducted.

4.4.2.2.3 Temperature dependence of Acceptor Transitions:

The uniquely new transitions as well as the degree of ionization do demonstrate a temperature dependence, such that different acceptor transitions are dominant at different temperatures. As examples, we track the thermally activated movement of three transitions starting with the infamous green band luminescence, GBL. The GBL is completely suppressed initially in the as-implanted case; commences formation after annealing at 250C; is “reactivated” at 400C, as well as off-centered by 0.4eV from the typical 2.45-2.5eV range to 2.0563eV; supports the formation of a new band, the K-band, or splits at 550C; returns to the typical 2.45-2.5eV position at 700C; gains intensity as well as undergoes the typical fine doublet splitting from 850C to 1000C. These transitions are shown in figure 11 and highlighted in figure 10.

Similarly, the new broad band centered at 2.8970eV, the K-band, follows similar temperature dependence. It actually commences at about 250C. It gains intensity through 400C to a maximum at 550C afterwards it disappears at 700C and thereafter, returning to

the prominent green band. Again, it appears to be less of a coincidence that the temperature of maximum intensity of the K-band also corresponds to the temperature of highest dopant ionization, 500C-550C. The thermally activated movement of the K-band is again highlighted in figures 10 and 11. Finally, the thermally activated movement of the prominent donor-bound to acceptor-bound transition (D^0, A^0), is somewhat more complicated. Primarily, the luminescence spectra of potassium implanted ZnO is essentially the same as that of virgin ZnO at temperatures below 400C. Only slight differences exist within this range involving the certain features at the onset of formation and an attenuation of the relative intensity because of implantation damage. However, at 400C and above, notable changes are established. Among such notable changes is the dominance of the DAP transition at 550C over other transition along with the coexistence of the K-band at this temperature as previously mentioned. A broadening of the DAP is also observed from FWHM of 8meV at 400C to 58meV at 550C. Even with the disappearance of the K-band at 700C, the DAP transitions is still quite enhanced at 700C however with a slight degradation of its dominance. At 850C, the DAP transition (3.2124eV) and its associated LO phonon (3.1392eV) regain dominance by a forming a strong and broad band as seen in figure 10f.

The foregoing discussion on unique acceptor lines occur because of the activation of potassium as an acceptor impurity and provide an insight into the defect mechanisms occurring due to the significant temperature dependence or metastability of these transitions. For instance, the maximal intensity of the K-band at 550C, coincides well with the maximal degree of ionization of 60% as well as the maximal concentration of

Zinc interstitials (Zn^{**}) vis-à-vis Zinc vacancies (V_{Zn}'') on the Zinc sublattice [13] and must necessarily be attributed to the highest substitution of potassium on the Zinc sublattice. Likewise, placing a greater weight on the contributions of native defects (V_{Zn}'', V_O^{**}) over substitutional copper impurities as the mechanism responsible for green band luminescence, then the thermally activated movement of the GBL can be associated with the defect reactions thermodynamically allowed at each temperature and consequently the ensuing changes in hydrostatic strain of the crystal. In essence, temperature regimes ($350C < T \leq 500C$) where defect generation on the Zinc sublattice is maximum is marked with the highest substitutional placement of dopants, highest hydrostatic strain and conversely the maximum shifts in GBL. Regimes where defect annihilation on the zinc sublattice is maximum ($500C < T \leq 700C$) also corresponds to the diminishing of ionization percentages as well as the disappearance of the K-band and degradation of the dominance of the DAP transitions. Finally, regimes wherein Schottky defect generation is sustainable ($700C < T \leq 1000C$) is marked by both a return of DAP dominance because of increased availability of zinc vacancies on the zinc sublattices as well as a “reactivation” of the GBL because of increased vibronic interaction of the deep donor-donor acceptor complexes. Above 1000C, there is the dominance of the GBL corresponding to the dominance of Schottky defect generation. The corresponding acceptor ionization energies for the DAP transition and the K-band are 224meV and 536meV respectively considering a theoretical band edge of 3.436eV.

4.4.3. Sodium-Implanted Samples:

Sodium was initially envisioned as a viable acceptor in ZnO. However, its high first ionization (5.139eV) potential in addition to its very significant ionicity (79.30%) predicates its behavior as a deep acceptor with highly localized holes. Furthermore, the possibility of amphoteric ionization i.e. interstitial and substitutional lattice placement also complicates the electronic contributions of sodium as an acceptor. In fact the electrical characteristics presented below favor the interstitial ionization of sodium as monovalent donor.

4.4.3.1. Electrical Properties:

Sodium implanted samples were annealed from 25C through 850C at 50C increments and essentially indicated similar CV profiles as virgin grade-I ZnO sample (Figure 12).

Virgin grade I substrates are typically n-type and significantly influenced by the presence of boundary donor defects as established by double depletion. This electrical behavior was also observed in sodium implanted ZnO substrates and is indicative of dominant interstitial ionization of sodium as monovalent donors. Substitutional ionization may be limited or retarded by a weak coupling of sodium impurities with zinc vacancies (V_{Zn}'') on the zinc sublattice as well as the fast diffusion of sodium via an interstitialcy mechanism. Even in the case of substitutional placement, the high first ionization potential of sodium may inhibit the formation of delocalized carriers or free holes.

N_D-N_A variation (not shown) with temperature derived from CV curves does indicate an extrinsic impurity profiles, but that of a monovalent donor. All CV curves at intermediate to high annealing temperatures remain n-type. The initial diode curve observed from 25C

to 250C is attributable to initial implantation-damage. This behavior is not sustainable at annealing temperatures in excess of 250C as the implantation damage is gradually recovered and the true contribution of the dopant impurity is determined.

4.4.3.2. Optical Properties:

The optical luminescence character of recovered Na-implanted ZnO at 8K from 25C through 1000C remains essentially similar to that of annealed virgin ZnO. The expected alleviation of implantation induced brownish yellow coloration was completed at 550C with the substrates returning to their innately transparent form. We neither observed any deep acceptor levels besides the green band at 2.45eV, nor did we observe any uniquely new lines and acceptor transitions enhancements. The typical “reactivation” of the green band at 850C and 1000C was however observed as has been observed for all other implanted impurities as well. Thus, it could be conclusively decided that sodium has negligible ionized acceptor contributions in ZnO. Figure 13 does show the optical spectra of annealed Sodium implanted ZnO from 250C through 1000C particularly the GBL reactivation mentioned above (Figure 13f and 13g).

4.4.4. Lithium and Nitrogen Codoping:

The persistent impediment to electrical measurements in ZnO has always been the unintentional and significantly high n-type conductivity, an immediate consequence of which is highly leaky electrical configuration. The advantage of lithium in ZnO is its ability to compensate this n-type conductivity. We have found firstly lithium is a fast diffuser in ZnO as shown by the SIMS data of figure 14 for diffusion depth in excess of

8 μm through constant source diffusion times and secondly, that diffused substrates are more insulating than implanted substrates as shown in figure 15 (for substrates at 1000C only) where flat line capacitance was observed from 25C through 1000C. The possibility of co-doping the compensated substrates with nitrogen acceptors might provide free acceptors in an insulating bulk and consequently magnetically observable p-type conductivity as by Hall techniques. Unfortunately we were not able to activate Nitrogen acceptors in these compensated substrates. The measured capacitance-voltage characteristics also remain insulating and flat. The characteristic diode profile for activated p-n substrates was not observed. Extensive self-compensation is a possible explanation for these observations. The electrical properties of the nitrogen-implanted-Lithium diffused substrates are also shown in figure 15.

4.5. Conclusions

It has been observed in this work, that it is indeed possible to activate metallic acceptors in ZnO. The new metallic favorites: Silver and Potassium do follow theoretical predictions of chemical valence band modulation and ionic localization respectively. Upon thermal activation, these metallic acceptors demonstrated diode characteristics as observed by capacitance-voltage techniques and optically, the strong enhancements of acceptor lines such as the donor-bound to acceptor-bound (D^0, A^0) transition, the free electron to acceptor transition (e, A^0) and even the enhancement of the two electron satellite (TES). In the case of Potassium, the presence of a new band, the K-band at 2.8970eV in the luminescence spectra at 8K and the much more apparent enhancements of the foregoing acceptor transitions as well as the presence of the high energy free

excitonic transition further corroborates the acceptor activity of the potassium in ZnO. Rather unfortunately, the ionization of Sodium in ZnO is primarily of interstitial nature and as such, sodium behaves as a monovalent donor in ZnO both electrically and optically.

4.7. ACKNOWLEDGEMENTS:

We would like to acknowledge insightful conversations of D.C Look and D.C. Reynolds especially in the work of Lithium and Nitrogen codoping. We as would as like to acknowledge D.W. Barlage for his availability as well as his insight on our electrical characterizations.

4.7. REFERENCES:

- [1]. K. Minegishi, Y. Koiwa, "Growth of p-type ZnO Films by Chemical Vapor Deposition.
- [2]. M. Joseph, H. Tabata, T. Kawai, "p-Type Electrical Conduction in ZnO Thin Films by Ga and N codoping". Jpn J. Appl Phys. Vol. 36, L1205-1207, Part 2, No 11A. Nov. 1999.
- [3]. A.B.M. Almamum Ashrafi, I. Suemune, H. Kumano and S. Tanaka, "Nitrogen-Doped p-Type ZnO Layers Prepared with H₂O Vapor-Assisted Metalorganic Molecular-Beam Epitaxy". Jpn. J. Appl. Phys. **Vol. 41** (2002) pp. L1281-1284.
- [4]. B.T. Adekore, D.W. Barlage, R.F. Davis, "Acceptor Conductivity in Bulk (000 $\bar{1}$) ZnO via Implantation of Nitrogen Ions. In Press.
- [6]. V.A. Nikitenko, A.I. Tereshchenko, V.P Kucheruk, K.E. Tarkpea, and I.P Kuz'mina, "Effect of Ion Implantation on the Optical Properties and Defects in Zinc Oxide" Translated from Izvestiya Akademi Nauk SSSR, Neorganicheskie Materialy, Vol. 25. No.10. Pp 1684-1689. October 1989.
- [8]. H. Kawazoe, H. Yanagi, K. Ueda, H. Hosono, "Transparent p-type Conducting Oxides: Designing and Fabrication of p-n Heterojunction". MRS Bulletin/August 2000 Pp28-36.

[10]. R. Kuhnert and R. Helbig, "Vibronic Structure of the Green Photoluminescence due to Copper Impurities in ZnO" *Journal of Luminescence* **Vol. 26**, pp203-206.

[11]. F.H Lieter, H.R. Alves, A. Hofstaetter, D.M. Hofmann and B.K. Meyer, "The Oxygen vacancy as the Origin of Green Emission in Undoped ZnO". *Phys. Stat. Sol.(b)* **Vol. 226**, No. 1, ppR4-R5 (2001)

[12]. D.C Reynolds, D.C Look and B. Jogai, "Fine structure on the green band in ZnO". *Journal of Appl. Phys.* Vol. 89 No 11. June 2001. Pp 6189-91.

[13]. B.T. Adekore, D.W. Barlage, R.F Davis, "Capacitance Measurements of Argon Implanted and Annealed ZnO (000 $\bar{1}$) substrates". In press.

[14]. B.G. Streetman, "Fabrication of p-n Junctions" in "*Solid State Electronic Devices*". Prentice Hall, New Jersey 1972.

[15]. E. Rita, U. Wahl, A.M.L. Lopez, J.P. Araujo, J.G. Correia, E. Alves, and J.C. Soares, "Lattice site and Stability of Ag in ZnO". In press.

[16]. B.T. Adekore, R.F Davis "Analysis of Structural Damage and Recovery in Ion-Implanted ZnO Bulk Crystals. To be published.

[17]. Y. Ohta, T. Haga, Y. Abe, "Crystallographic Features of ZnO single crystals", *Jpn J. Appl Phys* 36, L1040-L1042, Part 2, No 8H, 1997.

[18]. B.T. Adekore and R.F. Davis, "Extrinsic Donor Conductivity in ZnO via the Implantation of Metallic Impurities" In press.

4.8. Figures.

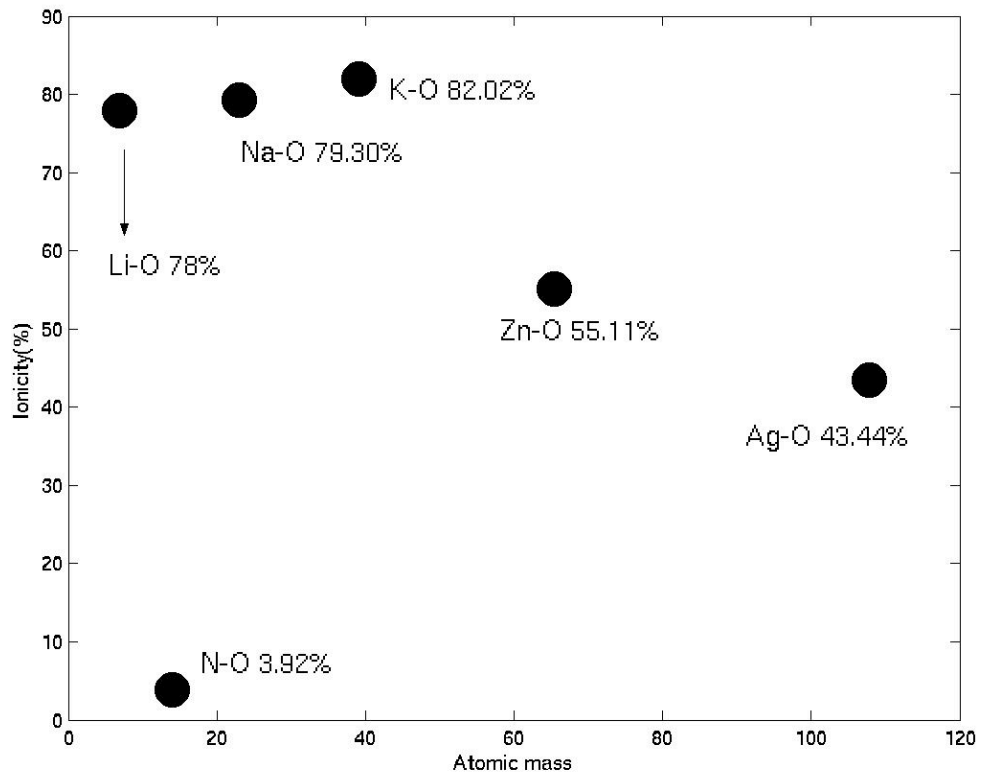


Figure 1: Ionicity of Dopant-Oxide Bond

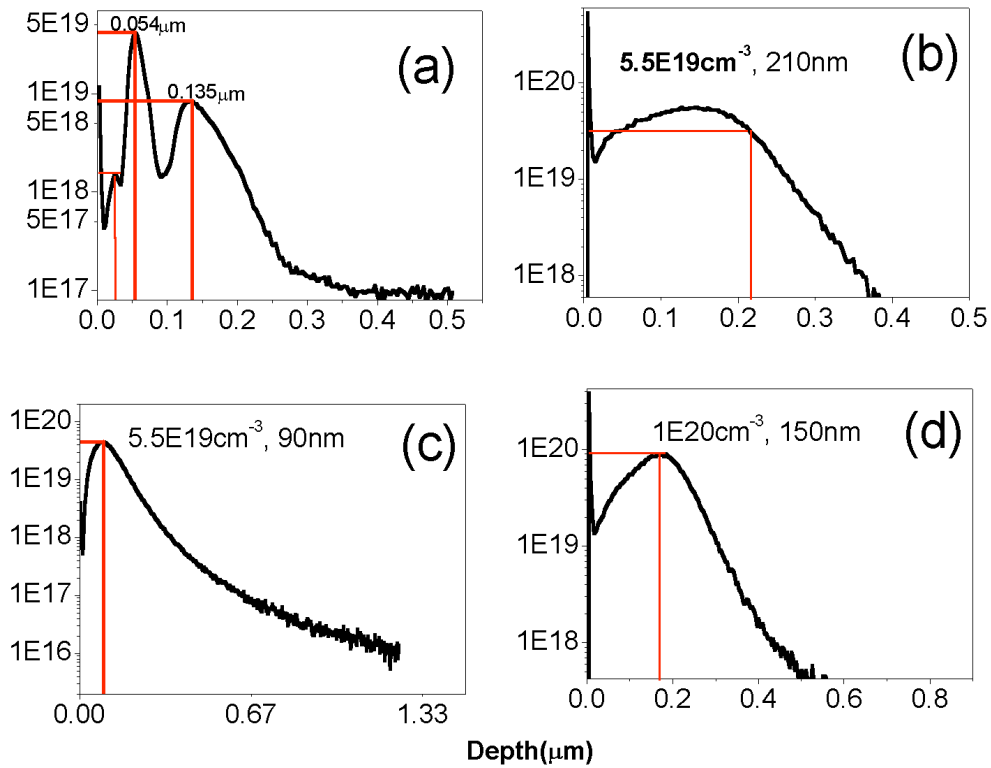


Figure 2: Comparison in SIMS Profile of Silver and Nitrogen Impurities.

Figure 2a: Ag-Implanted and Annealed at 1000°C . Figure 2b: N-Implanted and Annealed ZnO at 1000°C . Figure 2c: Ag As-Implanted ZnO. Figure 2d: N- As-Implanted ZnO.

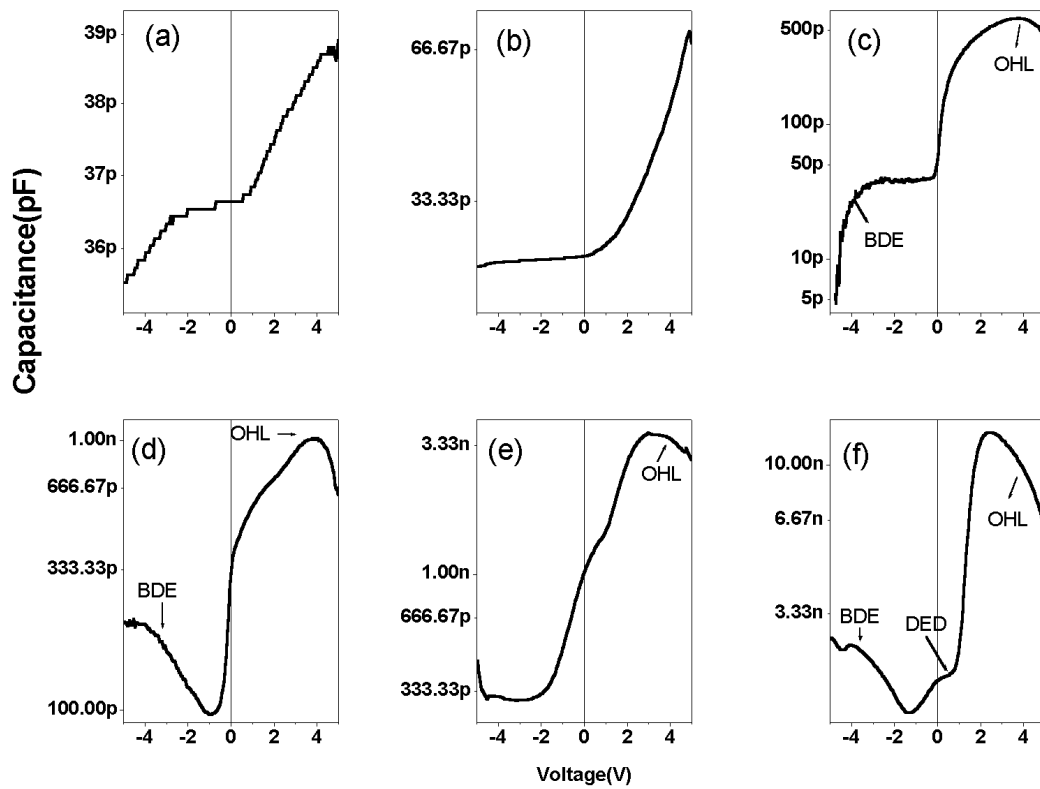


Figure 3: CV Characteristics of Silver implanted and annealed ZnO. Figures 3a for the As-Implanted, 3b at 250°C, 3c at 300°C, 3d at 350°C, 3e at 400°C and 3f at 450°C

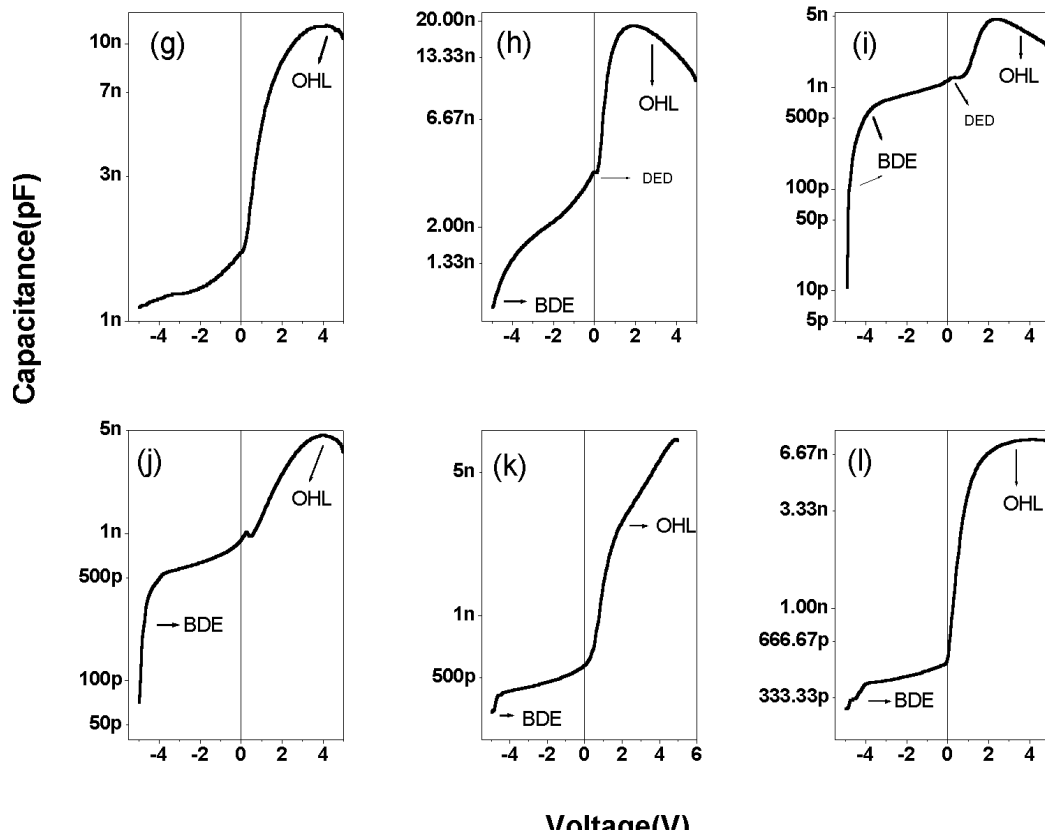


Figure 3: CV Characteristics of Silver implanted and annealed ZnO. Figures 3g at 500°C, 3h at 550°C, 3i at 600°C, 3j at 650°C, 3k at 700°C and 3l at 750°C

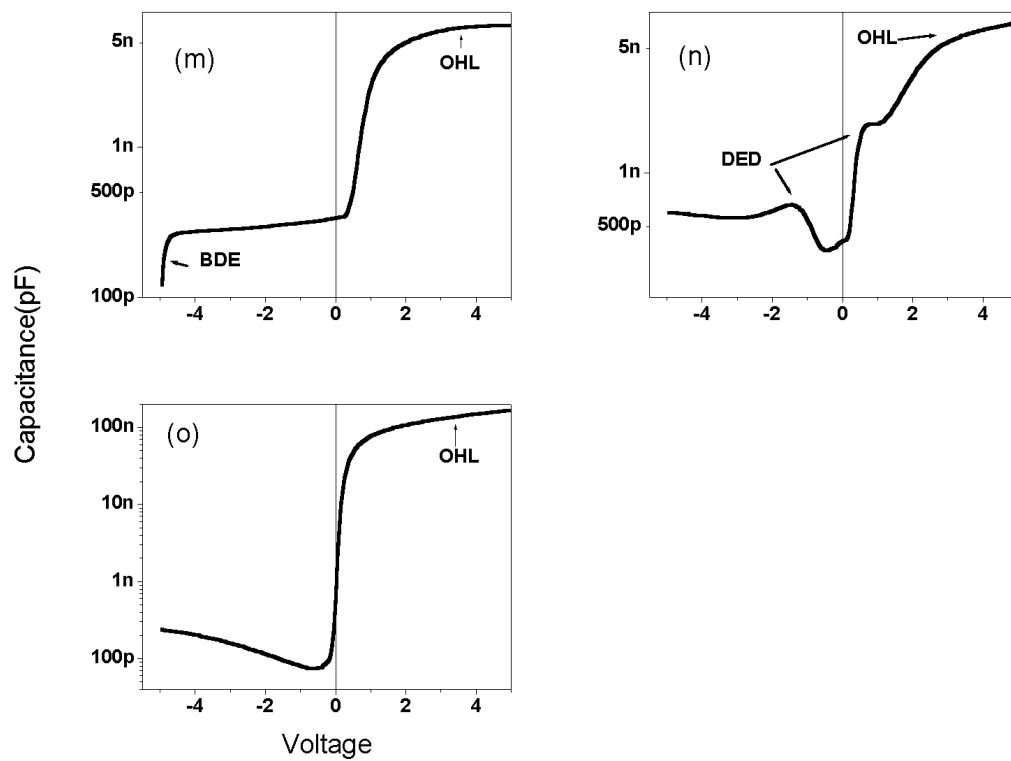


Figure 3: CV Characteristics of Silver implanted and annealed ZnO.
 Figures 3m at 800°C, 3n at 850°C, and 3o at 1000°C

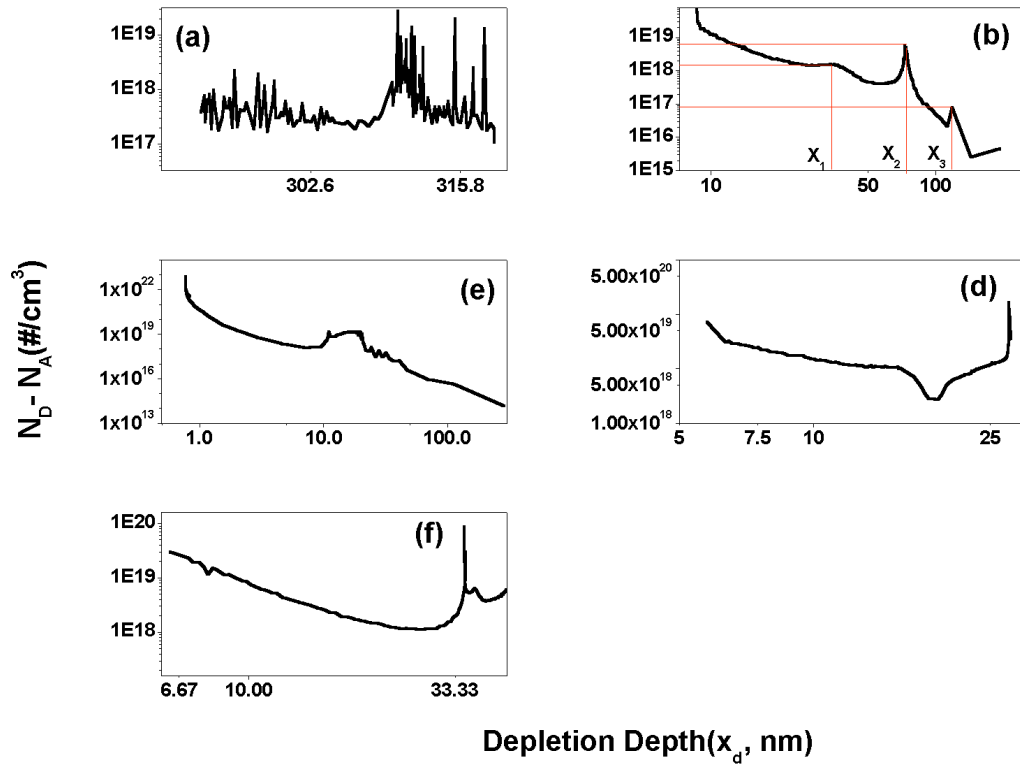


Figure 4: $N_D - N_A$ profiles of Ag Implanted ZnO. Figures (4a)- As- Implanted samples, (4b)-Samples annealed at 400°C, (4c)-Samples annealed at 650°C, (4d)-Samples annealed at 700°C and (4e)-Samples annealed 850°C.

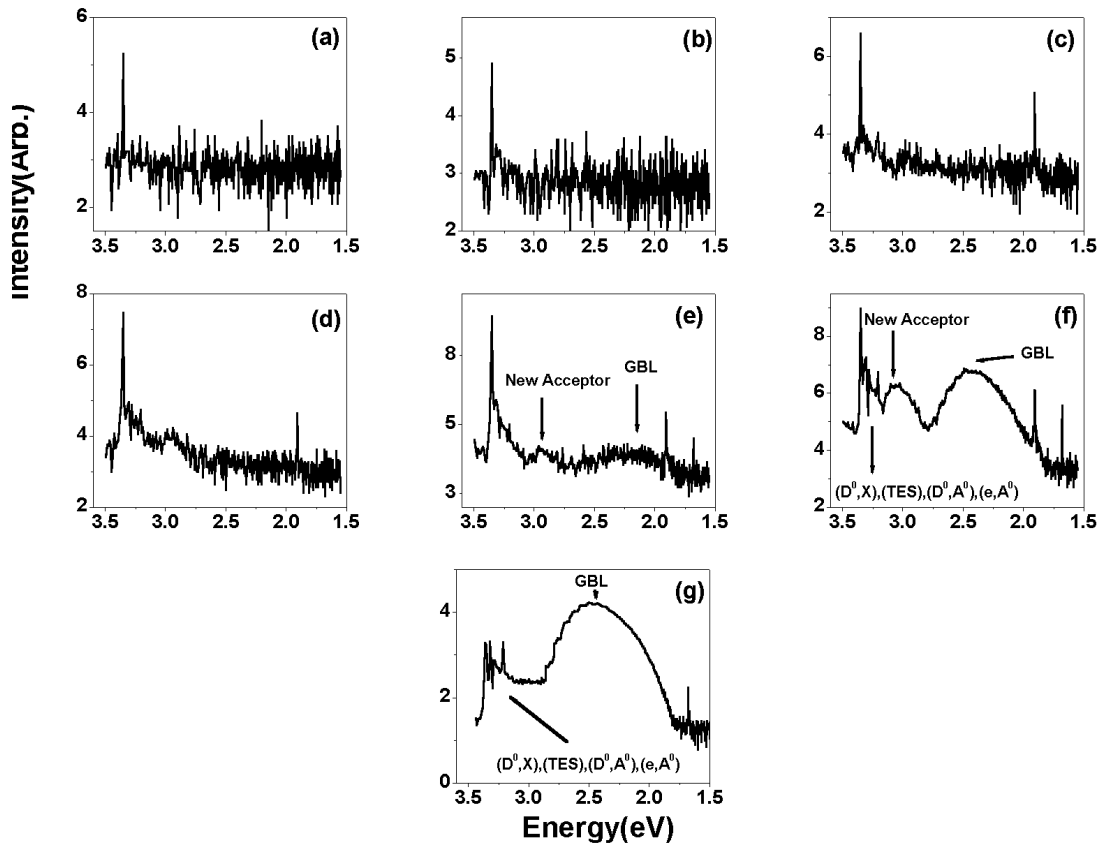


Figure 5: Low-Resolution 8K Photoluminescence Spectra of Ag-Implanted ZnO. Figures 5a shows the as-implanted samples, 5b, 5c, 5d, 5e, 5f and 5g show samples annealed at 250°C, 400°C, 550°C, 700°C, 850°C and 1000°C.

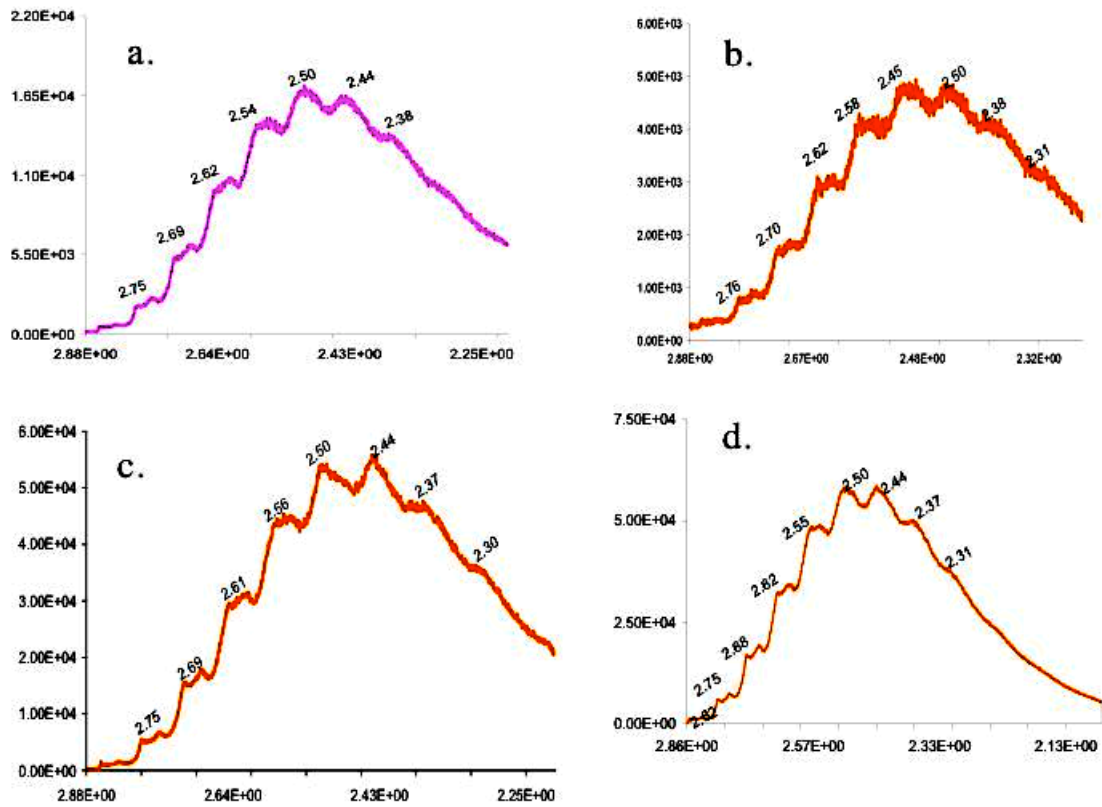


Figure 6: Reactivated Green Band Luminescence at 1000°C.
 (6a) of Ag-Implanted, (6b) of K-Implanted, (6c) of Na-Implanted and (6d) Li-Implanted.

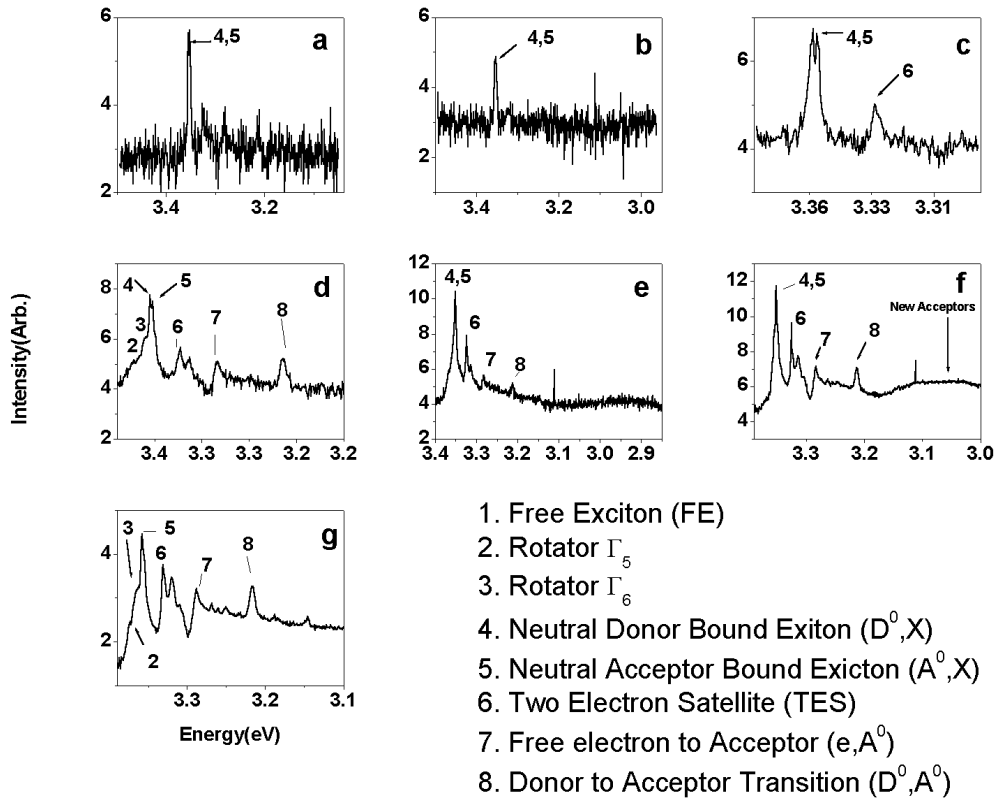


Figure 7: High Resolution 8K Photoluminescence Spectra of Ag-ZnO.

- (a) Silver As-Implanted ZnO
- (b) Silver implanted and annealed at 250°C
- (c) Silver implanted and annealed at 400°C
- (d) Silver implanted and annealed at 550°C
- (e) Silver implanted and annealed at 700°C
- (f) Silver implanted and annealed at 850°C
- (g) Silver implanted and annealed at 1000°C

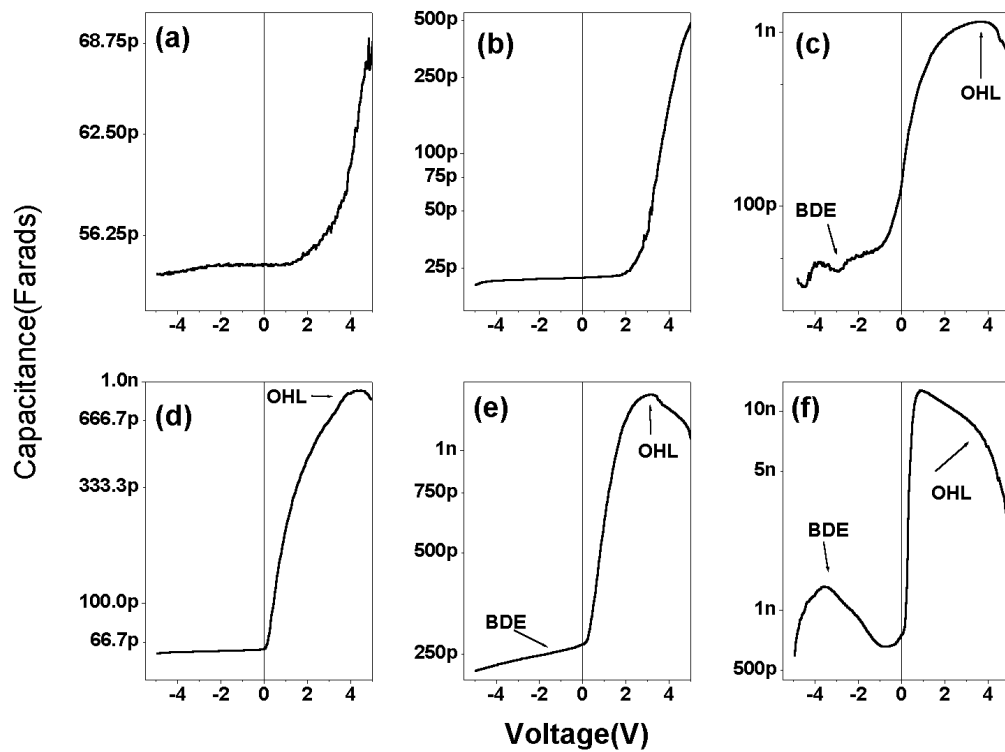


Figure 8: Capacitance-Voltage Measurements of Potassium Implanted ZnO.

- (a) Potassium As-Implanted ZnO
- (b) Potassium implanted and annealed at 250°C
- (c) Potassium implanted and annealed at 300°C
- (d) Potassium implanted and annealed at 350°C
- (e) Potassium implanted and annealed at 400°C
- (f) Potassium implanted and annealed at 450°C

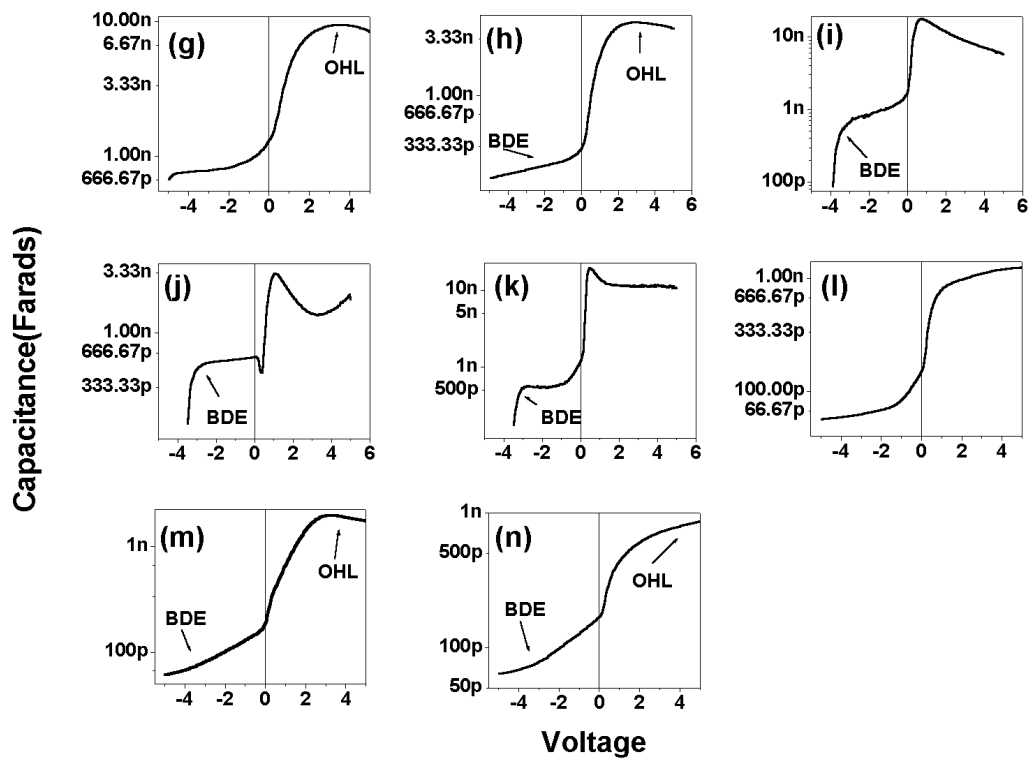


Figure 8: Capacitance-Voltage Measurements of Potassium Implanted ZnO.

- (g) Potassium implanted and annealed at 500°C
- (h) Potassium implanted and annealed at 550°C
- (i) Potassium implanted and annealed at 600°C
- (j) Potassium implanted and annealed at 650°C
- (k) Potassium implanted and annealed at 700°C
- (l) Potassium implanted and annealed at 750°C
- (m) Potassium implanted and annealed at 800°C
- (n) Potassium implanted and annealed at 850°C

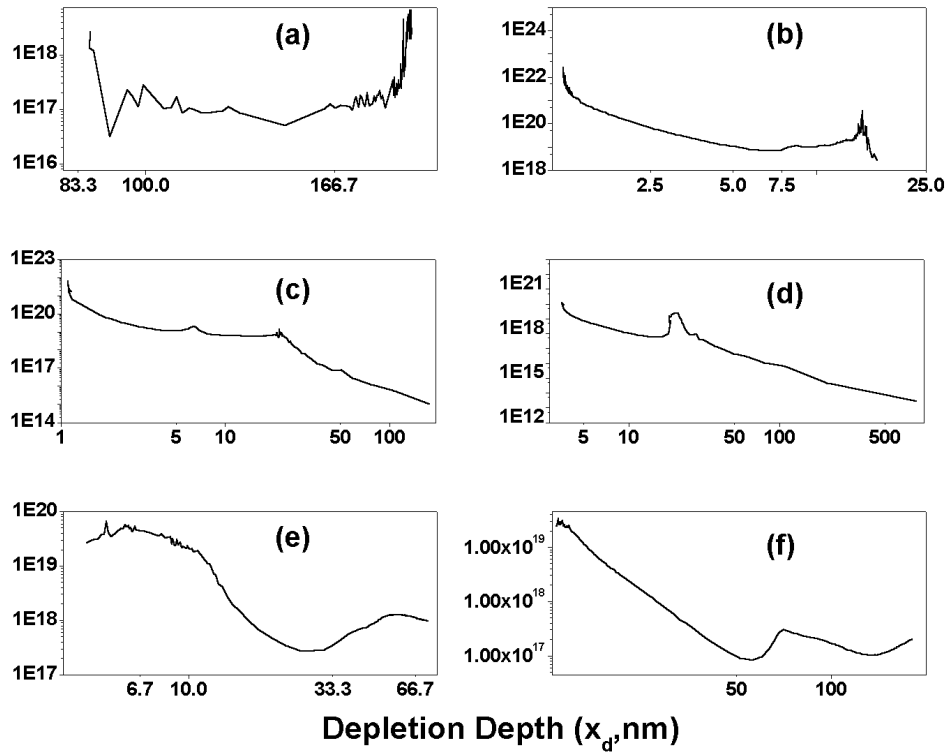


Figure 9: Carrier Concentration ($N_D - N_A$) of Potassium Implanted ZnO.
 (a) Potassium implanted and annealed at 350°C
 (b) Potassium implanted and annealed at 500°C
 (c) Potassium implanted and annealed at 550°C
 (d) Potassium implanted and annealed at 600°C
 (e) Potassium implanted and annealed at 700°C
 (f) Potassium implanted and annealed at 850°C

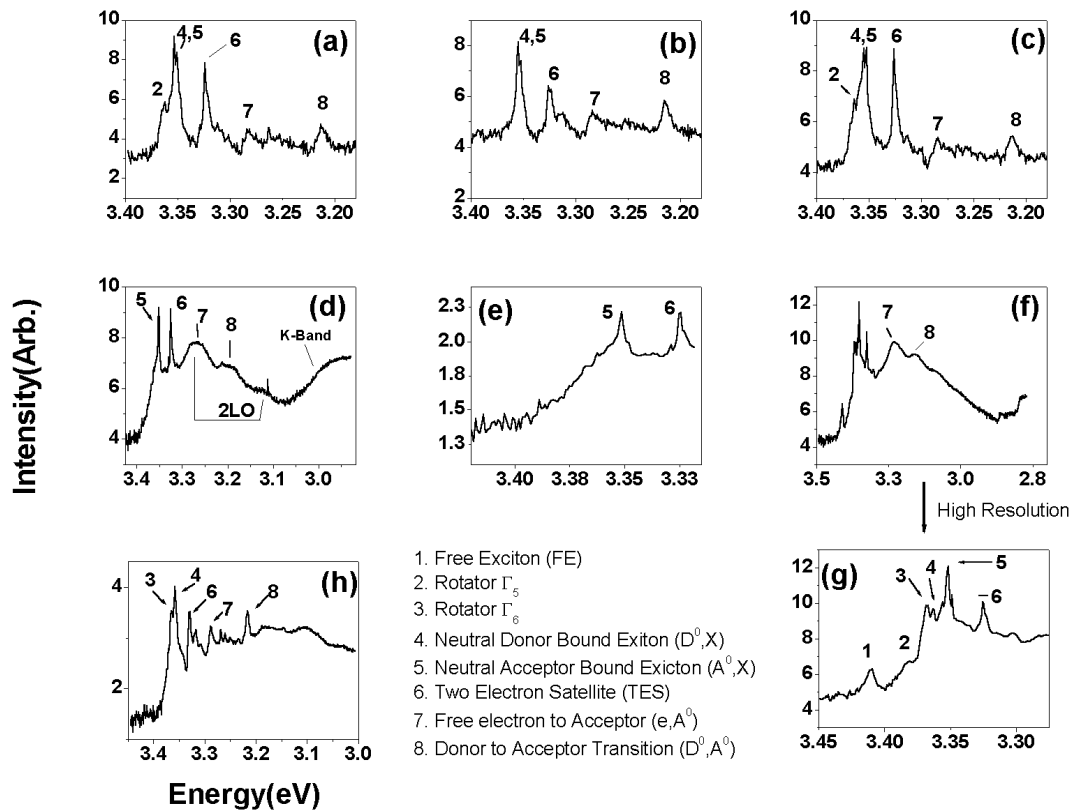


Figure 10: High Resolution 8K Photoluminescence of Potassium Implanted ZnO.

- (a) Potassium As-Implanted ZnO
- (b) Potassium implanted and annealed at 250°C
- (c) Potassium implanted and annealed at 400°C
- (d) Potassium implanted and annealed at 550°C
- (e) Potassium implanted and annealed at 700°C
- (f) Potassium implanted and annealed at 850°C
- (g) Higher Resolution spectra of implanted and annealed ZnO at 850°C
- (h) Potassium implanted and annealed at 1000°C

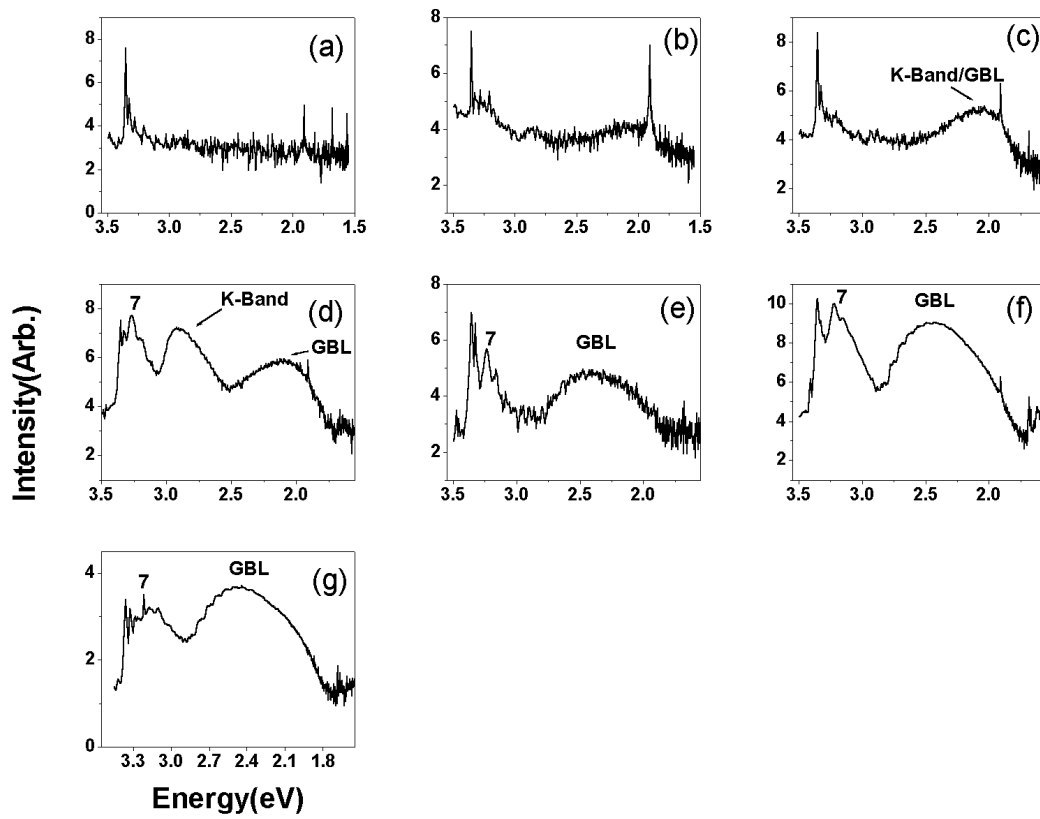


Figure 11: Low Resolution 8K Photoluminescence Spectra of Potassium Implanted ZnO.

- (a) Potassium As-Implanted ZnO
- (b) Potassium implanted and annealed at 250°C
- (c) Potassium implanted and annealed at 400°C
- (d) Potassium implanted and annealed at 550°C
- (e) Potassium implanted and annealed at 700°C
- (f) Potassium implanted and annealed at 850°C
- (g) Potassium implanted and annealed at 1000°C

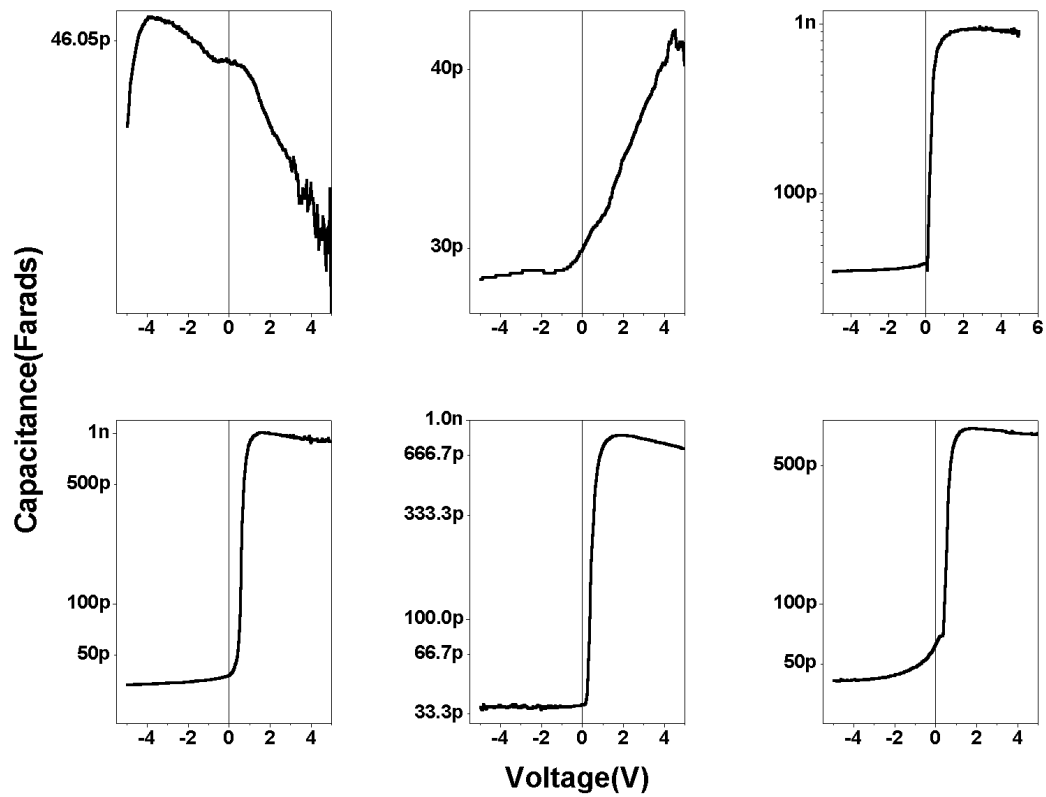


Figure 12: Capacitance-Voltage Measurements of Sodium Implanted ZnO.

- (a) Sodium As-Implanted ZnO
- (b) Sodium implanted and annealed at 250°C
- (c) Sodium implanted and annealed at 300°C
- (d) Sodium implanted and annealed at 350°C
- (e) Sodium implanted and annealed at 400°C
- (f) Sodium implanted and annealed at 450°C

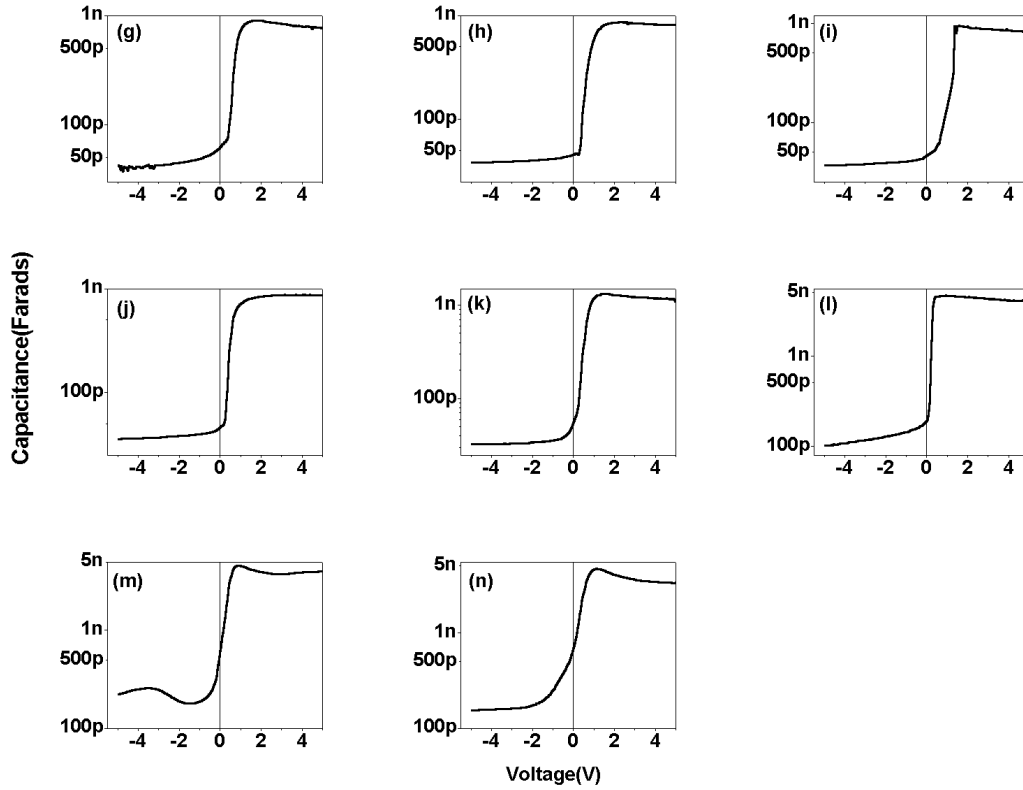


Figure 12: Capacitance-Voltage Measurements of Sodium Implanted ZnO.

- (g) Sodium implanted and annealed at 500°C
- (h) Sodium implanted and annealed at 550°C
- (i) Sodium implanted and annealed at 600°C
- (j) Sodium implanted and annealed at 650°C
- (k) Sodium implanted and annealed at 700°C
- (l) Sodium implanted and annealed at 750°C
- (m) Sodium implanted and annealed at 800°C
- (n) Sodium implanted and annealed at 850°C

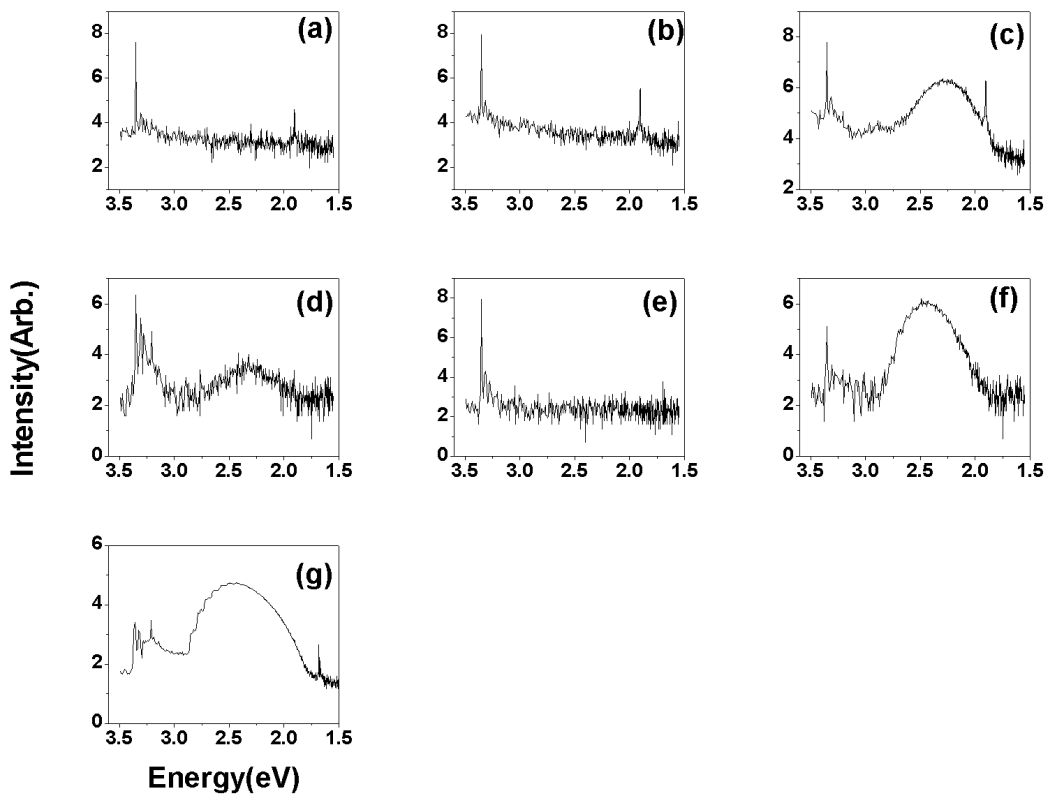


Figure 13: Low Resolution 8K Photoluminescence Spectra of Sodium-Implanted ZnO.

- (a) Sodium As-Implanted ZnO
- (b) Sodium implanted and annealed at 250°C
- (c) Sodium implanted and annealed at 400°C
- (d) Sodium implanted and annealed at 550°C
- (e) Sodium implanted and annealed at 700°C
- (f) Sodium implanted and annealed at 850°C
- (g) Sodium implanted and annealed at 1000°C

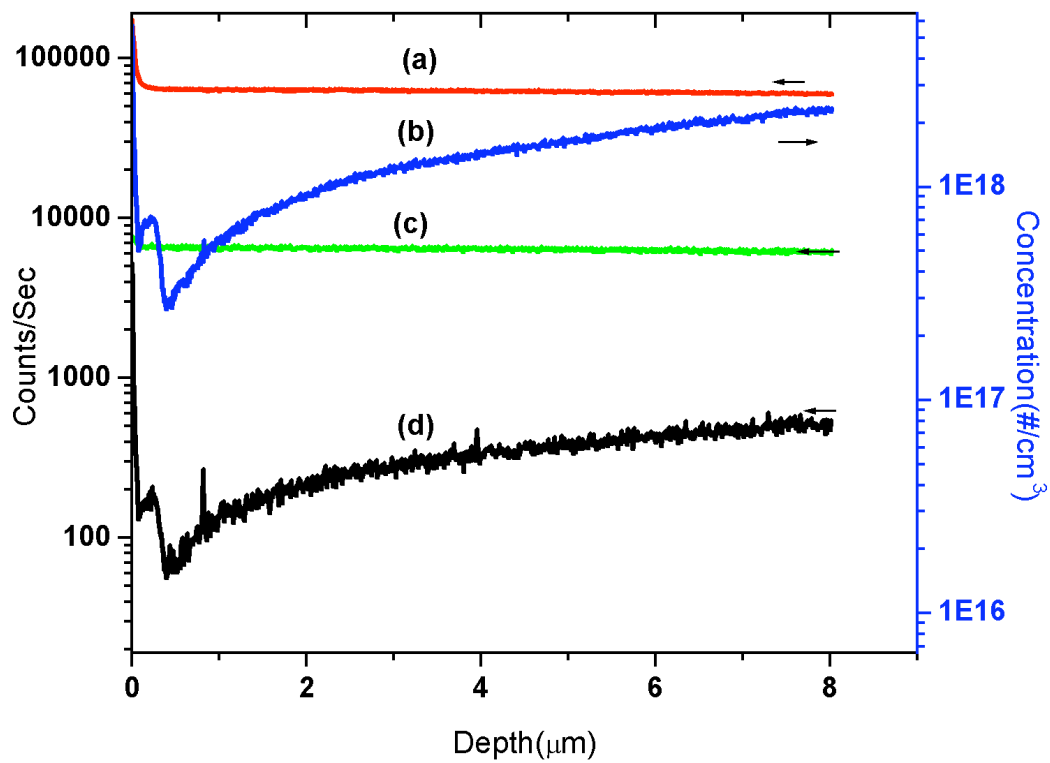


Figure 14: SIMS Profile of Lithium Diffused Substrates.
 Figure 14: a-⁶⁴Zn, b-⁷Li, c-¹⁶O and d-⁶Li.

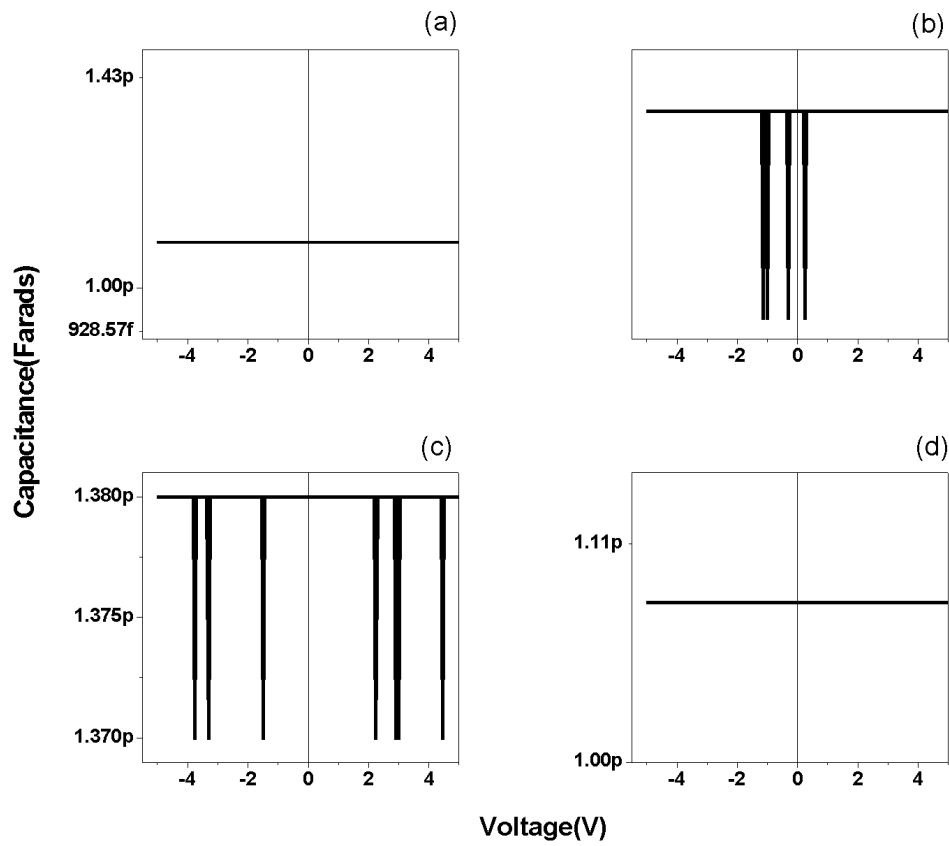


Figure 15: Capacitance-Voltage Measurements of Li-Diffused and Li-N Codoped ZnO.

- (a) Lithium diffused ZnO substrates annealed at 550°C
- (b) Lithium diffused ZnO substrates annealed at 1000°C
- (c) Lithium diffused and Nitrogen Implanted ZnO substrates annealed at 550°C
- (d) Lithium diffused and Nitrogen Implanted ZnO substrates annealed at 1000°C

5. Analysis of Structural Damage and Recovery in Ion-Implanted ZnO Bulk Crystals.

B.T. Adekore^a, R.F Davis^a.

I. Usov^b, B. Patnaik^b, N. Parikh^b.

^aDepartment of Materials Science and Engineering, North Carolina State University,
Raleigh, NC 27695.

^bDepartment of Physics and Astronomy, University of North Carolina at Chapel Hill

5.1. Abstract.

Symmetric ($00l$, $l = 2, 4$ and 6) triple axis X-ray diffraction (2θ - ω , ψ) was employed to characterize damage and recovery of ZnO bulk crystals implanted with metallic and non-metallic atomic species. Structural damage due to the ion-implantation was evidenced and characterized by the very significant broadening of isometric rocking curves along the diffraction vector H , or the radial intensity distribution (2θ - ω). Broadening of the azimuthal intensity distribution or rocking curves in (ψ) also provided an insight into structural factors as the mosaicity of ZnO crystals, the tilt and size of such mosaic blocks and importantly, the effect of ion-implantation on these factors. Thermally activated alleviation of implantation induced satellite peaks and fine structure was also observed at certain temperature ranges for various implants thereby evincing the onset of crystal reconstruction and recovery. These results show qualitatively that the implantation-induced damage in ZnO is characterized by the presence of symmetric satellite peaks and that this implantation damage can be alleviated by the thermally activated elimination of such satellite peaks via controlled annealing.

5.2. Introduction.

Rutherford backscattering was initially employed in this study to characterize ion-implantation damage in ZnO. Consistent with the conclusions of other investigative efforts [1], prominent lattice disordering of the zinc sublattice was observed for substrates implanted with heavier elements such as Silver as seen by the zinc signal in the RBS spectrum of figure 1. It was also obvious from the RBS spectra of heavier implanted species that firstly, the damage sustained was not sufficient to fully amorphize the crystal as there was the absence of an amorphization peak; and secondly, from the damage slant in the proximity of the surface peak highlighted in figure 1, that the damage mechanisms involve very significantly the presence of dislocations. However, the characterization of implantation damage due to lighter elements and for that matter, the thermal alleviation of such damage broached on the limits of RBS sensitivity (Figure 2b). It thus became necessary to employ another technique which when meticulously performed can provide information pertaining to the hydrostatic strain introduced into the crystal through impurity incorporation and the quality of the crystal both upon implantation and progressively as a function of annealing temperature. High resolution X-ray Diffraction provides this avenue of investigating the strain state ($RC(2\theta-\theta)$) of the crystal and the quality ($RC(\theta)$) of the crystal as a function of temperature. The presence of native and non-stoichiometric defects and their contributions to the properties of ZnO (structural, electrical, optical and chemical) has been a matter of significant contention. It is however reasonable to expect a hydrostatic strain contribution from these defects and a temperature variation of such strain if these defects are so prevalent. In fact, a few

investigators agree that the presence of a “built-in” and a hydrostatic strain in virgin and implanted ZnO respectively, affects the spatial location of optical lines of these crystals and in addition possess a temperature dependence [2,3]. Thus it follows that the hydrostatic strain introduced into the crystal by impurity incorporation would be affected firstly by local effects determined by the size of the substitutional impurity and its final lattice position and secondly, by hydrostatic effects due to the innate built-in strain and the generation of additional native defects upon implantation. In as much as RC ($2\theta-\theta$) enables the determination of the strain state of the crystal lattice, it also facilitates chemical understanding into thermally activated solvency i.e. maximum substitution into lattice positions via the disappearance of satellite peaks in RC ($2\theta-\theta$).

Broadening of θ -rocking curves through the increase in the FWHM of (RC (θ)) or for that matter, the width $\Delta(\theta)$ as well as the concomitant and strong polygonization of RC (θ), in fact shows that the quality of the crystal is indeed degraded by ion-implantation. The broadening (in both θ and $2\theta-\theta$) and polygonization (in θ) and their thermally activated variation also indicate that the nature of this lattice degradation involves firstly, the significant enlargement of domain boundaries via increased tilt of mosaic blocks upon implantation; secondly, the expansion and ultimately the local collapse of the lattice into amorphous clusters nucleated within a crystalline matrix upon implantation as well; thirdly, the progressive reconstruction of the crystal with increasing annealing temperature via self-seed recrystallization occurring at the interface between the crystalline mosaic blocks and the amorphous clusters. Polygonization [4], as displayed by the fine structure superimposed on the RC (θ) is indeed the arrangement of dislocations into cell boundaries. However, when these dislocations exist in very high densities as can

be facilitated by implantation damage, the cells comprising of the dislocations collapse through dislocation piling into an amorphous state. Hence, the amorphous clusters nucleated in the crystalline matrix are actually high-density dislocation piles separating crystalline mosaic blocks. Thus, it can be surmised that upon ion-implantation, already existing cell boundaries of low-density random dislocations with minimal coherence length (determined from virgin substrates) are significantly enlarged and ultimately amorphized into very high density dislocation cells of significant coherence length which now separate crystalline mosaic blocks. The foregoing mechanisms are schematically illustrated in figure 3. The innate crystal quality i.e. RC (Δ) of virgin ZnO can not be necessary be improved with increasing annealing temperature as such, the width of RC (Δ) or the FWHM can not be expected to decrease with temperature. However, if polygonization is indeed the mechanism of cluster amorphization, then one can expect a reduction in polygonization with temperature corresponding to the self-seeded recrystallization of amorphous clusters and a reduction in coherence length of dislocation domains with annealing temperature. As we show in subsequent sections, this was indeed observed to be the case and polygonization was greatly reduced to innate levels for implanted samples annealed at high temperatures. The strain state of the crystal correspondingly accommodates the reduction in polygonization as characterized by the variations of FWHM or widths of RC (2Δ) and ultimately the strain with temperature as we show subsequently. Transmission electron microscopy conducted on nitrogen implanted substrates; shown in figure 4, indeed confirm the localization of the implantation damage to the domain boundary or cell separating two mosaic blocks of

single crystallinity. Interestingly, figure 4 also show by the TEM contrast this localization of implantation damage as an amorphous cluster within this domain cell.

5.3. Experiment.

ZnO (000 $\bar{1}$) bulk crystals implanted with Lithium, Nitrogen, Sodium, Aluminum, Argon and Silver were used to investigate implantation damage as function of atomic mass of the species from lithium (6.941g.mol⁻¹) to Silver (107.8662g.mol⁻¹) as well as annealing temperature in 1Atm of oxygen at 25C (As-implanted) and 250C-1000C at an increment, $\Delta T= 150C$. The furnace anneals were also conducted isochronically at 30mins for each sample investigated. Rutherford backscattering was conducted for randomized and aligned positions for virgin and implanted samples as shown in figure 2. XRD investigation was conducted using a high-resolution X-ray diffractometer- Philips X'Pert MRD with a Cu K $\alpha_1 = 1.54\text{\AA}$ and four crystal monochromator in Ge (220) configuration.

5.4. Results and Discussions.

Investigations into the depth or volume (c-orientation) and thickness (a-orientation) variations of implantation damage and recovery mechanisms were facilitated by varying the reflection order of symmetric and asymmetric reflections respectively. Symmetric reflections (00 \bar{l}) of reflection order $\bar{l} = 2, 4$ and 6 were used to investigate the mechanisms over three unit cells while asymmetric reflections 205 and 201 corresponding to inclination, ψ , of 36.91° and 75.09° respectively were utilized in investigating such mechanisms within the crystal thickness or a-plane ($\psi = 90^\circ$). In this study we report investigations for the symmetric reflections only.

5.4.1. Mosaic Tilt and Lateral Coherence:

5.4.1.1. Virgin Substrates:

Mosaicity of virgin ZnO crystals is superposed with the effects of tilt, twist and lateral size of the mosaic blocks of the crystals. The tilt and size of the mosaic blocks can be deconvoluted by considering the dependence of the normalized width ($\Delta\theta \cdot \frac{\sin(\theta)}{\theta}$) of symmetric diffraction profiles on the normalized reflection order ($\frac{\sin(\theta)}{\theta}$) for 00 l , $l = 2, 4$ and 6. The above method was intricately examined by Metzger et al [5] and Heinke et al [6] and has been demonstrated by both authors as a means of obtaining rather accurate tilt of crystalline blocks in material with high mosaicity. From such linear dependence, the tilt angle, θ , is extracted for the inclination of the dependence and the ordinate intercept provides less accurately, an inverse proportionality with the size of the mosaic blocks. Thus the tilt, θ , of the domains can be obtained as function of temperature by measuring $\Delta\theta$ of the 002, 004 and 006 at each annealing temperature ($\theta(T)$). The foregoing technique is presented in figure 5 for extracted the tilt and coherence length ($L_{||} = \frac{0.9}{2y_o}$) at selected temperatures for virgin ZnO. The temperature variation of the extracted angles is also presented in figure 5b for virgin ZnO. If one assumes for simplicity, the uniformity of crystal quality i.e. $\Delta\theta$ is consistent across the surface of the entire bulk substrate, (although it has been shown this is not the case [7]) then the apparent non-linear variation (or parabolic variation with least mean square fit given by

$$\theta = 9e10^{\theta} T^2 + 7e^{\theta} T + 0.0011 \text{ for } 25^{\circ}\text{C} \leq \Delta T \leq 850^{\circ}\text{C}, \text{ where } \theta \text{ is the tilt angle and } T \text{ is}$$

the annealing temperature) of the tilt of virgin substrates on annealing temperature, can indeed be attributed to a thermally activated re-organization of domain cell boundaries that affect the tilt and consequently a thermally activated movement of boundary dislocations that form the cell boundaries. In which case, from figure 5b, one can attribute the maximum tilt attained at 400C as the maximum formation vis-à-vis randomization of the screw dislocations (from $\rho_{\text{screw}} \propto (\text{tilt})^2$ [1, 2]) causing the tilt and the minimum tilt attained at 850C as maximum re-organization of such dislocations and thus effecting a thermally activated transition from high to low angle domains. It is difficult to affirmatively conclude that high temperature processing in oxygen improves the overall quality of the crystal primarily because the least mean square technique progressively fits poorly for higher annealing temperatures as we show in figure 5a and secondarily because this overall improvement was not ratified by other characterization techniques involving optical and electrical characterization. Nonetheless, one can reasonably posit that high temperature processing in oxygen does seem to affect the polygonization of the mosaic structure and in effect, the arrangement and movement of dislocations within and around these domain cells or boundaries. Qualitatively, the reduction in polygonization is visible as from 650C to 850C as shown by the rocking curves RC (\square) of figure 6c to 6e. In the foregoing, it appears the reduction in polygonization occurs at these higher annealing temperatures via the reduction in the density of domains cells separating each crystalline block.

Although the discussion on figure 14 is deferred to subsequent sections, the variation of $\Delta(2\theta-\theta)$ with temperature in figure 14f shows that a maximum is attained in the $\Delta(2\theta-\theta)$ at 700C but thereafter $|\Delta(2\theta-\theta)|$ gradually diminishes. This maximum at 700C may indeed be predicated by the hydrostatic strain created through the generation of Schottky defects such as zinc and oxygen vacancies (figures 11d, 11e and 11f) particularly as the shape of the area map of the first unit cell at this annealing temperature appears strained.

5.4.1.2. Implanted ZnO:

The examination of triple axis area maps ($2\theta-\theta$, θ) of implanted material is quite complicated by the introduction of sub- and fine structure into these maps. Because of this complication we proceed with a primary qualitative examination and presentation of the maps, noting the origin and thermal evolution of the sub- and fine structure to a less accurate quantitative examination considering the extracted tilt angles of the mosaic blocks as well as the ensuing temperature dependence of such tilt angles. In order to minimize the cumbersomeness of presenting area maps of all the considered implantation (Lithium to Silver), we present the case for Silver in comparison to virgin substrates only. Silver being the heaviest element implanted, can be anticipated to effect the maximal crystal damage.

5.4.1.2.1. As-Implanted Substrates:

Upon implantation with silver at a dosage of 10^{15}cm^{-2} , immediately noticeable features as the significant broadening of radial (2θ - θ) and azimuthal (θ) intensity profiles is apparent. It is also very clear that a collapse of the crystal structure did occur because of the apparent disintegration of the once “whole” but broad θ -profile of virgin ZnO shown in figure 7d, 7e and 7f for 002, 004 and 006 reflections respectively into three clear regions consisting of three, two and one distinct regions for 002, 004 and 006 reflections respectively in the silver implanted ZnO. The azimuthal collapse of silver implanted ZnO shows a regressive magnitude of damage with increasing order of symmetric reflections. As shown in figures 7a, 7b and 7c corresponding to the 002, 004 and 006 reflections and first, second and third unit cells, the implantation damage is most prominent in the 002 reflection and least prominent, however still significant in the 006 reflection. We posit that the high angle domain boundaries act as high cross-section points for implantation damage as incoming ions would readily “see” an out-of-plane boundary before approaching an in-plane boundary. Consequently, the domain boundaries are enlarged and amorphized as most damage would be sustained around their vicinity and as a result a collapse of the crystal is seen manifested in the azimuthal profile by regions of high intensity (mosaic single crystal blocks) separated by amorphous regions of nearly unobservable intensity (enlarged domain cells). Again this mechanism is schematically presented in figure 3 and shown empirically, from area maps in the most prominent case of figure 7a.

Lattice strains and distortions can be characterized by the radial intensity distribution (2θ - d). Indeed the sub-structure of Ag-implanted ZnO does show that extensive strain evidenced by three additional structures in 2θ - d , distortion and collapse of the crystal has occurred. Again, we attribute this extensive hydrostatic strain to the introduction of dopant impurities via implantation. The strain qualitatively appears to be most prominent within the 002 reflection and regresses as the reflection order increases.

5.4.1.2.2. Annealed Substrates:

Alleviation of the extensive strain and distortion in 2θ - d as well as the collapse of the crystal in d commenced upon annealing the crystal at 250C. The mechanisms of crystal recovery can be postulated to involve the lateral self-seeded recrystallization of amorphized domain cells occurring at the interface between the domain cells and the crystalline mosaic blocks. Figure 8a shows by the appearance of intensity lines in initially amorphized regions that recrystallization commences at 250C. Lateral growth of mosaic blocks at the expense of amorphous domain cells continues at 400C as seen by the coalescence of sub-structure or satellite peaks in the radial (2θ - d) and azimuthal directions (ϕ) shown in figure 9a for 002 reflection. However, because only a coalescence is occurring and not an elimination, particularly in 2θ - d , it is obvious that further thermal activation of the crystal would be required to minimize or better still, eliminate the satellite peaks. Reconstruction of 004 and 006 appears to be very significant at 400C with the 2θ - d , ϕ maps qualitatively similar to those of virgin substrates of corresponding reflections annealed at the same temperature. This fact demonstrates the

shallow localization of the bulk of the damage i.e. within the first unit cell, after the 400C anneal.

Samples annealed at 550C demonstrate the elimination of satellite peaks in 2θ for 004 and 006 reflections indicating the elimination of lattice collapse due to hydrostatic strain. These reflections at 550C also show the elimination of lattice interruption in the azimuthal direction, ϕ , whereas in previous cases (the as-implanted case), the ϕ -profile was characterized by crystalline regions separated by large amorphous regions into one, two and three distinct regions for the 006, 004 and 002 reflections respectively. It is reasonably posited therefore, that the reconstruction of deeper unit cells, i.e. the second and third unit cells of the crystal which have sustained less damage relative to first unit cell, had undergone a complete reconstruction at 550C as shown in figure 10b and 10c for the 004 and 006 reflections respectively. The 002 reflection of samples annealed at 550C demonstrate remarkable attributes as further coalescence of the satellite peaks in 2θ into an extension or broadening of the main peak is shown in figure 10a. The above coalescence indicates a reduction of the strain state of the crystal and in essence, an increase in impurity incorporation into lattice positions within the crystal. Such incorporation of silver impurities into substitutional sites and hence dopant activation would reduce strain and collapse of the lattice that resulted from both damage and “mis-incorporation” of an oversized silver ion into an interstitial lattice position. The 2θ , ϕ map of the 002 reflection also show the complete elimination of lattice interruption in both the azimuthal (ϕ) and radial (2θ) directions of intensity at 550C and thus the recrystallization of very large amorphous domain into mosaic blocks. Apart from the further alleviation of the reduced hydrostatic strain from dopant impurities, the structural

integrity of the crystal is clearly restored at 550C. Additional thermal energy in excess of that applied at 550C would primarily to drive the further activation of impurities via impurity substitution on lattice sites and in effect reduce the strain state of the crystal by the elimination of the 2θ -broadening. We make a clear distinction here between the satellite peaks in 2θ and 2θ broadening. In which case satellite peaks are a result of excessive broadening in 2θ separated by amorphous regions and hence an interruption of the lattice while in the case of the 2θ -broadening, there are no longer any distinct separation or interruption of the lattice into several structures.

The foregoing is indeed demonstrated at 700C wherein the strain is further minimized by the very apparent reduction and approximate elimination of the coalesced broadening as shown in figure 11a. However, as previously mentioned, at 700C and above virgin samples show a shape alteration for 002 reflections speculatively because of the generation of Schottky defects at this temperature. The effect can be said to carry over for 002 and higher order reflections of silver implanted samples of figure 11b and 11c respectively.

Further application of thermal energy by annealing the crystal to 850C further complete absorbs the broadening into the main peak as shown in figures 12a, 12b and 12c. It becomes difficult at these elevated temperatures to distinguish between the variations in 2θ due to hydrostatic strain created by extrinsic impurities and the strain created by the generation of intrinsic Schottky defects. In any case, satellite peaks in 2θ have long been eliminated at 550C; mention is barely made of satellite peaks in θ as this has completely been eliminated at 550C as well and an “uninterrupted” crystal has been regained; thus it can be conclusively determined that residual broadening is partly shared

by hydrostatic effects of both dopants incorporation and native defect generation. It can also be anticipated that as dopant incorporation increases with increasing annealing temperature, such 2θ broadening would commensurately decrease. As we show subsequently, the former is indeed the case and the magnitude of $\Delta(2\theta)$ continuously decreases with increase in temperature. The qualitative shape of 2θ approaches that of a hexagonal unit cell i.e. hexagonality as shown by the area map at 850C (figure 12a) for the 002 and 004 reflections indicating maximal crystal recovery as well as maximal dopant incorporation occurs at this temperature. However, this hexagonal outline is clearly strained as we show in figure 13a and 113 for samples annealed at 1000C for the 002 and 004 reflections respectively. Such new strain effects would only be due to the presence and prevalence of the hydrostatic strain contributions of native Schottky defects as maximum crystal repair and dopant incorporation appears to have been completed at 850C. This new strain is another indication or for that matter, verification of the activity of point defects notably, zinc and oxygen vacancies at temperatures in excess of 1000C. We had previously shown by optical luminescence that the “reactivation” of features particular to native defects is very prominent at annealing temperatures in the vicinity of 850C [8]. From the 2θ , Δ area maps at 850C and 1000C (figures 12 and 13) it is also apparent that this new strain is localized to the first and second unit cell as the 006 reflection qualitatively does not appear affected. Because of this shallow localization, one can attributed the generation of Schottky defects to competing sublimation mechanism that begin to degrade the quality of the crystal above 1000C. Conclusively, the magnitude of $\Delta(2\theta)$ of Ag-ZnO continuously decreases with increasing temperature as shown in figure 14g. The decrease is somewhat stabilized from 700C to 850C indicating maximum

incorporation of dopant impurities. Hydrostatic strain effects of native defects further effect a continuous decrease beyond 850C however at the expense of lattice distortion of the unit cell as seen in figure 12a for the 002 reflection.

The variations in the extracted tilt angle of implanted ZnO with temperature are less accurate because of the poor least mean square fit of the high temperature data points. However, figure 15 shows the variation for the species mentioned in this study. It can be seen from figure 15g that there is a very significant drop in the tilt angle upon application of thermal energy for the silver impurity. After this initial drop, the tilt increases linearly with temperature from 250C to 1000C, however the final tilt is significantly much less than the tilt in the as-implanted state. Thus upon annealing, there is indeed a change from the high angle mosaic blocks in the as-implanted state to lower angle blocks in the recrystallized state. The case for other impurities is discussed in their respective sections.

5.4.1.2.3 Other Implanted Impurities:

For brevity and simplicity, the follow discussion has been limited to the first unit cell or the 002-reflection. The general behaviour of higher order reflections does replicate the behavior of the 002-reflection however, to a much lesser extent.

5.4.2. Thermal Response:

5.4.2.1 Nitrogen:

Quantitatively, in magnitude of the 2θ width with increasing temperature and atomic mass of implanted impurities is shown in figure 14 for the 002 reflection. The figure clearly distinguishes the “thermal response” of the oxygen and zinc sublattice especially among species of comparable atomic masses i.e. nitrogen (14.007g mol^{-1}), sodium (22.990g mol^{-1}) and aluminum (26.982g mol^{-1}). It can be seen from figures 14b, 14c and 14d corresponding to the thermal response of nitrogen, sodium and aluminum, that a somewhat sharp transition from highly damaged state characterized by a large $\Delta(2\theta)$ -due to lattice interruption, to a reconstructed but strained state-due to dopant incorporation occurs from 250-400C for the nitrogen implant. Thereafter, a gradual but continuous decrease in the magnitude of $\Delta(2\theta)$ occurs to an open minimum at 1000C (i.e. samples above 1000C were not investigated). This continuous decrease in $\Delta(2\theta)$ beyond 400C is again indicative of continuous incorporation of nitrogen dopants into the oxygen sublattice and thus minimizing the magnitude of $\Delta(2\theta)$.

5.4.2.2. Sodium and Aluminum:

The atomic masses of sodium and aluminum provide a method of studying the recovery of intermediate mass species. In the case of sodium, a sharp transition (from the damaged to a reconstructed state of the crystal) is observed at the much higher temperature interval 700-850C vis-à-vis the recrystallization temperature interval of nitrogen at 250C-400C. For sodium, the continuous decrease in the magnitude of $\Delta(2\theta)$ continues to the open

minimum at 1000C (figure 14c). In considering the case of aluminum, it is apparent that this sharp transition is lost to a more gradual and graded transition occurring after 550C. The graded transitions of aluminum and of silver (figures 14d and 14g) both operative on the zinc sublattice, maybe indicative of a change in the thermal response of the crystal for atomic masses greater than that of sodium. In which case the response of the crystal is altered to a more gradual and graded response rather than an abrupt and sharp response as we have seen for sodium and nitrogen even though nitrogen is operative on the oxygen sub-lattice. The new thermal response mechanism indicates that the damage created by heavier implants is less progressively annealed out in the case of hydrostatic point defects as vacancies or that the density and size of amorphous clusters generated upon implantation with species heavier than sodium may indeed be higher.

5.4.2.3 Lithium:

Lithium with atomic mass of 6.941 gmol^{-1} was expected and indeed observed to have the least or most minimal damage on the ZnO crystals given the quality of crystals are comparable[†]. Crystal integrity shown by RC (\square) as well as lattice collapse due to excessive hydrostatic strain in the as-implanted state was restored and alleviated respectively after annealing the crystal at 250C. Figure 14a along with 2θ - θ , \square maps show a quick thermal response of the crystal to the implantation damage. The increase in the magnitude of $\square(2\theta-\theta)$ seen after 250C to a maximum at 750C is very similar to that of virgin ZnO shown in figure 14f. After recovery from minimal crystal damage at 250C, the lithium-implanted crystal could be said to behave just as annealed virgin crystals with

[†] Bulk crystals of very large virgin rocking curves, i.e. $\text{RC}(\square) \geq 1.2^\circ$ or in excess of $1500''$ undergo very significant damage even with lithium-implantation and are only recovered at temperatures beyond 750C even with lithium-implantation only.

both attaining a maximum in $\Delta(2\theta-\theta)$ at 700C and decreasing to the now common open minimum at 1000C. Thus mechanisms responsible for the temperature variation of $\Delta(2\theta-\theta)$ in virgin ZnO are equally as prominent in lithium implanted and annealed substrates.

5.4.2.4. Argon Implanted and Virgin Crystals:

The thermal response of virgin ZnO could be interpreted as the variation of the “built-in” strain of the crystal. It is seen that the magnitude of $\Delta(2\theta-\theta)$ increases to a maximum at 700C and thereafter decreases to an open minimum at 1000C. This variation could be attributed to strain effects following the thermodynamics and generation of hydrostatic point defects with increasing annealing temperature [9].

Argon-implanted samples tend to follow the gradual and graded thermal response as shown in figure 14e with the downward turn in the broadening occurring at the 400-550C temperature interval. Again confirming the tendency of crystals implanted with atomic masses greater than that of sodium having a much more gradual and graded thermal response rather than the abrupt and sharp transition of the converse.

5.4.3. Extracted Tilt of Implanted Substrates:

As was mentioned in our discussion of silver implanted ZnO, the extracted tilt-temperature relationship is less accurate because of poor high temperature data fit.

However certain trends are still observable. In the case of nitrogen, besides, the initial and rapid drops in the tilt angle of nitrogen implanted ZnO, the tilt of nitrogen implanted substrates does not appear to vary very significantly with temperature. The tilt appears to

remain in the vicinity of an average value as the annealing temperature is increased. This may show that recrystallized blocks and mosaic blocks maintain the same orientation before and after annealing. Figure 15b shows that this average value is greatly reduced from the tilt value upon implantation.

The temperature-tilt variation of sodium and aluminum is presently ambiguous and may require further investigations at more intermediate temperature increments i.e. $\Delta T < 150\text{C}$. However, the trends are presented in figure 15c and 15d in which it can be seen from figure 15c that for sodium implanted substrates, the drastic drop in tilt was delayed to 400C from the maximum value at 250C. Also, contrary to the now expected initial decrease observed in other implanted from as-implanted state to 250C there was an initial increase in the tilt value to a maximum at 250C. Finally, there was the emergence of a local maximum as the annealing temperature was increased to 850C. The local maximum was observed to be 70% of the maximum value at 250C. Figure 15d shows a less ambiguous temperature-tilt variation for Aluminum. The initial drastic drop was also not observed but like sodium, an initial increase in tilt from the as-implanted to a maximum at 250C was observed for aluminum. The tilt values also remained independent of temperature until the 700C-850C interval wherein a drastic minimum was observed at 850C.

The tilt variation of virgin ZnO substrates already previously discussed and shown in figure 5b show a maximum at 400C after which a gradual but consistent decrease is seen to 1000C. The behavior of the tilt-temperature variation of argon-implanted ZnO follows well that of nitrogen and silver in that there was the initial and drastic drop in tilt value from the as-implanted state to the 250C anneal. Thereafter, a linear increase with

temperature is observed continuously to 1000C. In this case the finally value at 1000C is also less than the initial maximum value at 25C (the as-implanted state).

5.5. Conclusions.

The above study has been able to provide a structural insight into the crystal integrity and impurity accommodation of ZnO bulk substrates. We have been able to determine empirically, on a case-by-case basis, the temperature range in which implanted crystals recover from implantation damage via the minimization of radial broadening and the elimination of radial satellite peaks. We have also been able to develop as a mechanism for crystal damage i.e. the disintegration of azimuthal intensity into multiple satellite peaks. We attributed this collapse of the lattice or lattice interruption to the conversion of thin domain boundaries that separate mosaic blocks into broad amorphous region or clusters via the piling of dislocations at high densities into these boundaries. We have established that the mechanism of crystal reconstruction involves the lateral self-seeded recrystallization occurring at the interface of the amorphous cluster and the crystalline mosaic block.

5.6. Acknowledgements.

B.T. Adekore acknowledges S. Einfeldt for his insightful conversations, availability and direction; in essence his invaluable contributions to the XRD study. B.T. Adekore also acknowledges the relentless efforts of H. McClean in obtaining the transmission electron micrographs of figure 4., as well as the contributions of E. Preble in the XRD studies.

The time, efforts and insightful discussion of and with I. Usov, B. Patnaik and N. Parikh in the RBS study is also tremendously appreciated.

5.7. References.

- [1]. Y. Ohta, T. Haga, Y. Abe, “Crystallographic Features of ZnO single crystals”, Jpn J. Appl Phys 36, L1040-L1042, Part 2, No 8H, 1997.
- [2] D.C, Reynolds, D.C Look, B. Jogai, R.L Jones, C.W. Litton, W. Harsh and G. Cantwell, “Optical properties of ZnO crystals containing internal strains”, Journal of Luminescence, Vol 82 1999, Pp 173-6.
- [3]. B.T. Adekore, D.W. Barlage, R.F. Davis, “Acceptor Conductivity in Bulk (000 $\bar{1}$) ZnO via Implantation of Nitrogen Ions. In Press.
- [4]. I.P. Nikitian, R.C. Glass, E. Janzen, N.B. Guseva, A.A. Mal'tsev, “Structural analysis of 4H-SiC layers grown on 6H-SiC and 15R-SiC substrates”, Journal of Crystal Growth, Vol.152 (1995) Pp292-299.
- [5]. T. Metzger, R. Höpler, E. Born, “Defect structure of epitaxial GaN films determined by transmission electron microscopy and triple-axis X-ray diffractometry”, Philosophical Magazine A, Vol. 77(1995), No. 4 Pp1013-1025.
- [6]. H.Heinke, V. Kirchner, S. Einfeldt, D. Hommel, “Analysis of the Defect Structure of Epitaxial GaN”, Phys. Stat. Sol. (a) Vol. 176 (1999) Pp 391-5.
- [7]. T.P. Smith et al, Private Communication and Dissertation work on Heteroepitaxy and Homoepitaxy of ZnO films.

[8]. B.T. Adekore, D.W. Barlage, R.F. Davis, “Acceptor Conductivity in Bulk (000 $\bar{1}$) ZnO via Implantation of Nitrogen Ions. In Press.

[9]. B.T. Adekore, D.W. Barlage, R.F. Davis, “Capacitance Measurements of Argon Implanted and Annealed ZnO (000 $\bar{1}$) substrates”. In press.

5.8. Figures.

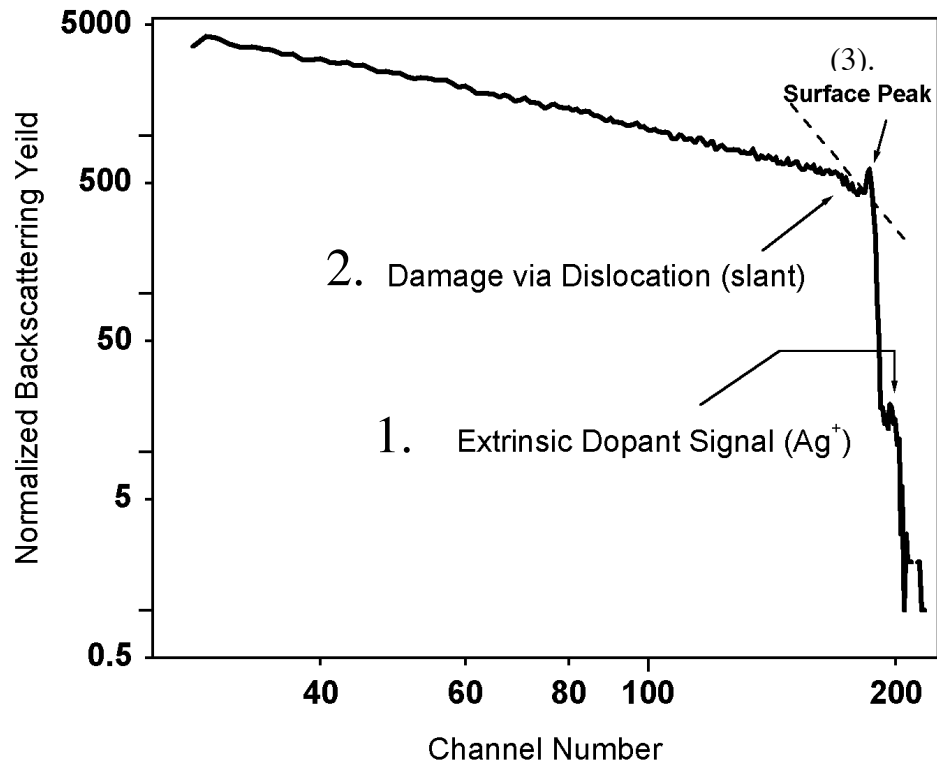


Figure 1a: Aligned Rutherford Backscattering Spectra of Silver As Implanted Substrates.
Highlighting : (1). the Signal of Ag⁺ , (2) the prevalence of Dislocation piling as the damage mechanism through the indicated slant in the dechanneling level, (3) the Surface peak.

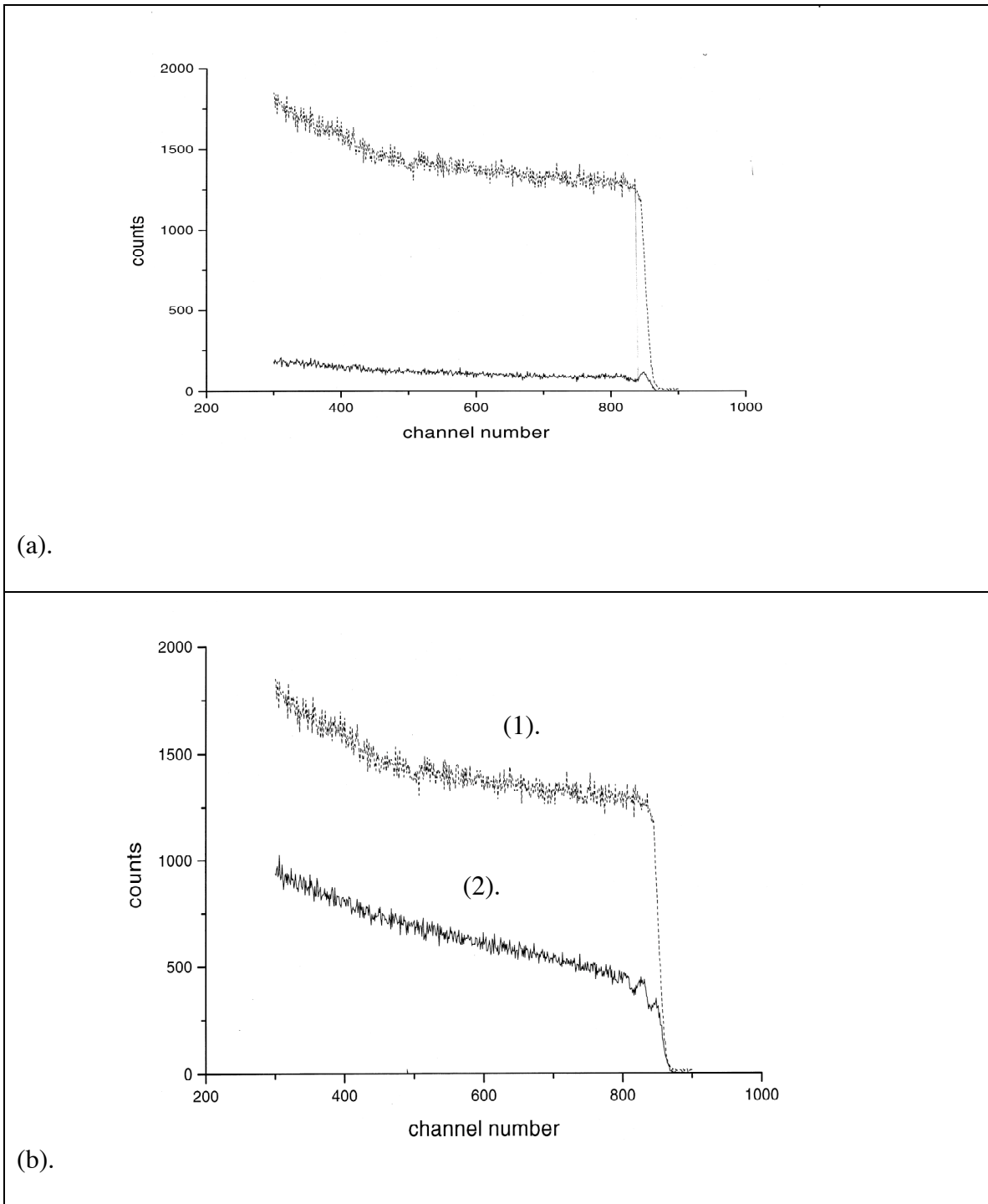


Figure 2: Rutherford Backscattering Spectra of ZnO
Figure 2a: Virgin ZnO, Random (1) and Aligned (2).
Figure 2b: Nitrogen Implanted ZnO, Random (1) and Aligned (2).

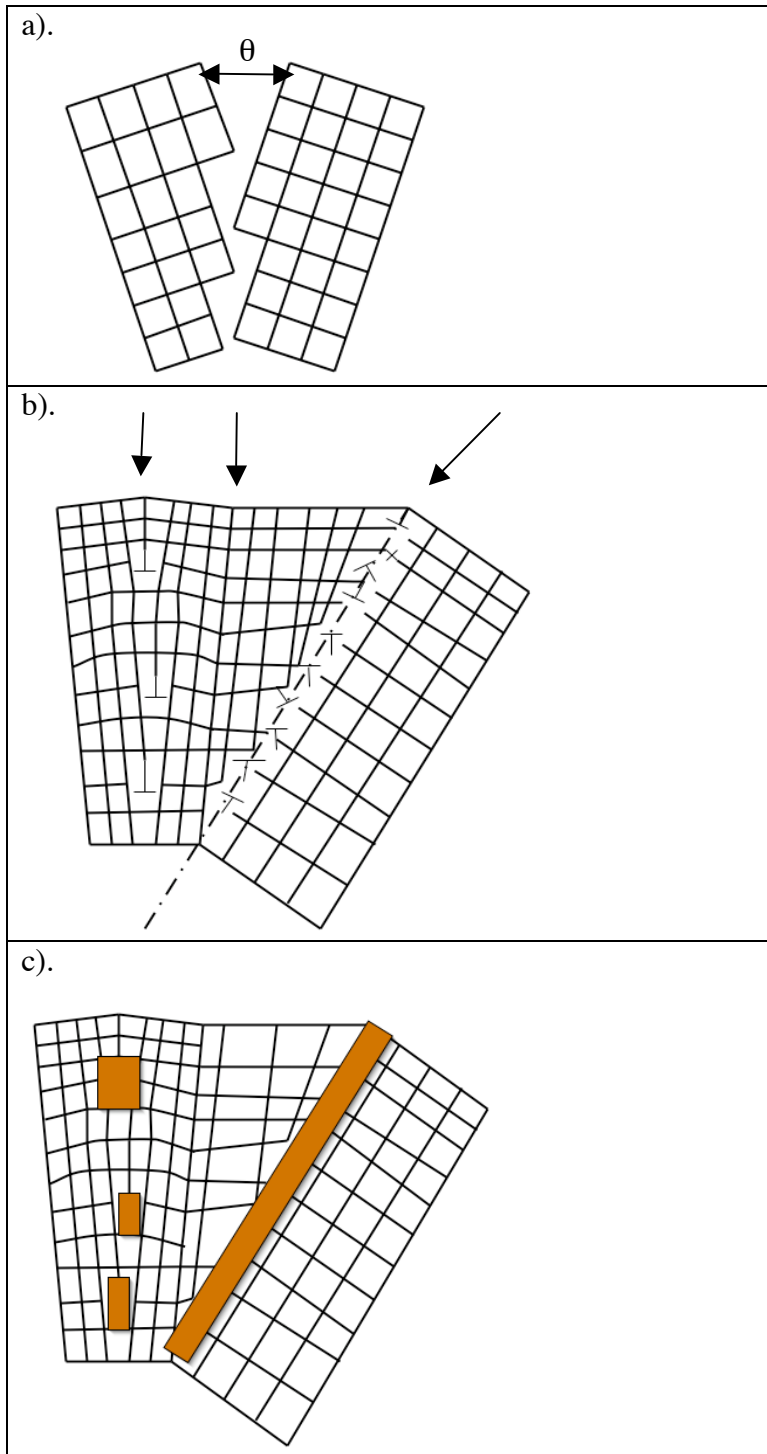


Figure 3: Schematic Illustration of the Damage Propensity in High angle tilt boundary.
 Figure 3a: Low angle tilt domain.
 Figure 3b: Low and high angle domain boundaries with high cross-section for implantation damage.
 Figure 3c: Amorphous clusters nucleated within single crystalline mosaic matrix.

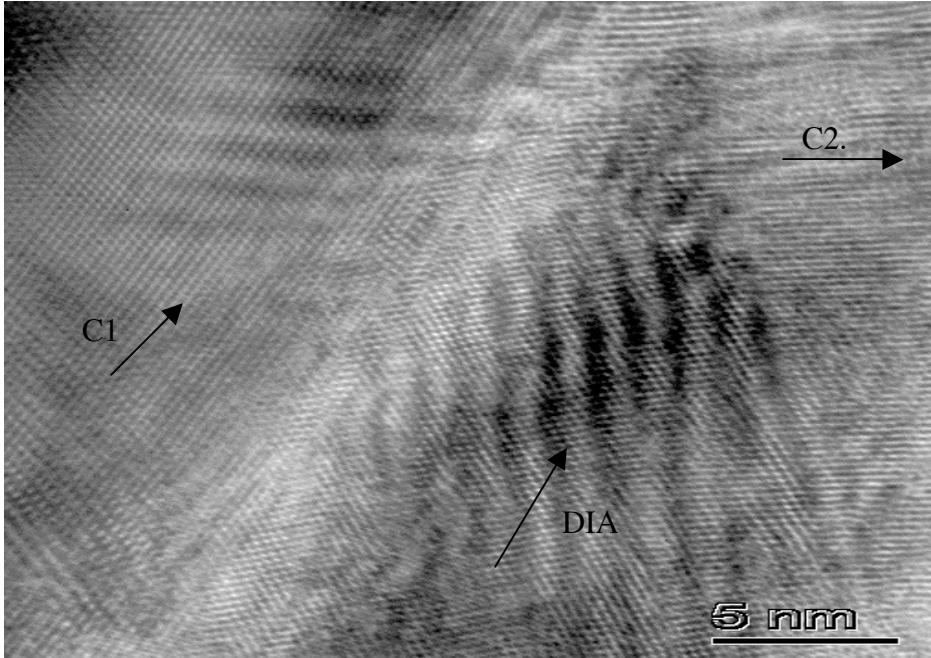


Figure 4: Transmission Electron Micrograph of Nitrogen-Implanted ZnO. Where C1 and C2 are two single crystal sub-grains with different crystallographic orientation. DIA is the Dislocation Induced Amorphization of the interfacing domain boundary of the misoriented sub-grains.

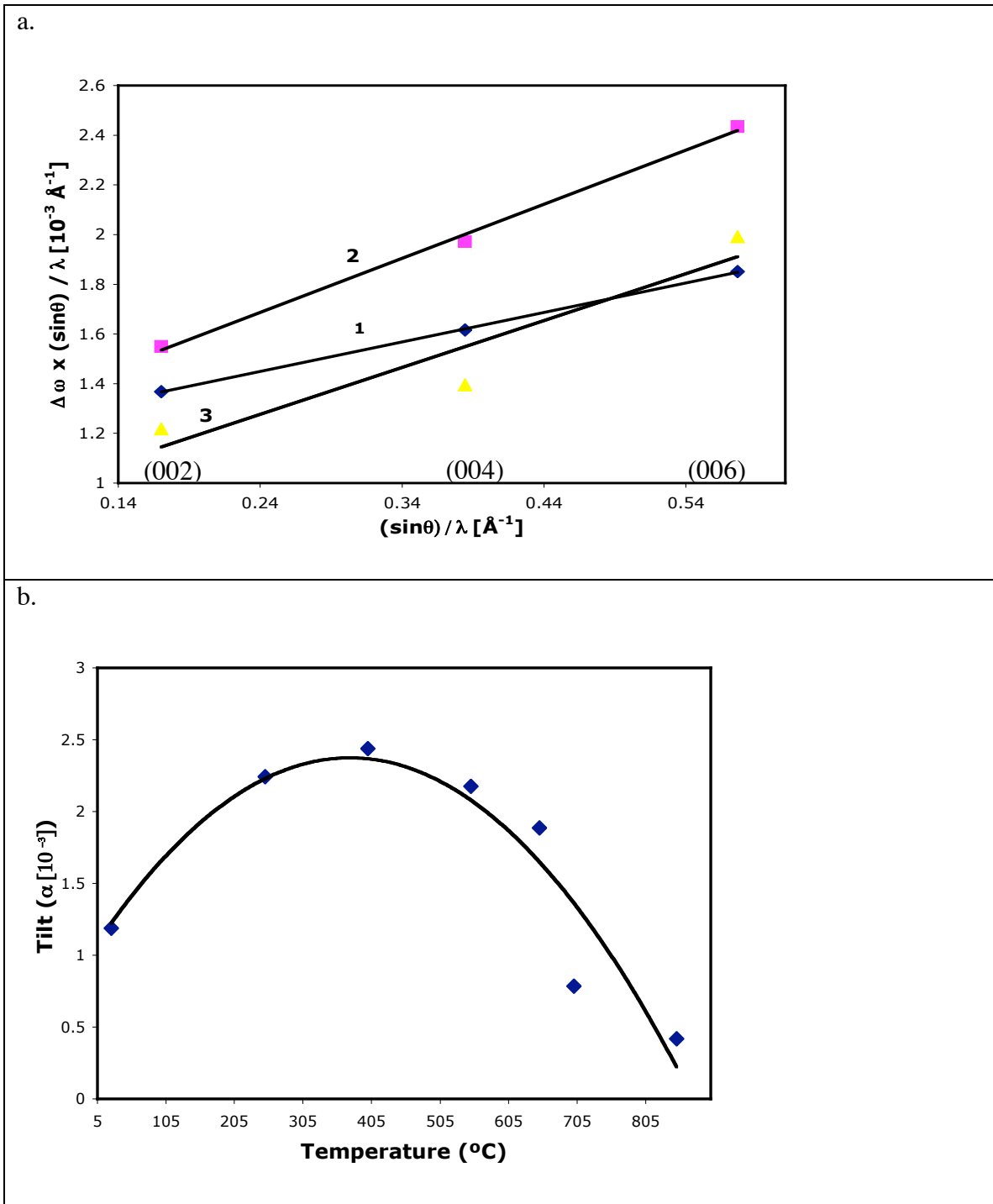


Figure 5: Isometric Variation in Δd with Reflection Order for Virgin ZnO.

Figure 5a: Isometric variation in Δd with Reflection Order for Virgin ZnO at 25°C (1.)

Virgin ZnO annealed at 550°C (2.) and

Virgin ZnO annealed at 650°C (3.)

Figure 5b: Variation of Tilt angles (θ) with Annealing Temperature.

Parabolic least mean square fit as: $\theta = 9e10^{-9} T^2 + 7e^{-9} T + 0.0011$, $R^2 = 0.8812$.

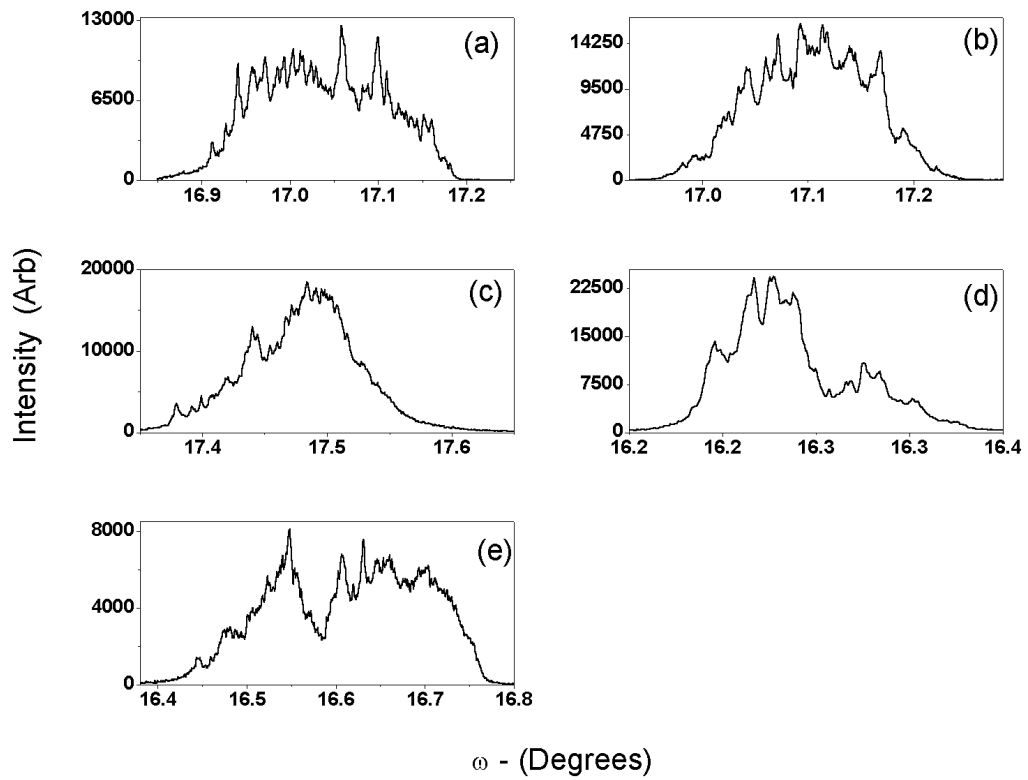


Figure 6: 002-reflection ω -Rocking Curves of Annealed Virgin ZnO.
 Figures 6a: samples at 25C, 6b: samples at 550C, 6c: samples at 650C, 6d: samples at 700C, 6e: Samples at 850C.

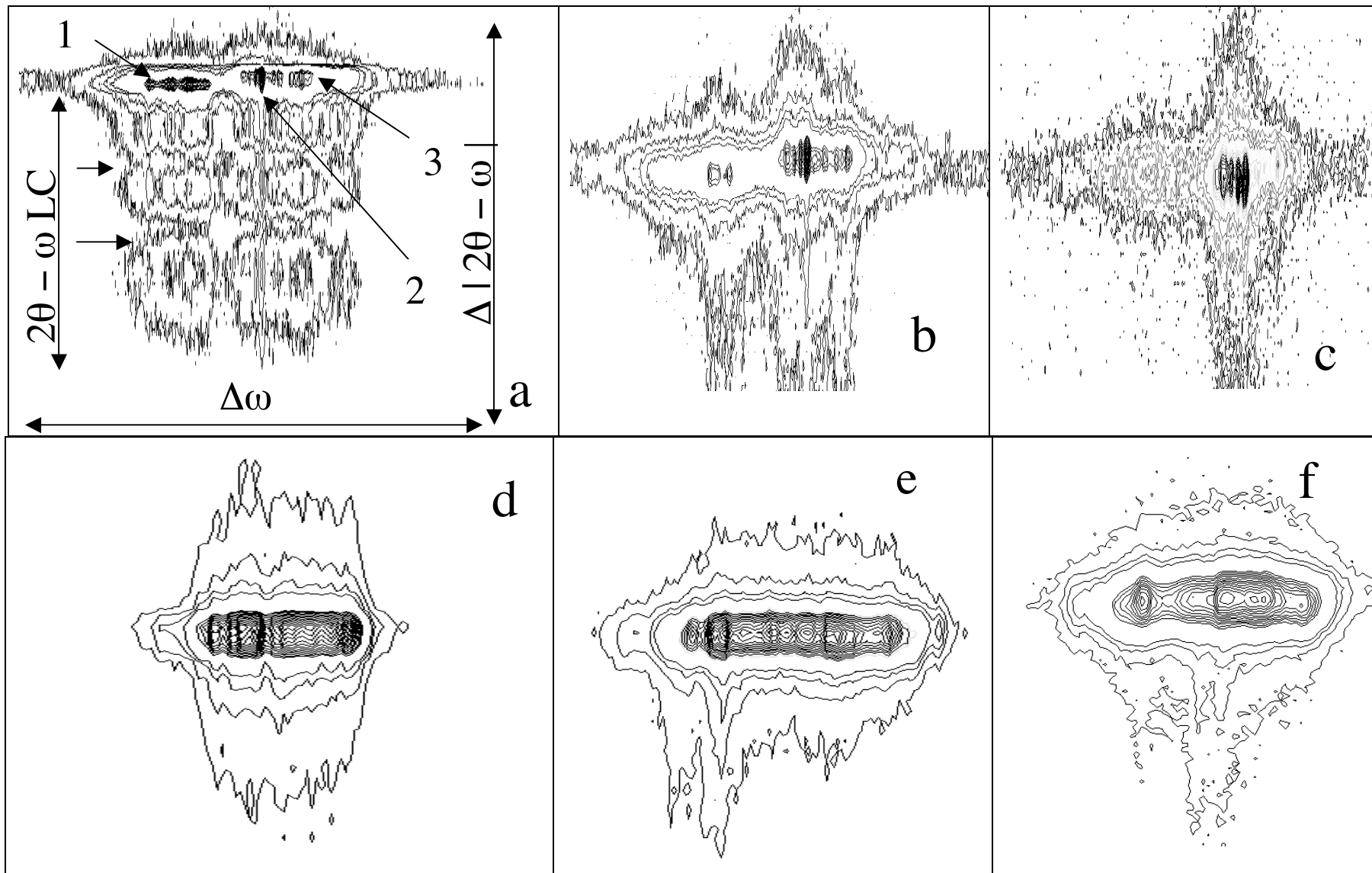


Figure 7: $2\theta - \omega$, $\Delta|2\theta - \omega|$ Area Maps of Silver Implanted and Virgin ZnO. Figure 7a: Silver as-Implanted (002) showing the $2\theta - \omega$ axis (abscissa) and the $\Delta|2\theta - \omega|$ axis as the ordinate. Also showing lattice collapse (LC) in both $2\theta - \omega$ and $\Delta|2\theta - \omega|$ (1,2,3). Figures 7b and 7c: (004) and (006) reflection of Silver as Implanted samples respectively. Figures 7c, 7d and 7e (002), (004) and (006) reflections of Virgin ZnO at 25°C respectively.

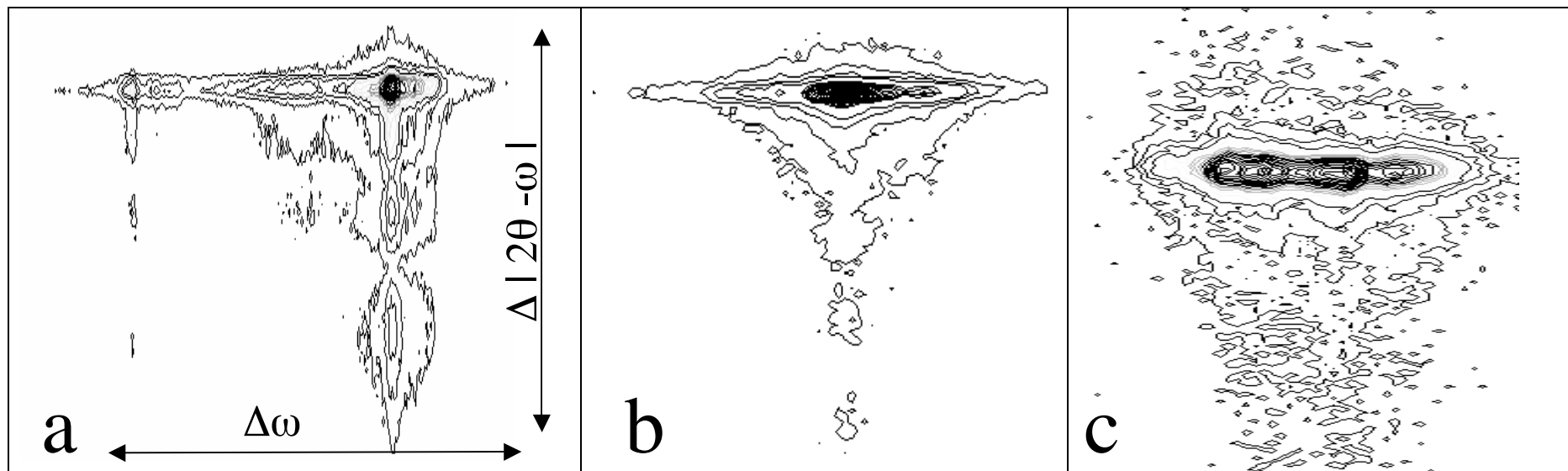


Figure 8: 2D Area Maps of Silver Implanted ZnO annealed at 250°C.

Figure 8a showing the commencement of lattice reconstruction for the (002) reflection. Figures 8b and 8c also shown lattice reconstruction for the (004) and (006) reflections respectively.

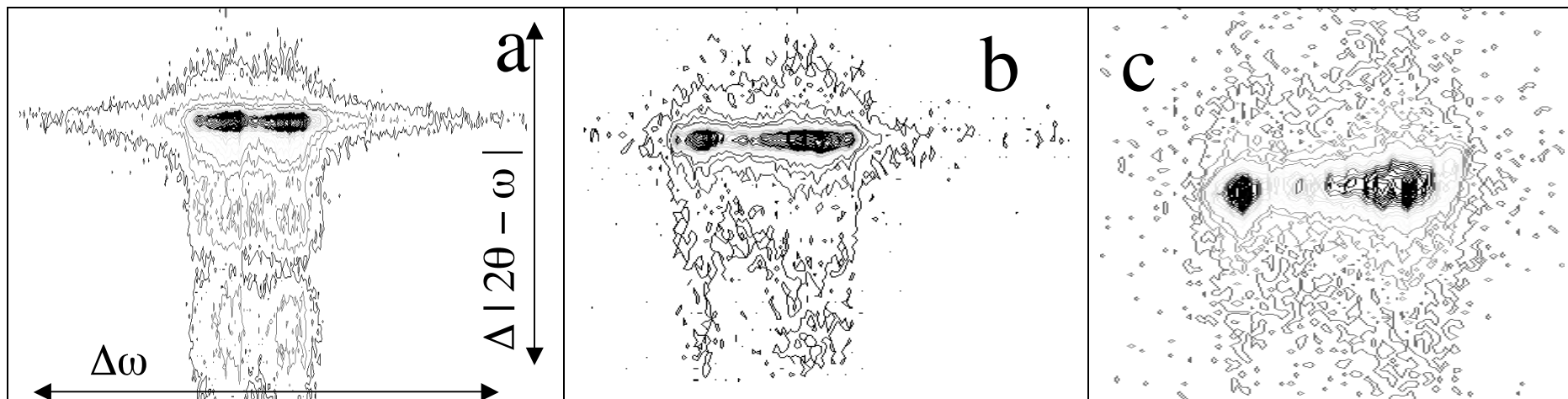


Figure 9: 2D Area Maps of Silver Implanted ZnO annealed at 400°C.
 Figures 9a, 9b and 9c showing the maps for (002), (004) and (006) reflections respectively.

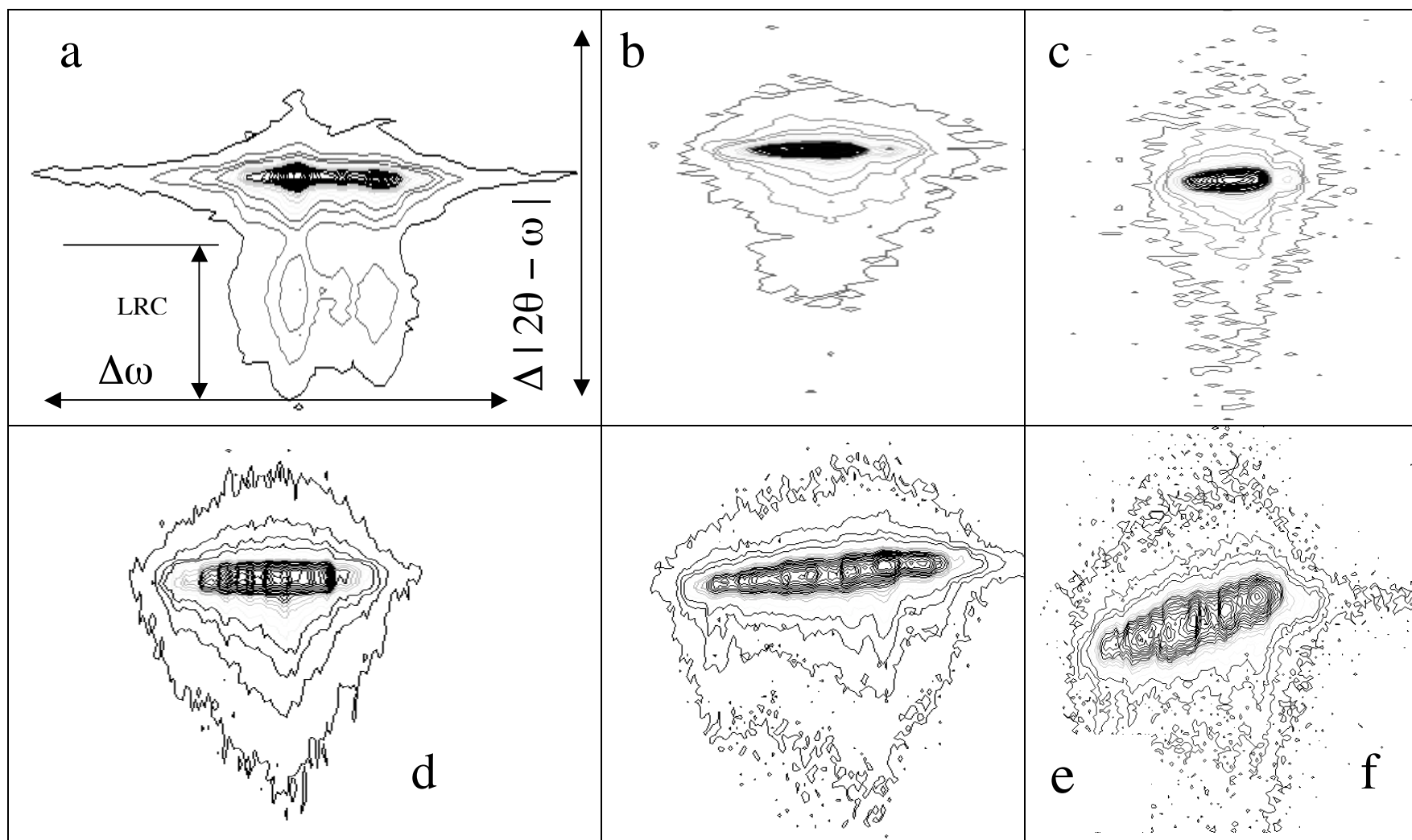


Figure 10: 2θ - ω Area Maps of Silver Implanted and Virgin ZnO annealed at 550°C. Figure 10a: Showing the completion of Lattice reconstruction (LRC) in 2θ and the advancement of LRC in 2θ - ω of the (002) reflection. However, the presence of a satellite peak is still noted. Figures 10b and 10c, the complete reconstruction of the (004) and (006) reflections respectively. Figure 10d, 10e and 10f showing the (002), (004) and (006) reflections for Virgin ZnO annealed at 550C and the broadening or strain in 2θ - ω .

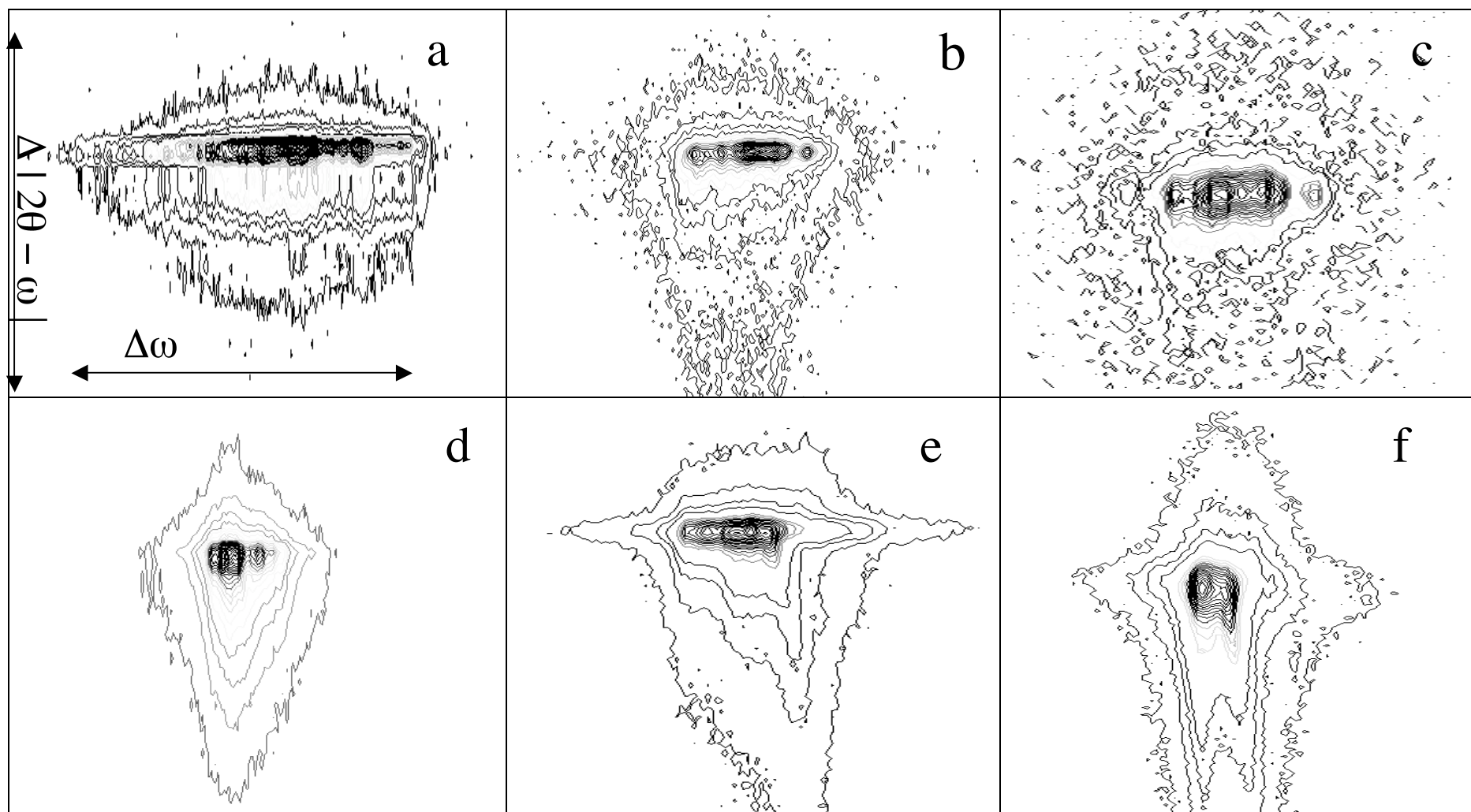


Figure 11: $2\theta - \omega$ Area Maps of Silver Implanted and Virgin ZnO annealed at 700°C.

Figure 11a: Showing further advancement in reduction of satellite peaks as well as complete LRC in $2\theta - \omega$ of the (002) reflection. Figures 11b and 11c, the complete reconstruction of the (004) and (006) reflections respectively. Figure 11d, 11e and 11f showing the (002), (004) and (006) reflections for Virgin ZnO annealed at 550°C and advanced broadening or maximum hydrostatic strain in $2\theta - \omega$.

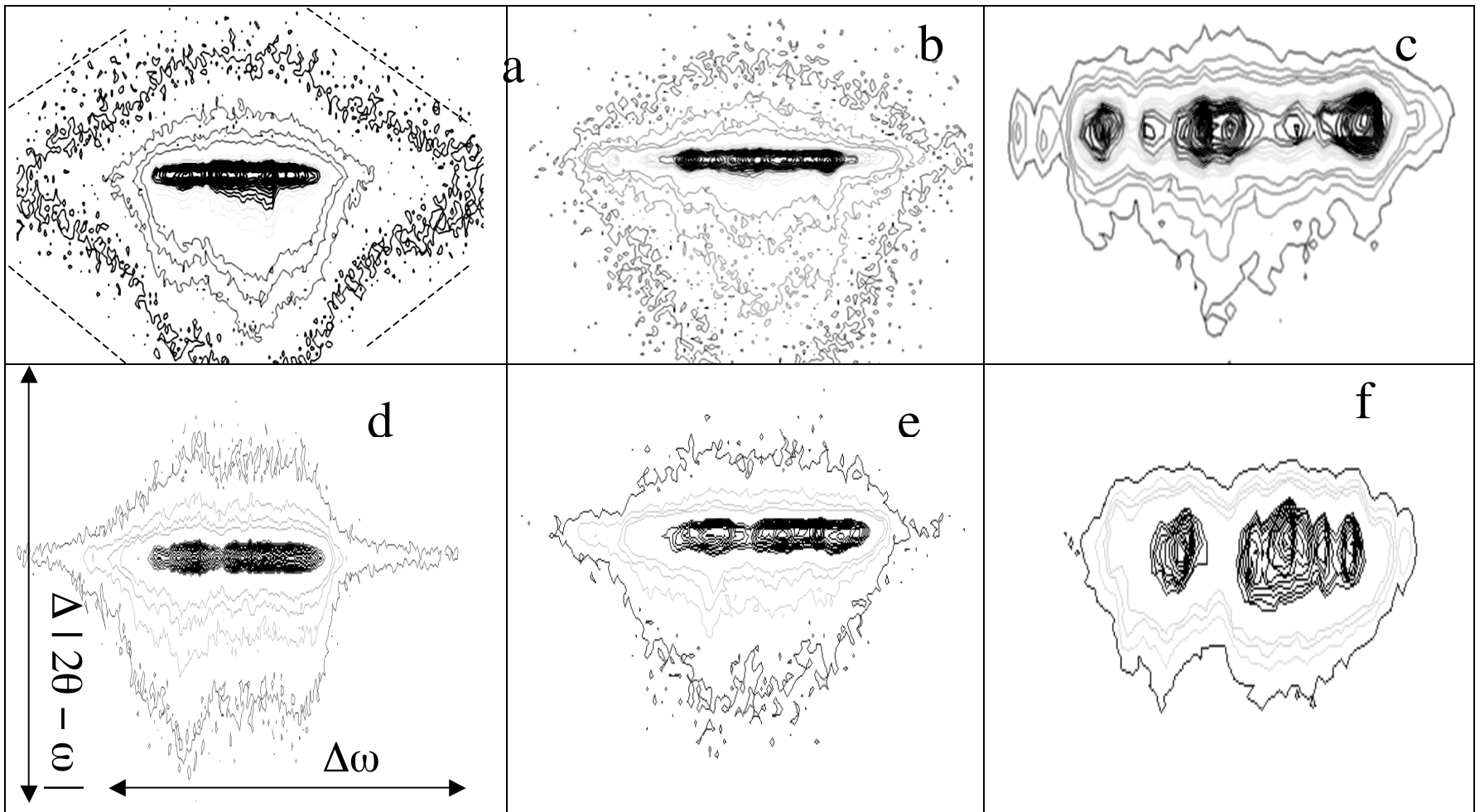


Figure 12: 2θ , ω Area Maps of Silver Implanted and Virgin ZnO annealed at 850°C.

Figure 12a: Showing complete elimination of satellite peaks as well as the resumption of the unit cell outline i.e. hexagonality as shown by the dashed outline in the (002) reflection. Figures 12b showing hexagonality of (004) reflection Figure 12c: the (006) reflection. Figure 12d, 12e and 12f showing the (002), (004) and (006) reflections for Virgin ZnO annealed at 850°C.

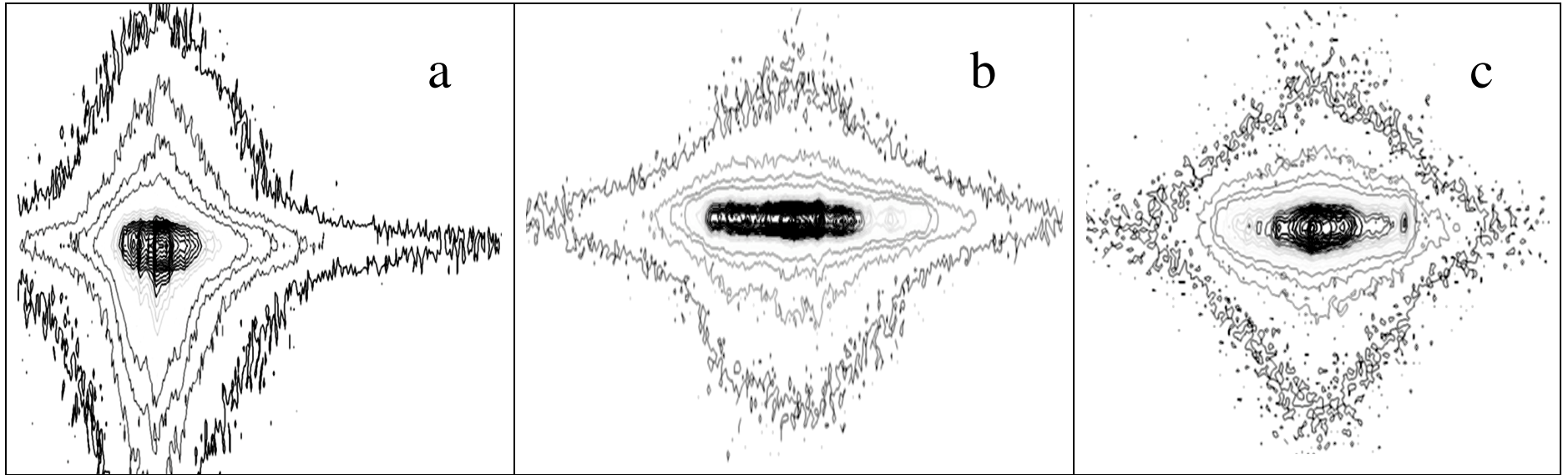


Figure 13: 2D Area Maps of Silver Implanted and Virgin ZnO annealed at 1000°C.

Figure 13a: Showing hydrostatic strain induced distortion of (002) hexagonality. Figures 13b and figure 13c showing the hexagonality of the (004) and (006) reflection.